Study on Fabrication and Characterization of $Zn_{1-x}Mg_xO$ Thin Films and $Zn_{1-x}Mg_xO/Ag_yO$ Heterojunction Diodes by Mist-CVD

by

Xiaojiao Liu

Student ID Number:1248009

A dissertation submitted to the

Department of Engineering,

Graduate School of Engineering,

Kochi University of Technology,

Kochi, Japan

in partial fulfillment of the requirements for the degree of

Doctor of Engineering

Assessment Committee:

Supervisor: Toshiyuki KAWAHARAMURA

Co-Supervisor: Mamoru FURUTA

Co-Supervisor: Chaoyang LI

Associate Professor: Akitaka ITO

Associate Professor: Hirokazu KOBAYASHI

September 2023

ABSTRACT

This thesis studies the fabrication and characterization of $Zn_{1-x}Mg_xO/Ag_yO$ heterojunction diodes (HJDs) via the Mist-CVD and sputtering methods. Different from the conventional deposition method, Mist-CVD is a non-vacuum and low-cost deposition technique. The three layers of ITO, $Zn_{1-x}Mg_xO$, and Ag_yO films applied in the HJDs all can be grown by Mist-CVD which are comparable to those achieved using similar but more expensive preparation methods. The detailed research works are summarized in 7 chapters as the following:

In Chapter 1, overviews of metallic oxides based on the typical metal-oxygen (MO) or transition-metal-oxygen (TMO) system of compound semiconducting materials have been described. The typical MO semiconduction materials of II-oxides, III-oxides, and IV-oxides, and TMO semiconduction materials of I-oxides have been reviewed. In addition, the properties of ZnO and the research status of ZnO-based heterojunction have been specifically reviewed.

In Chapter 2, the working principles, apparatus structures and parameters, and operation processes of fabrication equipment and characterization devices are introduced.

In Chapter 3, research on the fabrication and characterization of ZnMgO thin film grown by Mist-CVD is described. Aiming to optimize the performance of ZnO-related power devices, the crucial point is to grow high-quality ZnO-based thin films. The studies are based on 3rd generation of the Mist-CVD system. Investigation based on three different directions: 1) influence of different $[H_2O]/\{[Zn]+[Mg]\}$ supply ratio, 2) influence of Mg content, and 3) influence of O_3 supporting on ZnMgO characteristics. Even though we had already reported on the changes of ZnO characteristics with the supply ratio of $[H_2O]/[Zn]$, after introducing Mg the properties of ZnMgO have changed very much. The obtained results indicate that the H_2O supply amount was

influenced by Mg c.g./d.g., and the supply ratio of $[H_2O]/\{[Zn]+[Mg]\}$ has strongly impacted the growth rate and crystal orientations. The optical band gaps of ZnMgO films were widened from 3.22 to 3.83 eV by increasing the H_2O concentration with fixing Mg c.g./d.g. = 1.0/4.0. At the same supply ratio of $[H_2O]/\{[Zn]+[Mg]\}$, and Mg c.g./d.g. = 2.0/3.0 after adding the support oxidant of O_3, the resistivity increased to 8.24×10^5 Ω·cm, whereas without O_3, the resistivity decreased to 5.08×10^5 Ω·cm. As the flow rate of the Mg c.g. / d.g. increased, the morphology and crystallinity of the ZnMgO films were also extensively impacted by the Mg content and the band gaps of ZnMgO broadened from 3.3 to 3.7 eV, and resistivity increased to 1.58×10^8 Ω·cm.

In Chapter 4, the results of the preparation and characterization of Ag_xO thin film grown via a mist chemical vapor deposition (mist-CVD) system are described. It has been demonstrated that the mist-CVD system has the potential to grow Ag and Ag_xO thin films, the oxidants of O_3 and H_2O have an extensive influence on the Ag_xO properties, and the mist-CVD system has been proved to have the capability of depositing the metallic-oxide thin film.

In Chapter 5, the effects of oxygen flow ratio ($R[O_2]$ %) on the properties of Ag_xO thin films grown by RFM-Sputtering are discussed. While adjusting oxygen flow ratios ($R[O_2]$ %) from 0 % to 30 %, Ag_xO thin film transitioned from metal to semiconductor and/or insulator with different transparent appearances from the analysis results of GIXD, transmittance and SEM surface observed. Especially, at high oxygen flow ratios, the Ag_xO film is multi-phased as a mixture of $Ag^{(II)}O$ and $Ag_2{}^{(III)}O_3$. In addition, the work function (ϕ) of those samples changes from 4.7 eV to 5.6 eV as measured by photoelectron yield spectroscopy (PYS). The compositional and chemical state changes that occur at the Ag_xO surface during the increments of $R[O_2]$ % are evaluated by the relative peak intensities and binding energy shifts in x-ray photoelectron spectroscopy (XPS). With the incorporation of more electrons in chemical bonding, the oxygen-induced band forms. Combining all the results from transmittance

(band gaps confirmation), PYS (work function confirmation), and XPS (valence band position confirmation), the estimation band diagrams are given for the oxidation state of Ag_xO with various oxygen flow ratios.

Chapter 6 reports on the preparation of heterojunction based on $Zn_{1-x}Mg_xO/Ag_yO$ semiconductor heterostructure. A series of multi-layers, containing $Zn_{1-x}Mg_xO$ (ZnMgO) films stacked on InSnO (ITO) films, were prepared using a mist chemical vapor deposition system with different flow rates for the Mg carrier gas/dilution gas (c.g. / d.g.). Based on the results of Chapter 4, Ag_yO films then were deposited on the ZnMgO/ITO substrates by sputtering with reference to the results in Chapter 5. It was found that the cross-section images of the ZnMgO/Ag_yO HJDs showed spontaneous order of the random alloys and partial inclinations of the multi-layers. Although the energy gap variations caused abrupt interfaces, these ZnMgO/Ag_yO HJDs demonstrated rectifying behavior with a barrier height of around 0.98 eV, which is comparable to that achieved using conventional vacuum methods.

In Chapter 7, the main results have been summarized in this chapter, and depending on the understanding of the past work, look into the future and plan the blueprint.

FULL CONTENTS

ACKNOWLEDGEMENTS

My accomplishment of today could not have been reached without significant help from many individuals. First of all, I would like to express my grateful appreciation to my supervisor Prof. Toshiyuki Kawaharamura for his guidance and support during my study time in KUT. I am especially thankful for his generous help when I was in the most difficult time of my life. I thank him for his patient guidance, encouragement and support in my research project. I feel really lucky to had such a precious mentor as he is, it is my honor that I had the golden opportunity to study in Kawaharamura Laboratory, and your kindness will be engraved in my heart forever.

My special thanks of gratitude to my co-supervisor Prof. Furuta Mamoru who help in completing my project, and gave me important guidance and suggestions on the study of heterojunction diodes. I came to know about lots of new knowledge, I am really thankful to them. Not only in science but also in job hunting and life, sincerely thanks for his help and support.

My special thanks to my vice-supervisor Prof. Chaoyang Li for supporting me of my research project and giving me precious help and advices.

I thank Prof. Akitaka ITO for support and instruct me of my research project and giving me precious help and advices on the review of my thesis.

I thank Prof. Hirokazu Kobayashi for support and instruct me of my research project and giving me precious help and advices on the review of my thesis.

I thank Prof. Koji KITA for accepting my application and give me chance to study in his Laboratory. I thank for his help making my dream come true. His teachings and instructing, which I always remember in my heart, and continue to guide and benefit me all my life. I'm really grateful for him.

I extend my sincere gratitude to Dr. Giang T. Dang for his precious advices and dis-

cussions in the diodes study. And thanks to Dr Li Liu for teaching me how to use mist-CVD system, and also thanks to Tatsuya Yasuoka and Masahiko Komatsu supporting me in my daily experiments and instructing me in job hunting. Thank you all very much.

I would also extend my gratitude to all those who have directly and indirectly helped me in my research project.

Last but not the least, I thank for my parents for birthing me, raising me, and educating me to be a positive and kind person, and I wish that I could tell you all these good things happening in my life and you would be happy and proud of me.

LIST OF FIGURES

LIST OF TABLES

Chapter 1

Introduction

1.1 Overview of Semiconducting Metallic Oxides

Depending on the conductivity of the thin films, they are broadly divided into three types: metal, semiconductor, and insulator. Meanwhile, at different oxidation extents, metallic oxide thin films can be transformed into semiconductors and/or insulators. For decades, metallic oxides of the earth elements have gained tremendous interest for metallic oxide thin films that are oxidized from the beginning they are highly reliable, stable, and have excellent environmental friendliness. They are extremely superior functional thin films and are currently being applied to many electronic and optical devices.

I	II	III	IV	V	VI
	4 Be	5 B	6 C	7 N	8 O
	12 Mg	13 Al	14 Si	15 P	16 S
29 Cu	30 Zn	31 Ga	32 Ge	33 As	34 Se
47 Ag	48 Cd	49 In	50 Sn	51 Sb	52 Te
49 Au	80 Hg	81 Tl	82 Pb	83 Bi	84 Po

Fig. 1.1 Abbreviated periodic table of the elements

In general, a semiconducting metallic oxide is a traditional non-stoichiometric oxide and is sensitive to electrical conductivity [1]. As shown in Fig. 1 the abbreviated periodic table of the elements (I, II, III, IV, V, and VI groups), including metals and transition metals. Although the group V-oxides are covalent bonding and admixture of ionic bonding, when going from group IV-oxides to III-oxides, II-oxides, and I-oxides one has increasing ionic bonds and ends up with completely ionic bonding.

Group IV-oxides, such as silicon dioxide (SiO_2) is important in glass manufacture and electronics. and its various allotropic forms include quartz, cristobalite, tridymite, stishovite and vitreous silica [9]; the band gap of SiO_2 had been calculated by Chelikowsky and Schluter [10, 11] with E_G = 9.2 eV (indirect band gap) and silicon only has a band gap of 1.12 eV. And germanium (Ge) is also a low band gap (0.67 eV) semiconductor but GeO_2 is an ultra-wide bandgap semiconductor (~ 6 eV) [12]. Therefore, SiO_2 and GeO_2 are typically used as a dielectric material for the metal-oxide-semiconductor (MOS) devices because they block the unwanted leakage current due to their high energy barrier [13, 14]. Group-V elements such as As_2O_3 and Sb_2O_3 have been proposed as p-type dopants used in metallic oxide films [2-8], which is based on substituting a group VI-oxide anion with a group-V atom to create a hole. Therefore, phosphorus (P), arsenic (As), and antimony (Sb) are generally used as p-type dopants. Vice versa elements from group-III (B, Al, In, etc.) are used as n-type dopants.

III-oxide compounds belong to the metal oxide system so this group presents much different properties than those of the group I and II transition oxides. β-Ga_2O_3 has a very large breakdown field (E_b) value (~8 MV/cm) and a wide band gap (4.9 eV) [15]. Therefore, it is a promising material to be used in power electronics and is good for reducing the size of the device due to its advantage in high electric fields [16]. Tin-doped indium oxide (ITO) has been deposited by magnetron sputtering [17] and mist-CVD [18] has been used for transparent electrode applications. However, the cost and toxicity of indium limit its application in the expanding electronic industry.

Common transition metallic oxides from group I-oxides and group II-oxides, such as CuO, AgO, AuO, etc., exhibit a variety of novel properties [19-24]. The activity is in order as Cu > Ag > Au. Cu_2O is one of the stable phases of the three oxidation states of copper-oxide compounds (others are Cu_4O_3, CuO) [25]. Gold and silver are generally used as electrodes. Gold and silver can appear in three states of oxidation, I, II, and III. Silver oxide (Ag_xO) is a transparent material in wavelengths ranging from the infrared region to the visible region with an optical band gap in the range of 1.2 ~ 3.1 eV.

II-oxide compounds ZnO crystallize in the hexagonal wurtzite-type structure and as a wide band gap semiconductor with a band gap energy of 3.3 eV (375 nm) it could have a promising future for ultraviolet optoelectronics. ZnO properties are described in detail in Section 1.2.

1.2 Zinc Oxide Properties

Semiconductor zinc oxide (ZnO) is one of the common II-O binary compound semiconducting materials, others including BeO, MgO, and CdO. And ZnO crystalline in the structure of wurtzite, zinc blend, and rock salt [25] [26]. Fig. 1.2 shows the (a) crystal structure of wurtzite ZnO [27]. Zn^{2+} interconnects with O^{2-} forming the hexagonal lattice that each cation is surrounded by four anions at the tip of a triangular pyramid [28]. Under ambient conditions, the crystal structure of wurtzite is a thermodynamically stable grain phase for ZnO because its atoms bond covalently in sp3 hy-

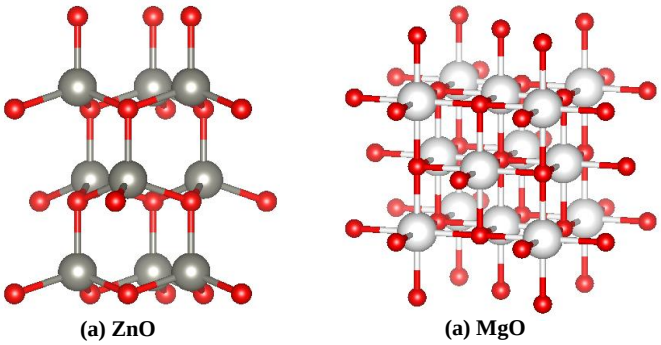

(a) ZnO **(a) MgO**

Fig. 1.2 Crystal structure of (a) wurtzite ZnO (b) cubic MgO

bridization and also behave like an ionic character. Therefore, ZnO is a semiconducting material between covalent semiconductors and ionic semiconductors. Additionally, ZnO is a wide band gap semiconductor with a direct gap of around 3.44 eV, where the lowest bottom of conduction bands and the uppermost top of valence bands energy aligns at the same position in k-space; and a large exciton binding energy of 60 meV at room temperature. Table 1-1 [29] shows the comparison between different candidate materials for next generation power devices. ZnO has its promising advantages.

Table 1-1. Comparison between different candidate materials for next generation power devices [29]

	Si	**GaAs**	**4H-SiC**	**GaN**	**ZnO**	**β-Ga_2O_3**	**C**	**AlN**	**MgO**
Band Gap (eV)	1.12	1.4	3.2	3.39	**3.4**	4.8-4.9	5.6	6	**7.83**
Thermal conductivity (W/cm·K)	1.3	0.54	5	1.3	**~1**	~0.2	20	321	30
Electron mobility ($cm^2 V^{-1} s^{-1}$)	1450	8500	950	2000	**300**	300	4000		
Exciton binding energy (meV)				24	**60**				
Saturation electron velocity ($\times 10^7$ cm/s)	1	2	2	2	**3**		3		

The beginning of the ZnO study can be traced back to the 1930s [30]. ZnO is considered as a promising material for use in blue/UV optoelectronics, including light-emitting diodes, laser diodes, and detectors [31-33]. Fig. 1.2 (b) shows the cubic crystal structure of MgO. ZnO was able to be alloyed with Mg and Cd, to enlarge and narrow the bandgap, respectively. The lattice change of ZnO-base alloys is relatively smaller than that of GaN-base alloys. This is due to the similarity in the radii of Zn^{2+} (0.6 Å) and Mg^{2+} (0.57 Å) in which the ZnMgO alloy is generally formed when Zn^{2+} in ZnO is partially substituted by Mg^{2+}. The band gap of MgO is around 7.8 eV, thus ZnMgO can have an expanding band gap extending from 3.4 eV to 7.8 eV. However, alloying ZnO with CdO (1.09 eV) can have a direct band gap that is narrowed to 2.4

eV, and an indirect band gap of 0.8 ~ 1.1 eV [34, 35].

Highly n-doped ZnO : Al can be used as a transparent conducting oxide (TCO) [36]. The expectation of ZnO : Al is a cheaper and conducting oxide alternative of ITO since the component elements of Zn and Al are much cheaper and less poisonous compared to that of the generally used indium tin oxide (ITO). Therefore, ZnO has been used as the front contact for solar cells to avoid the shadow effect of the metal finger contacts.

Depending on its intended applications, there are different methods for growing high-quality ZnO. ZnO powder is produced from the combustion of vapors resulting from the distillation of metallic zinc by a dry process [37]. The large size of the bulk ZnO had grown through a melt growth process, in which the ZnO melt is in a water-cooled crucible and with an oxygen overpressure close to 50 atm, that prevents the decomposition, and establishes an equilibrium between liquid ZnO and the oxygen pressure to protect the lattice from reduction [38,39]. Eagle-Picher has been reported seeded chemical vapor transport (SCVT) for the manufacture of ZnO wafers at 1000 ~ 1200℃ and still attracts a lot of interest for the growth of the crystal and epitaxial layer [40]. The ZnO crystal is grown using NaCl as a solvent at temperatures of about 900°C [41]. Using a KOH/LiOH solvent by hydrothermal process, bulk single crystals of ZnO of approximately 10 mm in dimension have been grown at temperatures less than 400 °C, at pressures ranging from 830 to 1110 MPa [42]. The thin film of ZnO has also been grown by various methods, such as chemical vapor deposition (CVD) [43-45], pulsed laser deposition (PLD) [46, 47], molecular beam epitaxy (MBE) [48-50], direct current (DC) magnetron sputtering, and radio frequency (RF) magnetron sputtering [51-52]. In recent years, many reports of the ZnO thin films grown via the third-generation mist-CVD system have been published [53-58] for its low cost and environmental friendly characteristics, the details of the third-generation mist-CVD will be introduced in Chapter 2.

ZnO with a wide direct band gap has electrical properties different from those of

others. In the low electric field, using the Mone Carlo simulation, Albrecht et al. [60] predicted that the electron mobility of undoped single-crystalline ZnO was about 300 $cm^2 V^{-1} s^{-1}$ at room temperature. In practical terms, the charge carrier mobility in ZnO is measured using the Hall effect. The highest bulk mobility of a single ZnO crystal at room temperature is approximately 205 $cm^2 V^{-1} s^{-1}$ with a carrier concentration of 6×10^{16} cm^{-3} [61, 62]. Depending on the growth technique, the mobility of charge carrier mobility at room temperature varies from less than 100 $cm^2 V^{-1} s^{-1}$ to around 150 $cm^2 V^{-1} s^{-1}$ [63-67]. In the high electric field, the drift velocity versus the electric field characteristic for bulk ZnO [68] from Monte Carlo simulations predicting was predicted. And in lower electric field, the drift velocity at room temperature occurs at 50 kV cm^{-1}, and a peak value of 3×10^7 cm s^{-1}. With increasing the electric field further more leads to a decrease of the drift velocity.

However, growing high-quality p-type ZnO was the limitation for the ZnO-based application in optoelectronics. Recently, some researchers have reported that ZnO : Li may form a shallow acceptor in ZnO [69, 70]. Subsequently, with the Group V elements N [71], P [72, 73, 74] or As [75, 76] on the oxygen site also showed p-doping results in ZnO.

1.3 ZnO-based Devices

The heterostructure may be built from two or more semiconducting layers with different energy band gaps. Conjoin semiconductors can be the compound from groups II-VI or III-V, or the semiconductor alloys. Depending on the application of the heterojunctions, the band gap value can be adjusted by replacing the element or varying the composition of the alloy [77, 78, 79].

Recently, there have been numerous studies reporting ZnO-based heterojunction diodes. For flexible and transparent thin film transistors (TFTs), ZnO-based semiconducting materials have been widely used as the channel layer. ZnO nanorods have been used as a conducting channel [80]. A single ZnO nanowire for a UV detector ob-

tained an excellent UV response [81]. The fabrication of a UV light-emitting diodes (LEDs) based on a p–n junction n-ZnMgO/n-ZnO/p-AlGaN/p-GaN semiconductor triple-heterostructure shows ZnO-based materials for UV emitters having the potential to lower the cost and higher emission intensity than AlGaN/GaN device [82]. Light-emitting diodes (LED) based on ZnO homojunctions in part with some $Zn_{1-x}Mg_xO$ barrier in order to influence carrier diffusion and recombination obtained by references [83, 84]. The performance of a device strongly depends on the interface between the drain/source electrodes and the semiconducting active layer. Therefore, optimization of active layer properties is the crucial point for achieving high performance devices.

1.4 Outline of This Thesis

Aiming to achieve high-performance ZnMgO/Ag_yO heterojunction diodes (HJDs), optimizations of the processes of the diodes and the properties of each layer are carried out. The optical and electrical characteristics of ZnMgO via Mist-CVD and the optical and electrical characteristics of Ag_xO via sputtering are summarized. The outline of the chapters is as follows:

Chapter 2 describes the fabrication and characterization system.

Chapter 3 focuses on the growth of ZnMgO thin film by mist-CVD for heterojunction diodes. The influence of different [H_2O]/{[Zn]+[Mg]} supply ratio, the influence of Mg content, and the influence of O_3 supporting on ZnMgO characteristics are described.

Chapter 4 gives the trial experiments of mist-CVD growth of Ag_xO thin film. Temperature dependences and suitable oxidants comparison for Ag and Ag_xO films are presented.

Chapter 5 is devoted to techniques used to characterize the electrical and optical properties of Ag_xO thin film grown by RFM-sputtering. The chemical states and estimated band gap diagram of the RFM-sputtering Ag_xO thin

film are also described.

Chapter 6 discusses the structure, design, and performance of ZnMgO/Ag_yO diodes, and gives a schematic energy diagram of the interface between ZnMgO/Ag_yO HJDs.

Chapter 7 conclusions.

1.5 References

[1] J. B. Goodenough, Progress in Solid State Chemistry, 5 C, 145-399.

[2] D. C. Look, Mater. Sci. Eng., B 80, 383 (2001).

[3] C. Jagadish and S. J. Pearton, Zinc Oxide Bulk, Thin Films and Nanostructures (Elsevier, Oxford, 2006).

[4] D. C. Look, D. C. Reynolds, C. W. Litton, R. L. Jones, D. B. Eason, and G. Cantwell, Appl. Phys. Lett. 81, 1830 (2002).

[5] K. Kim, H. Kim, D. Hwang, J. Lim, and S. Park, Appl. Phys. Lett. 83,63 (2003).

[6] C. Morhain, M. Teisseire, S. Vézian, F. Vigué, F. Raymond, P. Lorenzini, J. Guion, G. Neu, and J.-P. Faurie, Phys. Status Solidi B 229,881 (2002).

[7] Y. R. Ryu, T. S. Lee, and H. W. White, Appl. Phys. Lett. 83,87 (2003).

[8] T. Aoki, Y. Shimizu, A. Miyake, A. Nakamura, Y. Nakanishi, and Y. Hatanaka, Phys. Status Solidi B 229,911 (2002).

[9] R. W. G. Wyckoff, Crystal Structures, Vol. 1 (Interscience, New York, 1963).

[10] M. Schluter and J. R. Chelikowsky, Solid State Commun. 21 (1977) 381.

[11] J. R. Chelikowsky and M. A. Schluter, Phys. Rev. B15 (1977) 4020.

[12] M. Ardyanian, H. Rinnert, X. Devaux, M. Vergnat, Structure and photoluminescence properties of evaporated GeO_x thin films, Appl. Phys. Lett. 89 (2006) 011902 – 011904.

[13] C. Bin, Y. Y. Tang, X. X. Rong, W. Ning, M. Z. Yang, S. Kun, Z. X. Jun, Analysis of temperature-dependent characteristics of a 4H-SiC metal-semiconductor-metal ultraviolet photodetector, Appl. Phys. 57 (34) (2012) 4427 – 4433.

[14] S. N. A. Murad, P. T. Baine, D. W. McNeill, S. J. N. Mitchell, B. M. Armstrong, M. Modreanu, G. Hughes, R. K. Chellappan, Optimization and scaling of interfacial GeO_2 layers for high-k gate stacks on germanium and extraction of dielectric constant of GeO_2, Solid. Electron. 78 (2012) 136 – 148.

[15] A. T. Howe, and P. J. Fensham, Quart. Rev. (Chem. Soc. London), 21, 507 (1967).

[16] D. Adler, Solid State Phys., Eds. F. Seitz, D. Turnbull, and H. Ehrenreich 21, 1

(1968).

[17] C. N. R. Rao, and G. V. Subba Rao, phys. stat. solidi (a) 1, 597 (1970).

[18] Goodenough, J. B., in Progress in Solid State Chemistry, Vol. 5, Ed. H. Reiss (Pergamon Press, Oxford, 1971).

[19] M. Higashiwaki, K. Sasaki, A. Kuramata, T. Masui, and Y. Shigenobu. Gallium oxide (Ga_2O_3) metal-semiconductor field-effect transistors on single-crystal β-Ga_2O_3 (010) substrates. Appl. Phys. Lett. Jan 2012, 100, 1-3.

[20] X. Huiwen, H. Qiming, J. Guangzhong, L. Shibing, P. Tao, and L. Ming. An Overview of the Ultrawide Bandgap Ga_2O_3 Semiconductor Based Schottky Barrier Diode for Power Electronics Application. Nanoscale Res. Lett. Sept 2018, 13, 1 – 13.

[21] T. Minami, K. Shimokawa and T. Miyata, Journal of Vacuum Science & Technology A 16, 1218 (1998).

[22] Dang, G. T., Allen, M. W., Furuta, M., & Kawaharamura, T. (2019). Electronic devices fabricated on mist-CVD-grown oxide semiconductors and their applications. Japanese Journal of Applied Physics, 58(9), 090606.

[23] U. Ozgur, Y. I. Alivov, C. Liu, C. Teke, A. Reshchikov, M. A. Dogan, S. Avrutin, V. Cho, S. J. Morkoc, H.: J. Appl. Phys. 98, 041301 (2005).

[24] Klingshirn, Chem. "ZnO: material, physics and applications." ChemPhysChem 8.6 (2007): 782-803.

[25] B. K. Meyer, A. Polity, D. Reppin, M. Becker, P. Hering, P. J. Klar, & Ronning, C. (2012). Binary copper oxide semiconductors: From materials towards devices. physica status solidi (b), 249(8), 1487-1509.

[26] Shouli Bai, Song Chen, Yangbo Zhao, Teng Guo, Ruixian Luo, Dianqing Li and Aifan Chen, J. Mater. Chem. A, 2014, 2, 16697.

[27] C. Jagadish, S. J. Peartton, Zinc Oxide Bulk, Thin Films and Nanostructures: Processing, Properties and Applications. Elsevier, Amsterdam/London (2006).

[28] Y. Kato and T. Takei 1930 Trans. Amer: Electrochem. Soc. 57 297.

[29] Shizuo Fujita, Jpn. J. Appl. Phys. 54 030101 (2015).

[30] Holland, Harold Cecil. "LXXXV.-The ternary system zinc oxide–zinc chloride–water." Journal of the Chemical Society (Resumed) (1930): 643-648.

[31] H. Natsuhara, K. Matsumoto, N. Yoshida, T. Itoh, S. Nonomura, M. Fukawa, K. Sato, Sol. Energ. Mater. Sol. Cell. 90, 2867 (2006).

[32] X. Q. Wei, J. Z. Huang, M. Y. Zhang, Y. Du, B. Y. Man, Mater. Sci. Eng. B 166, 141–146 (2010).

[33] K. Ajay, K. Davinder, Sol. Energ. Mater. Sol. Cell. 93, 193 (2009).

[34] C. Sravani, K. T. R. Reddy and P. J. Reddy: Mater. Lett. 15 (1993) 356. 8) F. P. [10] Koffyberg: Phys. Rev. B 13 (1976) 4470.

[35] T. Minami, H. Nanot, S. Takata, Jpn. J. Appl. Phys. 1984, 23, L280; P. Kuppusami, K. Diesner, I. Sieber, K. Ellmer, Mater. Res. Soc. Symp. Proc. 2002, 721, 171; C. Agashe, O. Kluth, G. Schope, H. Siekmann, J. Hupkes, B. Rech, Thin Solid Films 2002, 442, 167.

[36] Y. W. Heo, L. C. Tien, Y. Kwon, D. P. Norton, S. J. Pearton, B. S. Kang, F. Ren, Appl. Phys. Lett. 2004, 85, 2274.

[37] G. Agarwal, J. E. Nause, and D. N. Hill, Mat. Res. Soc. Symp. Proc. 512, 41 (1998).

[38] D. C. Reynolds, C. W. Litton, D. C. Look, J. E. Hoeschler, B. Claflin, T. C. Collins, J. Nause, and B. Nemeth, J. Appl. Phys. 95, 4802 (2004).

[39] I. L. Khodakovsky, A.E. Elkin, Geochemistry 10 (1975) 1490.

[40] Triboulet, Robert, et al. "The scope of zinc oxide bulk growth." Zinc Oxide—A Material for Micro-and Optoelectronic Applications. Springer Netherlands, 2005.

[41] T. Sekiguchi, S. Miyashita, K. Obara, T. Shishido, and N. Sakagami, J. Crystal Growth 214/215, 72 (2000).

[42] Y. Natsume, H. Sakata, T. Hirayama, et al., Journal of Applied Physics 72, 4203 (1992).

[43] C. R. Gorla, N. W. Emanetoglu, S. Liang et al., J. Appl. Phys. 85, 2595 (1999).

[44] B. S. Li, Y. C. Liu, Z. Z. Zhi et al., J. Vac. Sci. Technol. A 20, 1779 (2002).

[45] H. Z. Wu, K. M. He, D. J. Qiu, and D. M. Huang, J. of Crystal Growth 217, 131 (2000).

[46] T. Ohgaki, N. Ohashi, H. Kakemoto et al., J. Appl. Phys. 93, 1961 (2003).

[47] M. Chen, Z. L. Pei, C. Sun et al., J. Crystal Growth 220, 254 (2000).

[48] K. Tominaga, T. Murayama, I. Mori et al., Thin Solid Films 386, 267 (2001).

[49] I. Ohkubo, Y. Matsumoto, M. Lippmaa, H. Koinuma, et al., Applied Surface Science 159–160 2000 514 – 519.

[50] Y. Igasaki, T. Naito, K. Murakami et al., Appl. Surf. Science 169-170, 512 (2001).

[51] F. J. Haug, Zs. Geller, H. Zogg et al., J. Vac. Sci. Technol. A 19, 171 (2001).

[52] T. Minami, T. Miyata, T. Yamamoto et al., J. Vac. Sci. Technol. A 18, 1584 (2000).

[53] Toshiyuki Kawaharamura et al 2008 Jpn. J. Appl. Phys. 47 4669.

[54] Toshiyuki Kawaharamura 2014 Jpn. J. Appl. Phys. 53 05FF08.

[55] Giang T. Dang, Toshiyuki Kawaharamura, Mamoru Furuta, Martin W. Allen, et al., Applied Physics Express 9, 041101 (2016).

[56] Phimolphan Rutthongjan et al., 2019 Jpn. J. Appl. Phys. 58 035503.

[57] Toshiyuki Kawaharamura et al., 2013 Jpn. J. Appl. Phys. 52 035501.

[58] Li Liu et al 2019 Jpn. J. Appl. Phys. 58 025502.

[59] J. G. Lu, Y. Z. Zhang, Z. Z. Ye, L. P. Zhu, L. Wang, B. H. Zhao, Q. L. Liang, Appl. Phys. Lett. 2006, 88, 222114; Y. J. Zeng, Z. Z. Ye, W. Z. Xu, D. Y. Li, G. J. Lu, L. P. Zhu, B. H. Zhao, Appl. Phys. Lett. 2006, 88, 062107.

[60] J. Sann, A. Hofstaetter, D. Pfisterer, J. Stehr, B. K. Meyer, Phys. Status Solidi C 2006, 4, 952; Y. J. Zeng, Z. Z. Ye, W. Z. Xu, D. Y. Li, J. G. Lu, L. P. Zhu, B. H. Zhao, Appl. Phys. Lett. 2006, 88, 062107.

[61] Albrecht, J.D., Ruden, P.P., Limpijumnong, S., Lambrecht, W.R.L., Brennan, K.F.: High field electron transport properties of bulk ZnO. J. Appl. Phys. 86(12), 6864 (1999).

[62] Look, D.C., Reynolds, D.C., Sizelove, J.R., R.L., Litton, C.W., Cantwell, G.,

Harsch, W.C.: Electrical properties of bulk ZnO. Solid state commun. 105(6), 399-401 (1998).

[63] Look, D.C., Reynolds, D.C., Sizelove, J.R., Residual native shallow donor in ZnO. Phys. Lett. 82(12), 2552-2555 (1999).

[64] Iwata, K., Fons, P., Niki, S., Yamada, A., Matsubara, K., Nakahara, K., Takasu, H.: Improvement of electrical properties in ZnO thin films grown by radical source (RS)-MBE. Phys. Status Solidi (a) 180 (1), 287-292 (2000).

[65] Miyamoto, K., Sano, M., Kato, H., Yao, T.: Effects of ZnO/MgO double buffer layers on structural quality and electron mobility of ZnO epitaxial films grown on c-plane sapphire. Jpn. J. Appl. Phys. 41 (part2), No. 11A, L1203-L1205.

[66] Edahiro, T., Fujimura, N., Ito, T.: Formation of two-dimensional electron gas and the magnetotransport behavior of ZnMnO/ZnO heterostructure. J. Appl. Phys. 93(10), 7673(2003).

[67] Kaidshev, E.M., Lorenz, M., von Wenckstern, H., Rahm, A., Semmelhack, H.-C., et al., Appl. Phys. Lett. 82(22), 3901(2003).

[68] Z. Fan, D. Wang, P.-C. Chang, W.-Y. Tseng, J. G. Lu, Appl. Phys. Lett. 2004, 85, 5923.

[69] Zeng, Y. J., et al. "Dopant source choice for formation of p-type ZnO: Li acceptor." Applied Physics Letters 88.6 (2006): 062107.

[70] Y.J. Zeng, Z.X. Jian, Z.Z. Ye, G.H. Gao, Y.F. Lu, B.H. Zhao, L.P. Zhu, S.H. Hu. State Superlattices and Microstructures 43 (2008) 278 – 284.

[71] K. H. Bang, D-K. Hwang, M-C. Park, Y-D. Ko, I. Yun, and J-M. Myoung, Appl. Surf. Sci. 210,177 (2003).

[72] K-K. Kim, H-S. Kim, D-K. Hwang, J-H. Lim, and S-J. Park, Appl. Phys. Lett. 83, 63 (2003).

[73] Y. W. Heo, Y. W. Kwon, Y. Li, S. J. Pearton, and D. P. Norton, Appl. Phys. Lett. 84,3474 (2004).

[74] Y. R. Ryu, S. Zhu, D. C. Look, J. M. Wrobel, H. M. Jeong, and H. W. White, J.

Cryst. Growth 216, 330 (2000).

[75] Y. R. Ryu, T. S. Lee, and H. W. White, Appl. Phys. Lett. 83,87 (2003).

[76] D. C. Look; G. M. Renlund; R. H. Burgener, et al., Appl. Phys. Lett. 85, 5269–5271 (2004).

[77] Giorgio Margaritondo, *Electronic Structure of Semiconductor Heterojunctions* (1988).

[78] L. J. Brillson, G. K. Sujan, Semiconductor Heterojunctions, An Essential Guide to Electronic Material Surfaces and Interfaces, (2016).

[79] H. E. Brown, Zinc oxide: *Properties and applications, International Lead Zinc Research Organization* (1976).

[80] Ryu, Y. R., T. S. Lee, and H. W. White. "Properties of arsenic-doped p-type ZnO grown by hybrid beam deposition." Applied Physics Letters 83.1 (2003): 87-89.

[81] Kind, H.; Yan, H.; Messer, B.; Law, M.; Yang, P. Nanowire ultraviolet photodetector sand optical switches. Adv. Mater. 2002, 14, 158–160.

[82] Hyuck Soo Yang et al 2005 Jpn. J. Appl. Phys. 44 7296.

[83] Tsukazaki, A. Ohtomo, T. Onuma, M. Ohtani, T. Makino, M. Sumiya, K. Ohtani, S. F. Chichibu, S. Fuke, Y. Segawa, H. Ohno, H. Koinuma, M. Kawasaki, Nat. Mater. 2005, 4, 42.

[84] Tsukazaki, M. Kubota, A. Ohtomo, T. Onuma, K. Ohtani, H. Ohno, S. F. Chichibu, M. Kawasaki, Jpn. J. Appl. Phys. 2005, 44, L643; Y. Ryu, T.-S. Lee, J. A. Lubguban, H. W. White, B.-J. Kim, Y.-S. Park, C.-J. Youn, Appl. Phys. Lett. 2006, 88, 241108; S. J. Jiao, Z. Z. Zhang, Y. M. Lu, D. Z. Shen, B. Yao, J. Y. Zhang, B. H. Li, D. X. Zhao, X. W. Fan, Z. K. Tang, Appl. Phys. Lett. 2006, 88, 031911; H. White, Y. Ryu, Opto Laser Europe 2006, 143, 26.

Chapter 2

Fabrication Systems and Characterization Techniques of Metallic Oxide Thin Films

In this chapter, the deposition systems and evaluation techniques of metallic oxide thin films were briefly presented. The main fabrication systems for the single layer include the third-generation Mist-CVD system (3rd Mist-CVD) and the radio frequency magnetron sputtering (RFM-SPT). For the formation of heterojunction device, the third-generation Mist-CVD system (3rd Mist-CVD) was used for ITO thin film deposition, which was formed as the backside electrode, and used for $Zn_{1-x}Mg_xO$ thin film preparation, which was formed as the active layer. The RFM-sputtering system was used for Ag_xO thin film deposition. And the electron beam vapor deposition system was used for the top side electrode of Au deposition. Meanwhile, different types of characterization techniques were used for the evaluation and analysis of metallic oxide thin films, including sample thicknesses, surface morphology, crystal structure, transmittance, and among others. All the details will be presented in each section.

2.1 Fabrication Systems

2.1.1 Mist Chemical Vapor Deposition (CVD)

The third-generation mist-CVD system (3rd Mist-CVD) mainly consists of two units as shown in Fig. 2.1, a supply unit and a reaction unit [1]. The supply unit is used for producing mist for the reaction unit for the thin film depositions, which consists of precursor solution chambers and ultrasonic transducers. The precursor solution of the target element is filled in the solution chamber, which is located upon the

ultrasonic transducers. The ultrasonic transducers are used to atomize or mist the liquid state precursor into the vapor state mist precursor, and afterward the precursor mist transfers to the reaction chamber through the medium gas of N_2.

Fig. 2.1 Schematic structure of Mist-CVD system [1]

The reaction unit consists of a reaction chamber, a heater, and an exhaust system. The reaction chamber has a mist mixing space and a fine channel (FC) structure, as shown in Fig. 2.2. In order to provide collisional mixing, the FC structure provides a space of only 1 mm between the top wall of the fine channel and the surface of the substrate. The precursor mist droplets flow through the top surface of the substrate, and then the mist evaporates and the precursors reacts and deposits on the substrate, and finally the extra mist is drawn into the exhaust system.

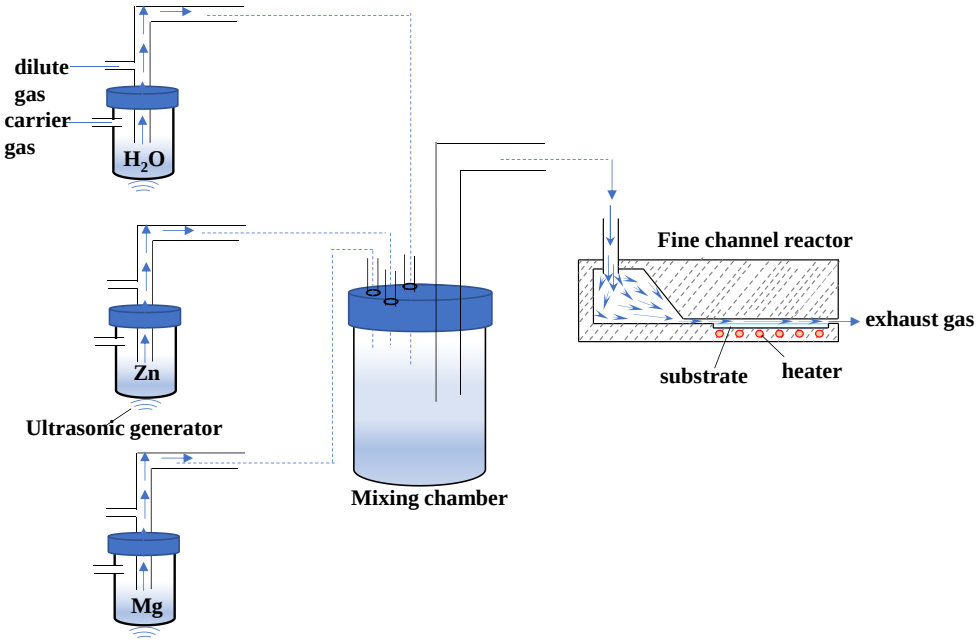

Fig.2.2 3rd-generation Mist-CVD installation with three chambers of ZnMgO deposition

Most of the CVD and solution-based processes are coordinated with the equilibrium reaction systems. In an equilibrium reaction of a mist-CVD system in order to form uniform and high-quality thin films, it is important to predict the reaction path and control the reaction conditions, such as the precursor composition, pressure, temperature, assistant gas species, and input power. At constant temperature and pressure, the composition of a reaction mixture has a tendency to minimize the Gibbs free energy, Whether or not a reaction is happening at a particular composition depends on the value of reaction Gibbs free energy $\Delta_r G$, it follows that

$$\Delta_r G = \Delta_r G^o + RTlnQ,$$

where Q is the reaction quotient, $Q = \frac{\text{activities of products}}{\text{activities of ractants}} = \prod_J a_J^{v_J}$, J denotes the substances and the v_J are the corresponding stoichiometric numbers in the chemical equation, which are positive for products and negative for reactants. $\Delta_r G^o$ is the standard Gibbs energy, and it is calculated from

$$\Delta_r G^o = \sum_{Products} v\,\Delta_f G^o - \sum_{Reactants} v\,\Delta_f G^o,$$

where the v is (positive) stoichiometric coefficients and $\Delta_f G^o$ is the standard Gibbs energy of formation. Therefore, as $\Delta_r G < 0$, the forward reaction is spontaneous; $\Delta_r G > 0$, the reverse reaction is spontaneous; as $\Delta_r G = 0$, the reaction is at equilibrium, so $\Delta_r G = 0$, $\Delta_r G^o = -RTlnQ$, then the activities have their equilibrium values

$$K = Q = \prod_J a_J^{v_J} = -\exp\frac{\Delta_r G^o}{RT}.$$

The ZnMgO thin films were grown by tri-solution chambers 3rd-generation mist-CVD at 400 ℃, as shown in Fig. 2.2, which is the experiment installation lateral view of the ZnMgO depositions [2]. H_2O solution is used as an assistant oxidant. All precursors are dissolved in methanol (CH_3OH, MeOH). In my experiment, all the reaction temperature is fixed at 400 ℃. Thus, pyrolysis, all the thermal decomposition of precursors, is carried out on a hot substrate. The reaction mechanism considered here is described as following:

$$5Zn(acac)_2 \cdot 2MeOH(aq) \rightarrow Zn_5(OH)_8(acac)_2 \cdot 2MeOH(aq) + 8AcacH(aq) \rightarrow$$

$$5ZnO(s) + 10AcacH(aq) + 5MeOH(l)\ (400\ ℃)$$

$$5Mg(acac)_2 \cdot 2MeOH \rightarrow Mg_5(OH)_8(acac)_2 \cdot 2MeOH(aq) + 8AcacH(aq) \rightarrow$$

$$5MgO(s) + 10AcacH(aq) + 5MeOH\ (400\ ℃).$$

They are all endothermic reactions [3, 4] Meanwhile, the assistance gas of O_3 decomposes into oxygen radicals (•O), then promotes MeOH and H_2O vapor produce hydroxyl radicals (•OH). These reactions can be expressed as [5]:

$$O_3 \leftrightarrow O_2 + \bullet O$$

$$CH_3OH + \bullet O \leftrightarrow CH_2OH + \bullet OH$$

$$H_2O + \bullet O \leftrightarrow 2\bullet OH.$$

Therefore, the participant oxidant is O_3, •O, •OH, then $Zn(acac)_2$ precursor and $Mg(acac)_2$ precursor may be randomly adjacent and decompose by activated oxygen sources.

2.1.2 Radio Frequency Magnetron Sputtering (RFM-Sputtering)

Ag and Ag_yO thin films are grown by an RFM-sputtering system. The working gas, Ar and/or O_2 as the electrical discharge medium, bombards the target material of Ag and the Ag related thin films are deposited onto a quartz substrate. In this time, near the cathode surface, free electrons encounter Argon ($e^- + Ar \longrightarrow 2e^- + Ar^+$), and the accelerated ions charge multiplication collide on the target to produce the target atoms [6], and the yield atoms are collected on the substrate by exerting the electron field. As a result, the target atoms are deposited on the substrate as a thin film.

Magnetron sputtering is now considered the most effective process for the deposition of a wide range of thin film materials [7-11]. The main driving force behind this development has been the increasing demand for high-quality. Figure 2.3 illustrates the basic components of an RFM-sputtering system. Briefly, ionized Ar atoms bombard a sputtering target, thus releasing the molecules/atoms that form thin layers on a substrate.

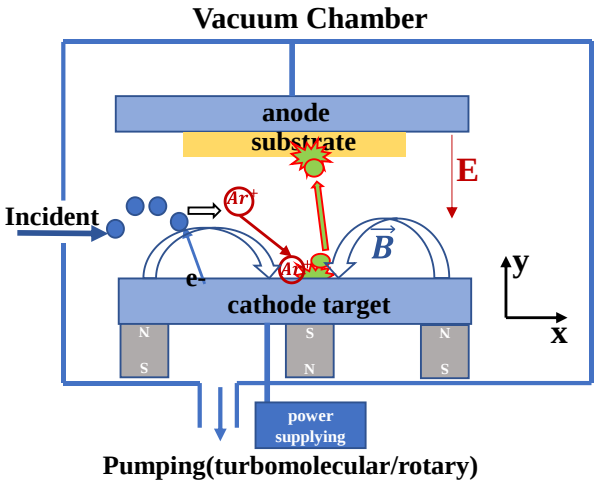

Fig. 2.3 Schematic illustration of RFM-sputtering system

2.2 Characterization Techniques

2.2.1 Spectroscopic Ellipsometry

The thickness of a film has significant effects on its every property. The varied types of films and their applications have generated different approaches for measuring film thickness. They are basically divided into optical and mechanical methods.

The film thickness of the ZnMgO and the ITO from my experiments were obtained by an optical method, which is from a spectroscopic ellipsometer (J.A. Woollm, W-VASE) fitting and calculated by the Cauchy model in the transparent region. Its structure illustration is shown in Fig 2.4.

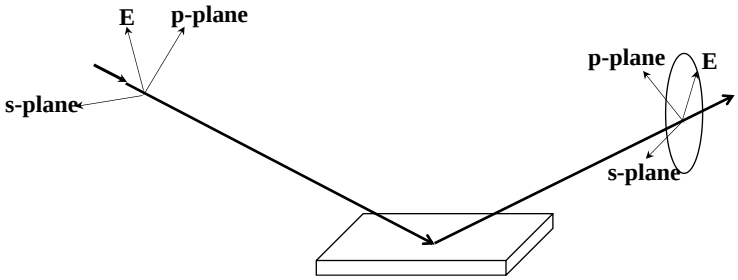

Fig. 2.4 Spectroscopic ellipsometer structure illustration

Ellipsometry is a technique to examine the thickness and optical constants of thin films with polarized light [12]. The light used is an electromagnetic wave, and the electric field oscillates perpendicular to the light beam direction. The magnetic field oscillates perpendicular to both the light beam direction and the electric field. If the two waves have different amplitudes or arbitrary phases, elliptically polarized light is generated. This is where the term ellipsometry comes from. When light is obliquely reflected from a sample, the incident and reflected beams define a plane of incidence. And changes in the state of polarization of light reflected from a sample surface at non-normal incidence is measured, namely measure the complex ratio of Fresnel reflection coefficients [13, 14], which is given by

$$\frac{R_p}{R_s} = \tan(\varphi)e^{i\Delta},$$

where R_p and R_s are the complex Fresnel reflection coefficient for light polarized parallel and perpendicular to the plane of incidence, φ and Δ are the traditional ellipsometry angles [14].

2.2.2 X-ray Diffraction

The crystal structure of all samples was analyzed by grazing incident X-ray diffraction (GIXD) spectra using CuKα radiation (Rigaku corp., Smart Lab, X-ray wavelength $\lambda = 1.5418$ Å, incident angle 0.35°).

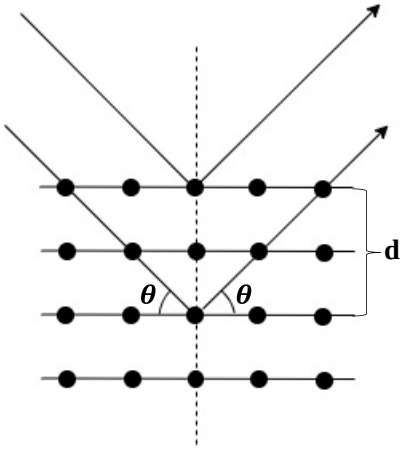

Fig. 2.5 The schematic diagram of Bragg diffraction from two parallel planes

X-ray methods have advantages because they are nondestructive and do not require elaborate sample preparation or film removal from the substrate. Using an X-ray of wavelength λ goes through and/or is partially scattered from many planes of a crystal grain. A crystal grain is generally structured by a systematic and periodic arrangement of atoms (or ions) in a three-dimensional array. As shown in Fig. 2.5, because the crystals are composed of a regular pattern of atoms, each crystal contains planes of atoms that are separated by a constant distance *d*, the critical angle of θ, at which the X-ray, scattered from the planes, the whole number of wavelengths $n\lambda$ is the X-ray passing through further the successive planes, *n* is an integer. Therefore, the distances between the planes are characteristic of the crystalline species. This relation can be described by Bragg's law:

$$n\lambda = 2d\sin\theta,$$

where diffraction can occur whenever the Bragg law is satisfied. Using a particular X-ray with constant wavelength λ of radiation is measured, and the angle of incidence θ of the primary radiation can be varied with the crystal planes.

2.2.3 Field Emission Scanning Electron Microscope and Energy Dispersive X-ray

Field emission scanning electron microscopy (FE-SEM) (Hitachi SU8020) equipped with an energy dispersive X-ray (EDX) detector (HOBIRA) was used for the atomic composition and surface morphology of ZnMgO and Ag_xO films.

Field emission scanning electron microscopy (FE-SEM) is an effective approach for mapping the sample surface morphology. An incident electron beam in the sample emits secondary electrons. The incident electron beam absorbed by the specimen and then the emitted electrons are collected in the field emission microscope [15]. A scanning electron microscope consists of an electron gun, a lens system, scanning coils, an electron collector, and a cathode ray display tube. Fig. 2.6 is the illustration diagram of FE-SEM. The electron energy is typically 5 - 30 keV for most samples, but for the insulating sample charging problems, the energy can be as low as several 10 eV.

The X-ray detector in the EDX is a reverse-biased semiconductor (usually Si or Ge) pin or Schottky diode. X-rays are absorbed into a solid according to the equation [16]

$$I(x) = I_0 \exp\left[\left(-\frac{\mu}{\rho}\right)\rho x\right],$$

where μ the mass absorption coefficient, ρ the detector material density, $I(x)$ the X-ray intensity into the detector, and I_0 the incident X-ray intensity. The mass absorption coefficient is characteristic of a given element at specified X-ray energies. Its value varies with the photon wavelength and with the atomic number of the target element generally decreasing smoothly with energy. The energy discontinuities appears immediately above the "absorption edge" energy, corresponding to the energy to eject a secondary electron from a shell.

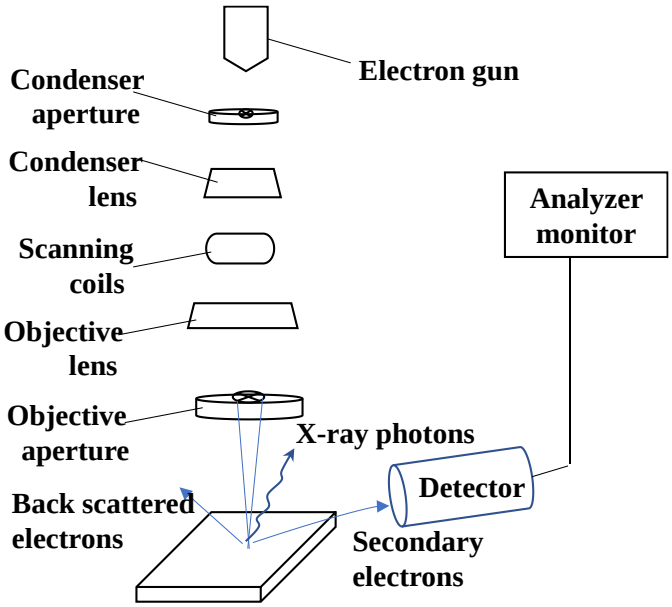

Fig. 2.6 The illustration diagram of FE-SEM

2.2.4 UV-visible Transmission Spectroscopy

UV-visible transmission spectroscopy is used for the measurement of the optical transmittance spectrum, which has a wavelength in the range from 200 to 2500 nm by using a UV-visible spectrometer (Hitachi UV-vis U-4100). And the band gap was then calculated and confirmed by the Tauc plot which was extracted from the transformation of transmittance spectra into absorption spectra.

The relation between the optical absorption coefficient α of a direct band gap (E_G) semiconductor near the band edge and the photon energy hv is given by the following equation [17, 18]:

$$\alpha hv = A(hv - E_G)^{1/2},$$

where A is a constant value and E_G is band gap. The film transmittance (T) around the absorption edge is approximated as $\exp(-\alpha t)$, where t is the film thickness. By then plotting $(\alpha hv)^2$versus photon energy hv, the band gap E_G can be confirmed by linear extrapolations of absorption region.

2.2.5 Resistivity and Hall Effect

The resistivity measurement is performed using the four-point probe method [19] [20]. A small current from a constant-current source is passed through the outer probes and the voltage is measured between the inner two probes. For a thin wafer with thickness W much smaller than either length a or width d, the sheet resistance R, is given by

$$R_s = \frac{V}{I}\,\mathrm{CF}\,\frac{\Omega}{\text{square}},$$

where CF is the correction factor. The resistivity is then

$$\rho = R_s W \quad \Omega \cdot cm,$$

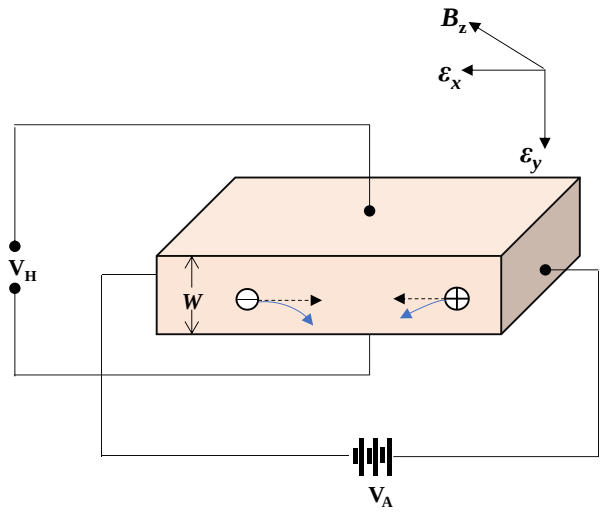

Fig. 2.7 Hall effect measurement basic setup

The carrier concentration is measured by the Hall effect method. Fig. 2.7 shows the basic setup [21] where an electric field is applied along the x axis and a magnetic field is applied along the z axis. For example, as the specimen is a p-type material, the Lorentz force $qv_x \times B_z$ exerts an average downward force on the holes, and the downward directed current causes a piling up of holes at the bottom side of the sample. As a result, an electric field E_y occurs. Since there is no net current along the y direction in the steady state, the electric field along the y axis (Hall field) exactly balances the Lorentz force. This Hall field can be measured externally and is given by

$$E_y = \left(\frac{V_y}{W}\right) = R_H J_x B_z,$$

where R_H is the Hall coefficient and is given by [22]

$$R_H = \frac{r(p - b^2 n)}{q(p + bn)^2},$$

where $b = \mu_n/\mu_p$ and r is the scattering factor, whose value lies between 1 and 2, depending on the scattering mechanism in the semiconductor.

2.2.6 X-ray Photoelectron Spectroscopy

X-ray photoelectron spectroscopy, also known as electron spectroscopy for chemical analysis (ESCA), is the high-energy version of the photoelectric effect discovered by Hertz in 1887. It is primarily used to identify chemical species on the sample surface, allowing all elements except hydrogen and helium to be detected. Hydrogen and helium can, in principle, also be detected, but this requires a very good spectrometer. When low energy photons (≤ 50 eV) are incident on a solid, they can eject electrons from the valence band, the effect is known as ultraviolet photoelectron spectroscopy (UPS). In XPS the photons that interact with core level electrons are X-rays. Electrons can be emitted from any orbital with photoemission occurring for X-ray energies exceeding the binding energy [23].

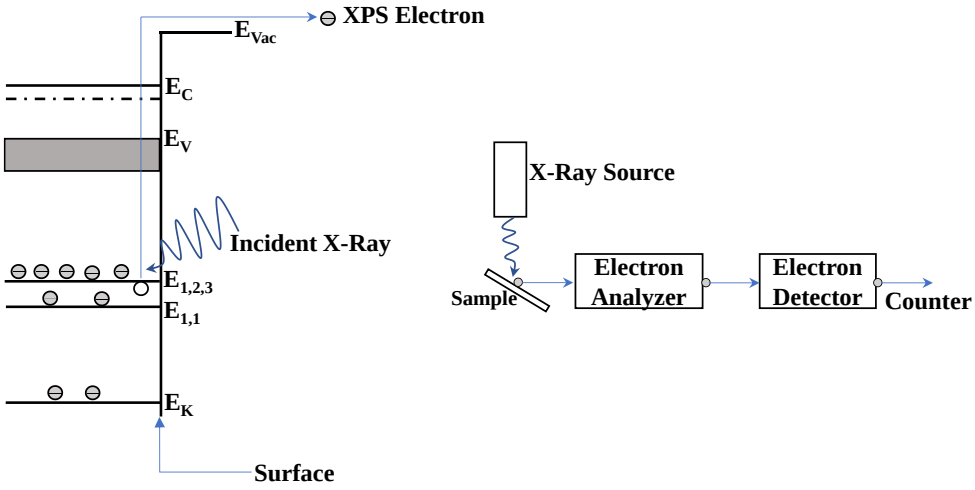

Fig. 2.8 Energy band diagram and the schematic XPS measurement

The method is illustrated with the energy band diagram and the schematic XPS principle as shown in Fig. 2.8. Primary X-rays with 1 to 2 keV energy eject photoelectrons from the sample [24, 25]. The binding energy of each emitted electrons can be determined using the equation:

$$E_B = E_P - (E_K + \phi),$$

where E_B is the binding energy (BE) of electrons, E_P is the energy of the X-ray photon used for measurement, E_K is the kinetic energy of the electron as measured by the instrument, and ϕ is the work function of the measured samples.

2.2.7 Photoelectron Yield Spectroscopy

The work function of 150 nm thick Ag and Ag_xO films on the quartz substrate was determined by photoelectron yield spectroscopy (PYS) (BUNKOUKEIKI Corp., BIP-KV202GD/UVT) under vacuum at room temperature. Fig. 2.9 shows the principle of PYS.

The monochromatized photon from the D_2 (30 W) lamp is used as the excitation light source. The density of yield photoelectrons (Y) of Ag_xO samples is detected by irradiated D_2 light with incremental photon energy ($h\nu$) scanning from 4 to 9.5 eV. The value of Y is thought to be proportional to the square root in the surface area of

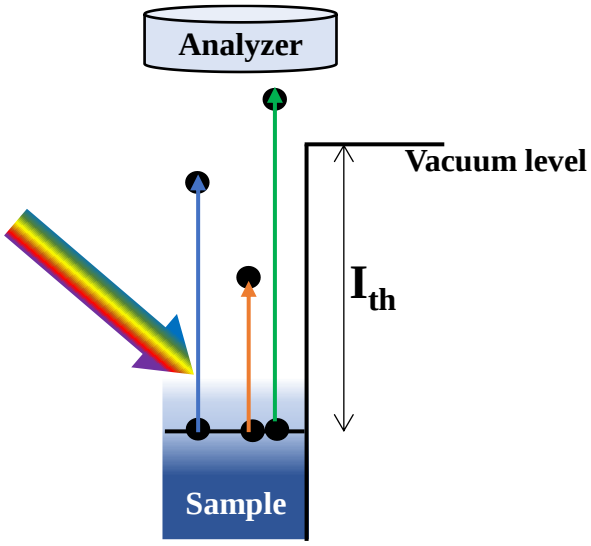

Fig. 2.9 PYS principle

hv over the threshold ionization energy (I_{th}) which is equal to the energy difference $E_0 - E_{\mathrm{F}}$ for Ag, or $E_0 - E_{\mathrm{v}}$ for Ag_yO, where E_0 is vacuum level, E_{F} is fermi level, E_{v} is valence band energy. I_{th} was evaluated through the following equation $Y \propto (hv - I_{\mathrm{th}})^{1/2}$ [26, 27] with plotting the hv versus $Y^{1/2}$ spectra then by linear extrapolations of $Y^{1/2}$.

2.3 References

[1] 川原村敏幸. "ミスト CVD 法とその酸化亜鉛薄膜成長への応用に関する研究." (2008). http://repository.kulib.kyoto-u.ac.jp/dspace/handle/2433/57270

[2] T. Kawaharamura, Jpn. J. Appl. Phys. 53, 05FF08 (2014).

[3] Tatsumi ISHIHARA, Yujin KONG, Shintaro IZUK, and Atsushi TAKAGAK, Journal of the Japan Petroleum Institute, 62, (6), 296-302 (2019).

[4] C. J. M. Fletcher Proc. R. Soc. Lond. A 1934 147, 119-128.

[5] Toshiyuki Kawaharamura et al., 2013 Jpn. J. Appl. Phys. 52 035501.

[6] J. H. Keller and W. B. Pennebaker, "Electrical Properties of RF Sputtering Systems," in IBM Journal of Research and Development, vol. 23, no. 1, pp. 3-15, Jan. 1979.

[7] Kelly, P. J.; Arnell, R. D. Magnetron sputtering: A review of recent developments and applications. Vacuum 2000, 56, 159–172.

[8] Musil, J.; Baroch, P.; Viček, J.; Nam, K.H.; Han, J.G. Reactive magnetron sputtering of thin films: Present status and trends. Thin Solid Films 2005, 1–2, 208–218.

[9] Alam, M. N.; Vasiliev, M.; Kotovb, V.; Alameh, K. Recent developments in magneto-optic garnet-type thin-film materials synthesis. Procedia Eng. 2014, 76, 61–73.

[10] Alam, M. N.; Vasiliev, M.; Alameh, K. $Bi_3Fe_5O_2$:Dy_2O_3 composite thin film materials for magneto-photonics and magneto-plasmonics. Opt. mater. Express 2014, 4, 1866–1875.

[11] Alam, M. N.; Vasiliev, M.; Alameh, K. Nano-structured magnetic photonic crystals for magneto-optic polarization controllers at the communication-band wavelengths. Opt. Quantum Electron. 2009, 41, 661–669.

[12] Jellison Jr, G. E., and J. W. McCamy. "Sample depolarization effects from thin films of ZnS on GaAs as measured by spectroscopic ellipsometry." Applied phys-

ics letters 61.5 (1992): 512-514.

[13] G. E. Jellison, Jr., 416 Thin Solid Films, 234 (1993) 416-422.

[14] R. W. Collins, Rev Sci Instrum 61, 2029–2062 (1990).

[15] V.E. Cosslett, "Fifty Years of Instrumental Development of the Electron Microscope," in Advances in Optical and Electron Microscopy (R. Barer and V.E. Cosslett, eds.), Academic Press, London, 10, 215–267, 1988.

[16] C-U Kim, N.L. Michael, Q.-T. Jiang, and R. Augur, "Efficient Electromigration Testing with a Single Current Source," Rev. Sci. Instrum. 72, 3962 – 3967, Oct. 2001.

[17] Hamberg,C. G. Granqvist, J. Appl. Phys. 60, R123 (1986).

[18] Franz Urbach, Physical Review, 92 (5)1324 (1953).

[19] W. F. Beadle, R. D. Plummer, and J. C. C. Tsai, Quick Reference Manual for Semiconductor Engineers, to be published.

[20] F. M. Smits, "Measurement of Sheet Resistivities with the Four-Point Probe," Bell Syst Tech. J., 37, 711 (1958).

[21] R. A. Smith, Semiconductors, 2nd ed., Cambridge University Press, London, 1979.

[22] E. H. Hall, "On a New Action of the magnet on Electric Currents," Am. J. Math., 2, 287 (1879).

[23] P. K. Gosh, *Introduction to Photoelectron Spectroscopy*, Wiley-Interscience, New York, 1983; D. Briggs and M.P. Seah (eds.), *Practical Surface Analysis*, Vol. 1: Auger and X-Ray Photoelectron Spectroscopy, Wiley, Chichester, 1990; J.B. Lumsden, "X-Ray Photoelectron Spectroscopy," in Metals Handbook, 9th Ed. (R.E. Whan, coord.), Am. Soc. Metals, Metals Park, OH, 10, 568–580, 1986; N. Martensson, "ESCA," in *Analytical Techniques for Thin Film Analysis* (K.N. Tu and R. Rosenberg, eds.), Academic Press, Boston, 1988, 65 – 109.

[24] C. Nordling, S. Hagstrom and K. Siegbahn, "Application of Electron Spectroscopy to Chemical Analysis," *Z. Phys.* 178, 433 – 438, 1964; S. Hagstrom, C. Nordling and K. Siegbahn, "Electron Spectroscopic Determination of the Chemical

Valence State," *Z. Phys.* 178, 439 – 444, 1964.

[25] J.G. Jenkin, R.C.G. Leckey and J. Liesegang, "The Development of X-Ray Photoelectron Spectroscopy: 1900 – 1960," *J. Electron Spectr. Rel. Phen*. 12, 1–35, Sept. 1977; J.G. Jenkin, J.D. Riley, J. Liesegang and R.C.G. Leckey, "The Development of X-Ray Photoelectron Spectroscopy (1900 – 1960): A Postscript," *J. Electron Spectr. Rel. Phen.* 14, 477 – 485, Dec. 1978; J.G. Jenkin, "The Development of Angle-Resolved Photoelectron Spectroscopy: 1900–1960," *J. Electron Spectr. Rel. Phen*. 23, 187 – 273, June 1981.

[26] W. Li, C. Stampfl, M. Scheffler, Physical Review B 68, 165412 (2003)

[27] Ishii Hisao, Compendium of Surface and Interface Analysis, 457-463(2018).

Chapter 3

Fabrication and characterization of $Zn_{1-x}Mg_xO$ thin film by Mist-CVD

Silicon based power devices are well commercialized and widely used in our daily lives. However, due to the limitation of the physical properties, power losses occur continuously. Therefore, an alternative material is required. Among the different candidate materials, ZnO has its several important advantages (higher electron mobility and exciton binding energy, good conductivity, etc.). Furthermore, the alloying of ZnO with MgO could form a tunable wide band (3.4 eV ~ 7.8 eV). The ZnMgO with a wide band gap has its promising advantages for power devices. In this chapter, we focus mainly on three directions to optimize ZnMgO properties: first, the influence of the support of H_2O as oxidant, second, is the influence of Mg content, and third, influence of the support of ozone on the ZnMgO properties.

3.1 Introduction

Recent developments in wide band gap semiconductors, such as GaN (3.5 eV at 300K) and ZnO (3.4 eV at 300K) [1], have made considerable progress in high-quality short-wavelength photonic devices [2-4] and high-power, high-frequency electronic devices [5, 6]. Such improvements are based on the breakthroughs in high-quality growth processes of these materials.

Many applications based on GaN films have been taken over by ZnO films, due to its similar properties as GaN films in some cases even better. For example, gallium is a relatively expensive metal, but zinc is cheaper and abundant [1]. In fact, ZnO has numerous advantages, such as bulk single crystals of fairly high-quality ZnO can be

produced [7], large-size ZnO substrates are available [8], and its exciton binding energy is 60 meV (GaN 24 meV) [9]. Furthermore, combination with CdO or MgO to form ZnCdO and ZnMgO alloys provides a wide and versatile band gap engineering because CdO, ZnO, and MgO have band gaps ranging from 2.4 eV [10] to 8.2 eV [11], which has satisfied the requirements of the optoelectronic device applications.

Various deposition methods have been developed on the growth of ZnO and ZnO alloys of optoelectronic devices, such as molecular beam epitaxy (MBE) [12, 13], pulsed laser deposition (PLD) [14, 15], physical vapor deposition (PVD)16), RF-Magnetron Sputtering [17, 18], chemical vapor deposition (CVD) [19~21]. In fact, all of these pre-mentioned deposition methods have been capable of growing high quality thin films, whereas, from the perspective of environmental protection and lower cost, alternatively, research is developing methods to improve quality and reduce costs. An example is the solution based deposition process [19], such as the sol-gel method [22, 23, 24], spin coating [25, 26], spray pyrolysis [27, 28, 29], and mist-CVD [30-36], which does not require vacuum condition and all reactions are carried out at atmospheric ambient. Thus, these advantages lower the cost of the deposition system and the energy consumption, but they would not be able to obtain as high quality as the vacuum-based process.

Although we have been aware of these shortcomings of the non-vacuum solution-based process, we recently reported the deposition of magnesium alloyed zinc oxide films by a fine channel mist-CVD system at atmospheric pressure [37], which consists of dual-solution-chambers and a mist mixing chamber. Such a separated dual solution chamber of the metal precursor solution can usefully prevent pre-interaction of the different metal atoms that dissolve in one solution chamber and can precisely control the metal atomic composition. Our intention is not only to reduce the cost, but also to acquire fairly high-quality thin films. The upgrades of the fine channel mist-CVD system comprise tri-solution chambers assembling with corresponding to three ultrasonic mist generators below and a mist mixing chamber installed in the vertical direction of

the middle of the tri-solution chambers. The two of the tri-solution-chambers are used for the solutions of Zn and Mg precursors and the other one is used for H_2O as an oxidant. Furthermore, the ZnMgO films can be deposited by introducing the carrier gas and the dilution gas (c.g. / d.g.) of nitrogen brought mist into the mixing chamber, and the extent of alloying and oxidization can be easily controlled by the concentration of the precursor solution and the flow ratio of the carrier gas and dilution gas.

3.2 The Effect of Different Supply Ratios of $[H_2O]/\{[Zn]+[Mg]\}$ on the Properties of $Zn_{1-x}Mg_xO$ Thin Films

3.2.1 Experimental Procedures

$Zn_{1-x}Mg_xO$ (ZnMgO) films were deposited on quartz substrates in an atmospheric pressure third-generation mist-CVD system (3rd mist-CVD) [38] which has tri-solution-chambers and a mist mixing chamber. High-purity nitrogen (99.99% from a gas generator) with a velocity of 1 m/s was used as the carrier gas and the dilution gas (c.g / d.g.).

Table 3-1 Experiment conditions of the effect of different supply ratios of $[H_2O]$ / {[Zn] + [Mg]}

	Chamber A	Chamber B	Chamber C
Sour. Conc.	MeOH + $Zn(acac)_2$ 50 mM	MeOH + $Mg(acac)_2$ 20 mM	MeOH + H_2O 0 % ~ 100 %
c.g. / d.g. (l / min)	2.5 / 2.5	1.0 / 4.0	2.0 / 3.0
Growth time & Temp.	600 s & 400 ℃		
Ultrasonic transducer	2.4 MHz, 24 V - 0.625 A		

In this experiment, three types of precursor solutions were prepared as the following: zinc acetylacetonate ($Zn(acac)_2 \cdot 2H_2O$) dissolving in methanol with the setting of the solution concentration as 50 mM, magnesium acetylacetonate dihydrate ($Mg(acac)_2$ 98% purity) dissolving in methanol with the setting of the solution concentration as 0.02 mM, and deionized (D.I.) water diluting in methanol with the

change concentration from 0%, 3 %, 10 %, 15 %, 30 %, 50 %, to 100 % (i.e., D.I. water : Methanol = 3 : 97 = 3 %). Then the mists of the precursor solutions of $Zn(acac)_2 \cdot 2\ H_2O$, $Mg(acac)_2$, D.I. water were gathered into the mixing chamber by the three-path silicone tube of three paths and then all the mists were introduced into the reactor with a fine channel structure by one silicone tube [39, 40]. The gas flow rate in each line was 5 l/min, and the total gas flow rate is 15 l/min. The reactor was pre-heated by the bottom hot plate at the bottom and its temperature was set at 400 ℃, but the deposition temperature was stabilized at 400 ℃ ± 3 ℃. The quartz substrates were cleaned with acetone, isopropyl alcohol and deionized (D.I.) water for 2 min, respectively, and lastly followed by drying with an N_2 gas gun. The details of the experiment conditions are summarized in Table 3-1.

3.2.2 Results and Discussions

The growth rate profile of films deposited in different supply ratios of H_2O / {[Zn] + [Mg]} is shown in Fig. 3.1 (a). While increasing the H_2O concentration to 30 %, the growth rate reached its maximum value around 114 nm/min. And after continuing to increase the H_2O concentration to 100 %, the growth rate started to decrease to 47 nm/min which is equal to the growth rate of the H_2O concentration of 3 %. Fig 3.1 (b) shows the variety of roughness with increasing supply ratios of H_2O / {[Zn] + [Mg]}. The roughness increased monotonically with increasing supply ratios of H_2O / {[Zn] + [Mg]}. The roughness was floating between 60 and 70 nm.

The ZnMgO band gaps with different supply ratios of H_2O /{[Zn]+[Mg]} are shown in Fig. 3.1 (c), which were extracted from the transformation of transmittance spectra into absorption spectra and then confirmed by the Tauc plot. The absorption edges are distributed in two groups. The first group is the samples grown from the H_2O concentration of 0%, there is a slightly blue-shift, which ended at 3.2 eV. This small shift behavior is thought to be due to variations in the Mg supply amount, but it shows that the amount of Mg incorporation into the thin film hardly changes even

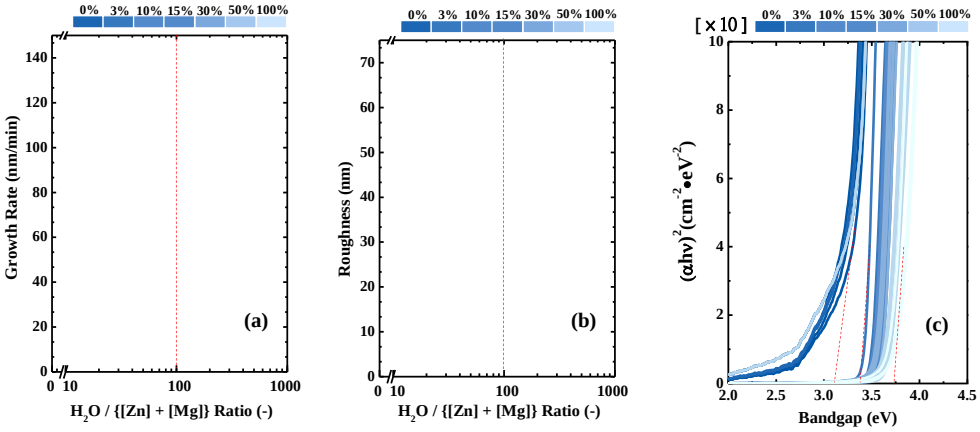

Fig. 3.1 (a) Growth rate (b) Roughness (c) Band gaps changing tendency as a function of H_2O / {[Zn] + [Mg]} ratio in the Mist phase

when the Mg supply amount increases. In other words, this suggests that the amount of Mg incorporation cannot be increased without supplying an oxygen source. The second group is the samples grown from the increase in H_2O concentration from 3 % to 100 %, corresponding to the supply ratios of H_2O /{[Zn]+[Mg]} increased from approximately 10 to 900. The absorption edge shifted from 3.4 eV to 3.83 eV. This suggests that during increasing the H_2O concentration and increasing carrier gas, the larger numbers of OH^- ions were input into the reaction chamber, so there is more po-

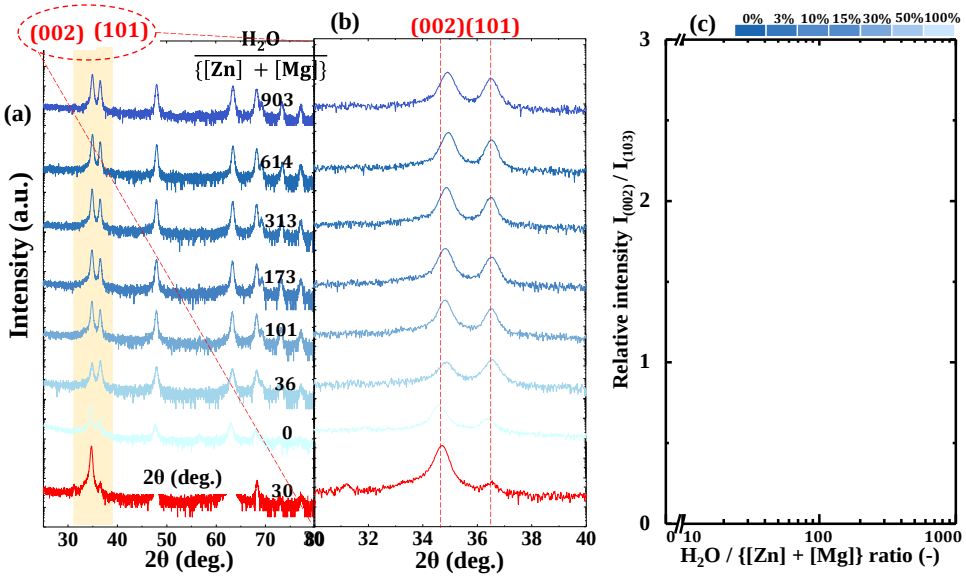

Fig. 3.2 (a) GIXD spectrum of different [H_2O] / {[Zn] + [Mg]} supply ratio (b) magnification of the (002) peak from 30° to 40°. (c) Intensity ratios of GIXD peak from ZnO (002) to that from ZnO (103) against [H_2O] /{[Zn]+[Mg]} supply ratios

tential to interact with Zn and Mg precursors films.

Figure 3.2 (a) shows the GIXD spectrum of the various supply ratios of H_2O / {[Zn] + [Mg]} of ZnMgO films. The spectra in red show the ZnO film, which has an exclusive stronger (002) peak, providing a comparison with ZnMgO. Therefore, there is a clear observation of the influence of the Mg content. When Mg c.g. / d.g. was fixed at 1.0 / 4.0 for all specimens, on that the grown films were obtained as the polycrystalline structure of the mixture of the weaker ZnO (002) peaks and gradually appeared (101) peaks. Furthermore, as the supply ratios of H_2O / {[Zn] + [Mg]} increased, the peak position of the plane (002) shifts from 34.7° for the supply ratios of H_2O / {[Zn] + [Mg]} = 0 to 34.9° for the supply ratios of H_2O / {[Zn] + [Mg]} = 900 as seen in Fig. 3.2 (b). The intensity ratios of $I_{(002)}$ / $I_{(103)}$ are shown in Fig. 3.2 (c). $I_{(002)}$ / $I_{(103)}$ was decreased dramatically from 240 to 29. However, after increasing the H_2O concentration to 30%, 50% and 100%, that is, the supply ratios of the H_2O / {[Zn]+[Mg]} from 220 to 900, the intensity ratios of $I_{(002)}$ / $I_{(103)}$ had a slight increase tendency.

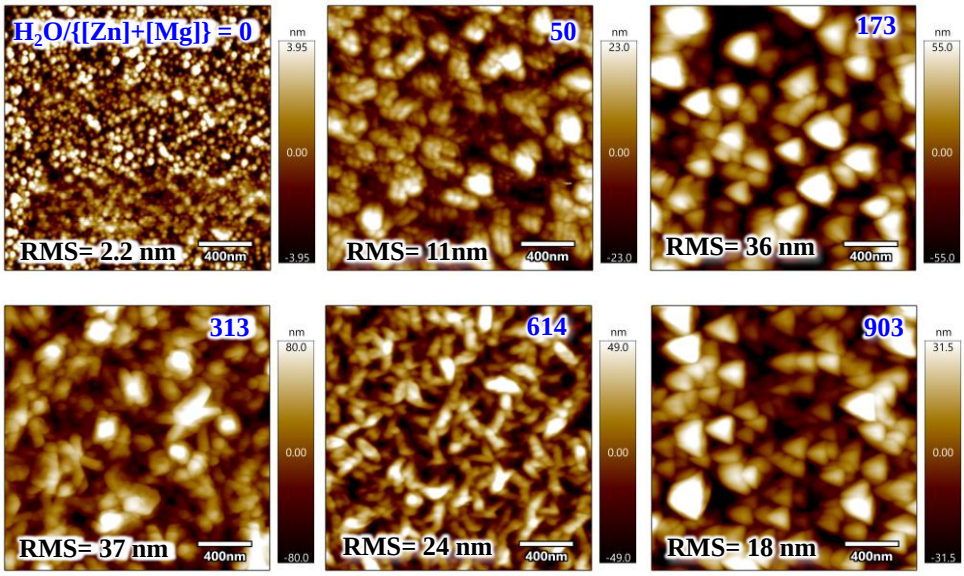

Fig. 3.3 AFM micrographs with different H_2O /{[Zn]+[Mg]} supply ratios

The surface root-mean-square (RMS) roughness was derived from the atomic-force microscope (AFM) image of 2 μm × 2 μm scanning as shown in Fig. 3.3. For without introducing water, that is, H_2O /{[Zn]+[Mg]} = 0, the RMS = 2.2 nm. And after sup-

plying water and increasing the H_2O /{[Zn]+[Mg]} ratio, the surface tended to become rough for ZnMgO. This is probably due to the more complicated chemical reactions and/or the non-uniform instability of the deposition system.

3.2.3 Summary

The results indicate that it was necessary to supply an oxygen source (H_2O) in order to increase the amount of Mg mixed into zinc oxide under this experimental condition. At the same content of Mg, the optical band gaps of the ZnMgO films were widen from 3.22 to 3.83 eV by increasing the H_2O concentration. The supply ratio of [H_2O]/{[Zn]+[Mg]} has a strong influence on growth rate and crystal orientations.

3.3 The Influence of Different Mg Content on the Properties of ZnMgO Thin Films

3.3.1 Experimental Methods

The third-generation mist-CVD system (3rd mist-CVD) was used for the preparation of $Zn_{1-x}Mg_xO$ thin films under atmospheric pressure at 400 ℃ on quartz substrates. ZnMgO was formed by supplying the Zn source and the Mg source from the two separate solution tanks. Their component ratio was manipulated by fixing the carrier gas/dilution gas (c.g. / d.g.) flow rate of the Zn source (Zn c.g. / d.g.) and changing the c.g. / d.g. flow rate of the Mg source (Mg c.g. / d.g.) under the same total gas flow rate. Each quartz substrate was ultrasonically precleaned for 2 min, respectively, in acetone, isopropyl alcohol, and deionized (D.I.) water followed by drying in an N_2 gas gun. The experiment conditions are summarized in Table 3-2.

The films thicknesses of the ZnMgO were obtained from a spectroscopic ellipsometer (J.A. Woollm, W-VASE). The atomic composition and surface morphology of ZnMgO films were analyzed by energy dispersive X-ray (EDX) measurement using scanning electron microscopy (SEM) (Hitachi SU8020) equipped with a (HOBIRA) detector. The crystal structure was analyzed by grazing incident X-ray diffraction

(GIXD) spectra using CuKα radiation (Rigaku corp., Smart Lab, X-ray wavelength $\lambda = 1.5418$ Å, incident angle 0.35°). The optical transmittance spectrum of ZnMgO films was measured in the range from 200 to 2500 nm using a UV-visible spectrometer (Hitachi UV-Vis U-4100), and the band gap was then calculated and confirmed by Tauc plot, which was extracted from the transformation of transmittance spectra into absorption spectra. The electric properties of 150 nm ZnMgO films were measured by Hall System (Accent HL5500) in the Van der Pauw configuration.

Table 3-2 Mist-CVD deposition conditions of ZnMgO with different Mg content

	Chamber A	Chamber B	Chamber C
Sour. Conc.	MeOH + $Zn(acac)_2$ 50 mM	MeOH + $Mg(acac)_2$ 20 mM	MeOH + H_2O 97 : 3
c.g. / d.g. (l / min)	2.5 / 2.5	0.5 / 4.5 ~ 2.0 / 3.0	2.0 / 3.0
Growth time & Temp.	600 s & 400℃		
Ultrasonic transducer	2.4 MHz, 24 V, 0.625 A		

3.2.2 Results and Discussions

Fig. 3.4 (a) shows the EDX spectra of the atomic compositions of the ZnMgO films with different Mg c.g. / d.g. using the Mist-CVD system. The X-ray intensity was normalized by the intensity of the Si Kα line. To avoid the influence of oxygen from the quartz substrates, we used Si substrates for this EDX measurement. An accelerating voltage of 5 keV was applied at five randomly selected points on the surface of ZnMgO, which revealed the atomic composition at those points. The atomic composition of the surface as a whole was then calculated as the average of the atomic compositions at these five points. With the change in the flow rate of Mg c.g. / d.g. from 0.5 / 4.5 to 2.0 / 3.0, the atomic composition of Mg increased from 0.08 to 0.23. Fig. 3.4 (b) shows the variation of the Mg content (x) with different flow ratios of [Mg]. It has been confirmed that the variation in the Mg content in the grown ZnMgO

films was consistent with the experimental conditions of an increased flow ratio of [Mg]. The atomic compositions of ZnMgO are summarized in Table 3-3.

Table 3-3 The atomic composition of ZnMgO

Mg c.g. / d.g.	Atomic composition			$x = \frac{[Mg]}{[Mg + Zn]}$
	O	Zn	Mg	
0.5 / 4.5	54.1	42.4	3.6	0.08
1.0 / 4.0	55.2	37.1	7.7	0.17
1.5 / 3.5	58.3	33.1	7.8	0.19
2.0 / 3.0	55.8	33.7	10.4	0.23

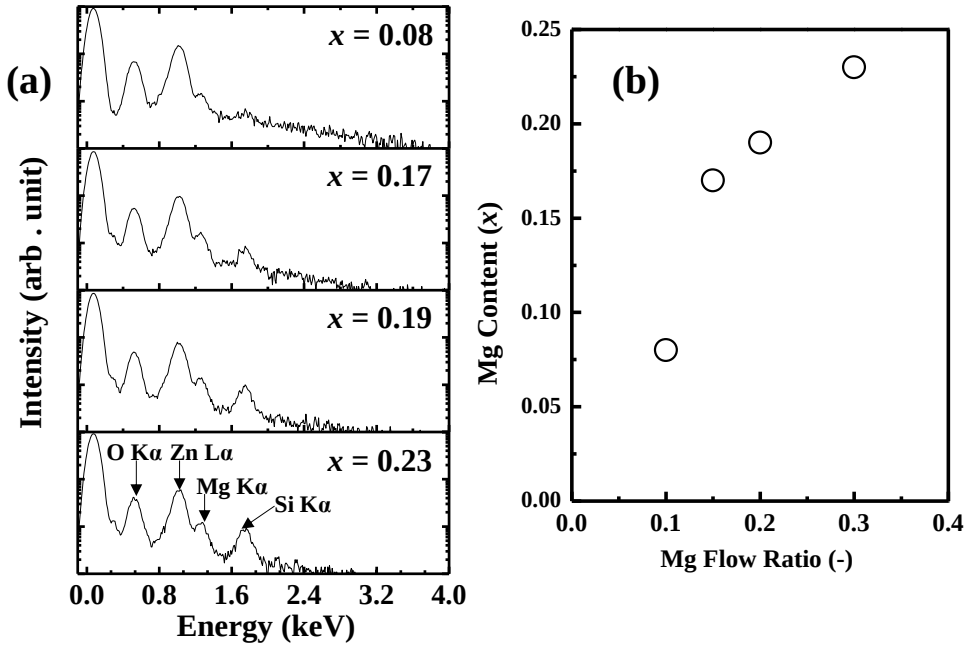

Fig. 3.4 EDX spectra with different Mg c.g. / d.g. of ZnMgO

Fig. 3.5(a) shows Tauc plots extracted from the transmittance spectrum of ZnMgO films. The absorption edge was blue-shifted and the band gap was tuned from 3.3 eV ($x = 0.00$) to 3.7 eV ($x = 0.23$) by incorporating Mg content in the films. Fig. 3.7 (b) shows the resistivity (ρ) and carrier concentration (N_H) of the ZnMgO films. When the Mg composition of Mg $x = 0.00$, the resistivity ρ = 0.66 Ω·cm, N_H = 7.44 × 10^{20} cm^{-3} and as the Mg content increased to 0.08, ρ increased to 1.4 × 10^5 Ω·cm, N_H declined to 3.9 × 10^{19} cm^{-3}; and after Mg x > 0.08, high resistivity of the films did not allow reliable Hall effect measurements for carrier concentrations. Meanwhile, as Mg x = 0.23, ρ increased to 1.58 × 10^8 Ω·cm. These results suggest that ZnMgO films

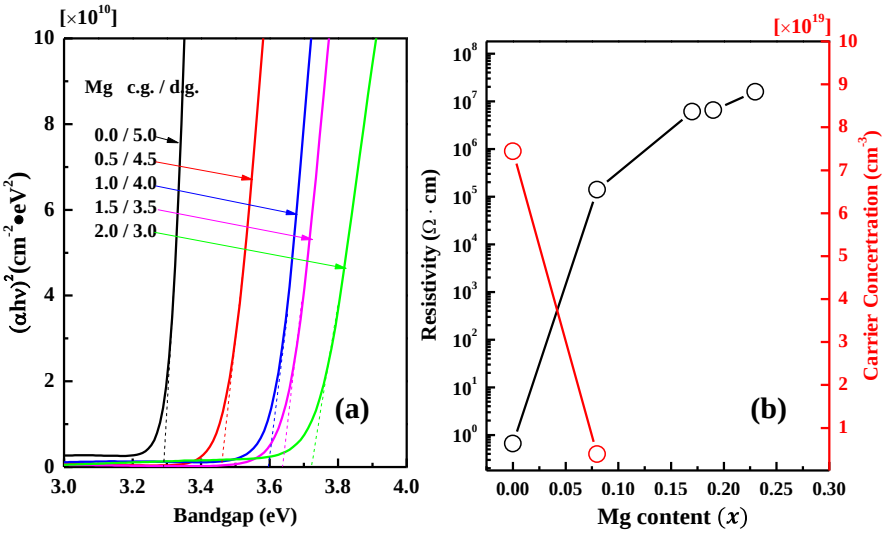

Fig. 3.5 Mg content dependence of (a) Absorption spectra with Tauc plots (b) Resistivity and Carrier concentration

were transformed from a conductor to a semiconductor or insulator by increased the Mg content.

The crystal structures and morphology images of ZnMgO with different Mg compositions are shown in Fig. 3.6 and Fig. 3.7. As can be seen, even a very small amount of Mg content has a tremendous impact on the crystal structure and morphology of the films. From the results of the GIXD spectra of Fig. 3.6., the crystal structure of the films could be observed by five main peaks, namely (002), (101), (102), (103) and (112). When the Mg content x = 0.00, the grown film was pure ZnO, which presented a sharp diffraction peak (002) with the strongest diffraction intensity. This indicates that the atoms were mainly stacked along the c-axis direction and such crystals showed wurtzite sphere shaped structures from the morphology observation of the SEM measurement results, as shown in Fig. 3.7 in the first image. When the Mg content x increases from 0.00 to 0.23, the crystal structure reveals the polycrystalline structure of the ZnO/MgO mixture. It suggests that the crystals varied to be a combination of the five-fold coordinated hexagonal structure of MgO [41] and the wurtzite structure of ZnO. The magnification of the (002) peaks (2θ = 34° to 36°) is shown on the right side of Fig. 3.6. The (002) peak center positions were shifted from 2θ = 34.7° to 34.96°, and the intensities on the c-axis were compressed by incorporating Mg

atoms. Such variations may have been caused by the substitution of Zn^{2+} by Mg^{+2} due to the divergences in the electronegativity of Zn^{2+} and Mg^{+2}. The grain size became visibly smaller, which may be caused by the different atomic radii of Zn and Mg [41-44].

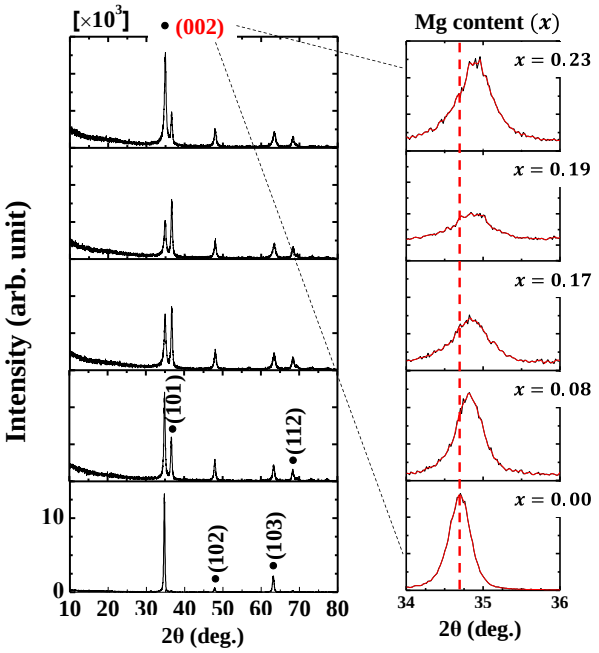

Fig. 3.6 GIXD spectrum of Mg content (x) dependence

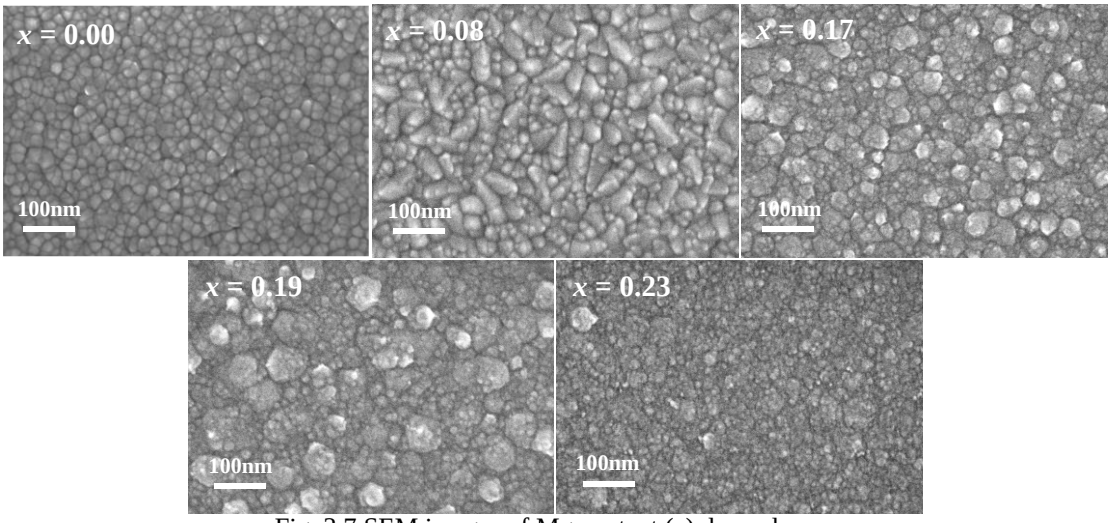

Fig. 3.7 SEM images of Mg content (*x*) dependence

3.3.3 Summary

The ZnMgO films that were prepared using the mist-CVD system present a poly-

crystal structure of the ZnO/MgO mixture with increasing incorporation of the Mg content. Furthermore, by alloying the Mg atom (x = 0.00 ~ 0.23), the band gaps of ZnMgO have been shown to vary from 3.3 eV to 3.7 eV, the carrier concentration is obtained 3.9×10^{19} cm^{-3} (x = 0.08), and the resistivity increases from 0.66 Ω·cm (x = 0.00) to 1.58×10^{8} Ω·cm (x = 0.23). This suggests that the ZnMgO film grown is transformed from a conductor to a semiconductor or an insulator.

3.4 The Effect of Ozone on the Properties of $Zn_{1-x}Mg_xO$ Thin Films

3.4.1 Experimental Methods

The $Zn_{1-x}Mg_xO$ films were deposited on quartz substrates in an atmospheric pressure third-generation mist-CVD system (3rd mist-CVD) which has tri-solution chambers set separately for the three precursors: $Zn(acac)_2$ precursor, $Mg(acac)_2$ precursor, and H_2O support solution, respectively, and another big chamber is set to mix all the mist together. The zinc acetylacetonate ($Zn(acac)_2 \cdot 2H_2O$) dissolve in methanol with the setting solution concentration of 50 mmol/l, magnesium acetylacetonate dihydrate ($Mg(acac)_2$ 98 % purity) dissolve in methanol with the setting solution concentration of 20 mmol/l, and deionized (D.I.) water dilute in methanol with the setting concentration of 3 %, and assistant gas O_3 is introduced directly into the reaction chamber. The experiment conditions and the parameters of the mist-CVD system are summarized in Table 3-4.

Table 3-4 Experiment conditions of ozone effects on the properties of ZnMgO

	Chamber A	Chamber B	Chamber C	Assistant Gas
Sour. Conc.	MeOH + $Zn(acac)_2$ 50 mM	MeOH + $Mg(acac)_2$ 20 mM	MeOH + H_2O 3 %	O_3 10 g / m^3
c.g. / d.g. (l / min)	2.5 / 2.5	0.0 / 5.0 ~ 5.0 / 0.0	2.0 / 3.0	0
				1.5
Growth time & Temp.	600 s & 400℃			
Ultrasonic transducer	2.4 MHz, 24 V, 0.625 A			

3.4.2 Results and Discussions

Ozone is a powerful oxidizing agent. When used in CVD processes, it can lead to an increase in the oxidation of metal precursors, which may affect the growth rate of the thin films. Fig. 3.8 shows the EDX spectra of the ZnMgO film of the atomic compositions compared to the supply of O_3 (Fig.3.8 (b) with O_3) with different Mg c.g. / d.g. using the mist-CVD system. The X-ray intensity was normalized by the intensity of the Si Kα line. In the case of without O_3, as increasing Mg c.g. / d.g. flow rate from 0.0 / 5.0 to 3.0 / 2.0, but there is no Mg peak showing up in the spectrum. However, under the same condition after introducing O_3, the peak of Mg is present in the Kα line at 1.25 keV, and the atomic composition of Mg increased from 0.00 to 1.39. This increase in Mg composition is mainly caused by the reactive oxygen species of singlet oxygen (O_2^*) and the ozone radical ($O\bullet$) that is generated from thermal decomposition of the ozone [45]:

$$O_3 \rightarrow O_2 + O\bullet$$

$$O_3 + O_2 \rightarrow O_2^* \ or \ O\bullet + O_2$$

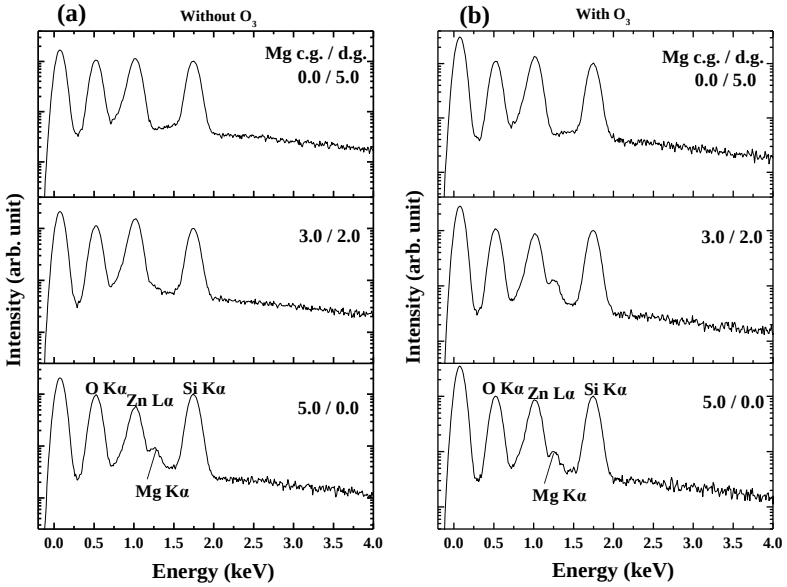

Fig. 3.8 EDX spectrum of ZnMgO thin films in comparison between (a) without O_3 and (b) with O_3

Reactive oxygen species (O_2^* and O•) initiate a chain reaction by attacking the precursor substance (Zn- and Mg-). Therefore, the reactive oxygen slightly increases in the incorporation of Mg in the ZnMgO thin film with an increase in the carrier gas of the Mg precursor. The atomic compositions of ZnMgO and resistivity compared with those without O_3 and with O_3 are summarized in Table 3-5.

Table 3-5 The atomic composition of ZnMgO without O_3 and with O_3

	Mg c.g. / d.g.	C	O	Zn	Mg	Si	Resistivity (Ω·cm)
With-out O_3	0.0 / 5.0	12.1	67.36	0.15	--	20.98	2.31E+06
	3.0 / 2.0	12.01	68.74	0.17	--	19.14	5.08E+05
	5.0 / 0.0	10.56	65.76	0.1	1.01	22.57	7.53E+04
With O_3	0.0 / 5.0	12.53	67.3	0.12	--	20.58	2.55E+06
	3.0 / 2.0	11.5	66.1	0.1	1.39	21	8.24E+05
	5.0 / 0.0	12.72	66.22	0.12	0.97	19.97	2.66E+09

And the atomic composition with and without O_3 introduce against the amount of Mg source plot as shown in Fig. 3.9 (a). There was no obvious improvement between supporting with O_3 and without O_3. Fig. 3.9 (b) shows the growth rate profiles at different Mg alloying concentrations with O_3 and without O_3. The alloying concentration of Mg was modified by the amount of carrier gas (l/min). From observation of the

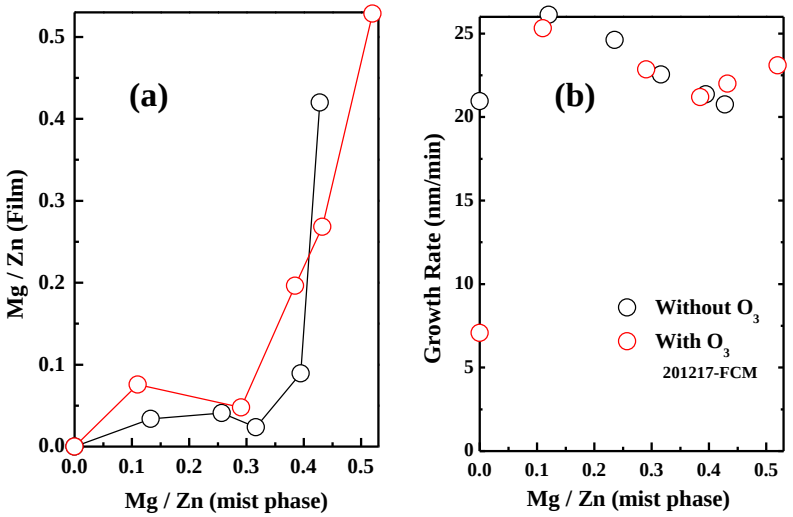

Fig. 3.9 Mg / Zn content in film versus Mg / Zn content in Mist

growth rate tendency, there is no shift between every point position appearing at almost the same position of 25 nm/min in both cases with O_3 and without O_3 in the case of the Mg carrier gas is 1.0 l/min. And, after increasing the Mg alloying concentration, the growth rate slightly decreased. But while the carrier gas was set at the same volume, almost no differences were observed in the corporation of Mg with O_3 and without O_3. The references [46, 47] report that O_3 can improve doping efficiency and metal incorporation into ZnO films. However, such a tendency was not observed in this experiment.

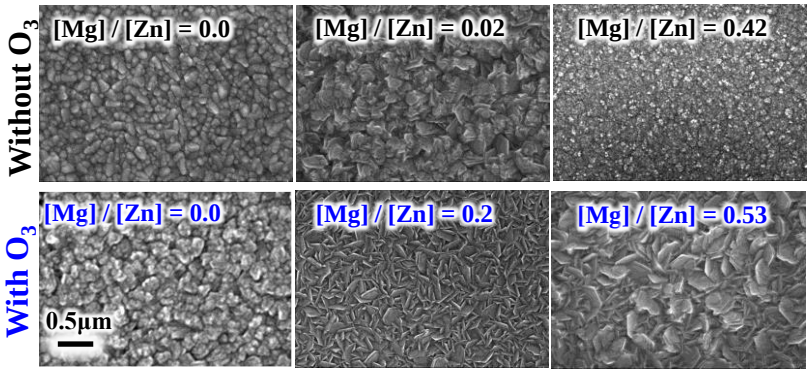

Fig. 3.10 SEM micrographs with different [Mg] / [Zn] ratio in the film

Ozone can also influence the surface morphology and roughness of the deposited films. The presence of oxygen radicals can lead to different growth modes, resulting in various surface structures. And the comparison of the influence of O_3 on the surface morphology of ZnMgO is shown in Fig. 3.10. The top surface of the samples grown without O_3 looks smooth. In Mg/Zn = 0, which means that there is no Mg alloy in the film, the upper surface presents a grain of the sphere shape and when the Mg content increased, the surface became rough. With the O_3 group, morphology looks rough than those of the group without O_3.

The comparison of GIXD spectra in (a) without O_3 and (b) with O_3 is shown in Fig. 3.11. For the without O_3 case, there were five main peaks appearing as (002), (101), (102), (103) and (112) separately; in Mg c.g. / d.g. $\leq$ 2.0 / 3.0, the deposited films presented a strong signal of the diffraction peak (002), but the other four peaks were constantly without obvious changing; with increasing Mg c.g. / d.g. from 0.0 / 5.0 to

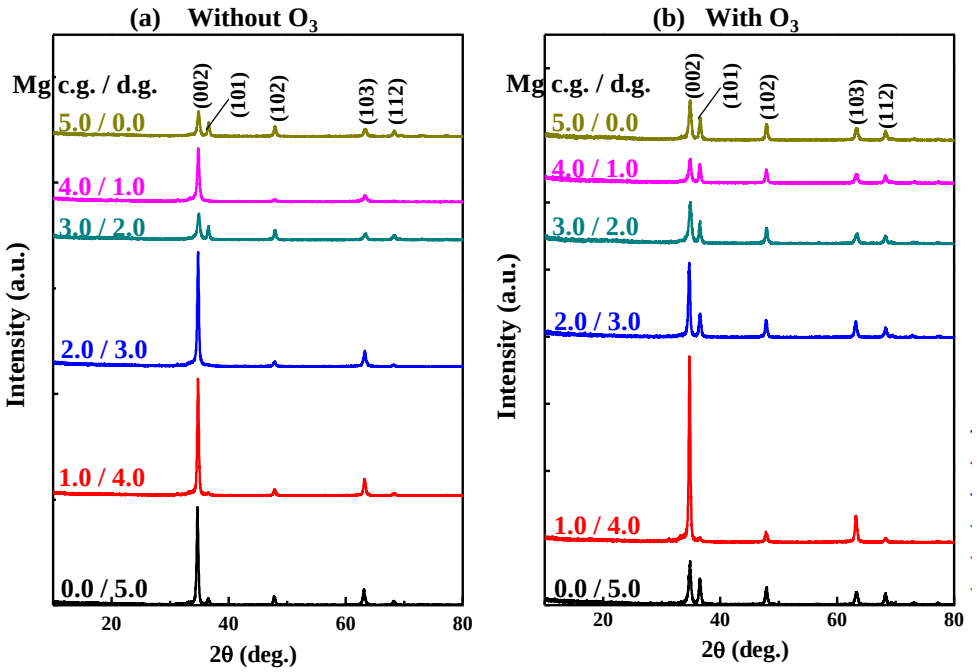

Fig. 3.11 GIXD spectrum of ZnMgO in comparison between (a) with O_3 and (b) without O_3

5.0 / 0.0, the intensity of the crystal peak of (002) decreased significantly, and another small peak (101) appeared next to the peak (002) and the other three peaks did not show obvious changes. Meanwhile, for the case of the samples with O_3 under the same conditions, they had the same tendency of changing, but the peak (101) had a constant intensity after Mg c.g. / d.g. increased to 2.0 / 3.0. This may cause that the introduction of O_3, increased the interaction between Zn and Mg, and the incorporation of Mg might create defects, which resulted in the having polycrystal grain of the grown ZnMgO films.

Fig. 3.12 shows Tauc plots extracted from the transmittance spectrum of ZnMgO films. We can see that in the case of without O_3, as the Mg c.g. / d.g. was increased from 0.0 / 5.0 to 5.0 / 0.0, the absorption edges were blue-shifted and the band gap waas widened from 3.2 eV to 3.6 eV. When comparing the results with the group with O_3, they had the same tendency to blue shift, and the band gaps widened to 3.7 eV but with more steep absorption edges. These results indicated that after introducing O_3, due to reactive oxygen species, more Mg is involved in the deposited films, and causing defect levels within the bandgap, and these defects can trap charge carriers, lead-

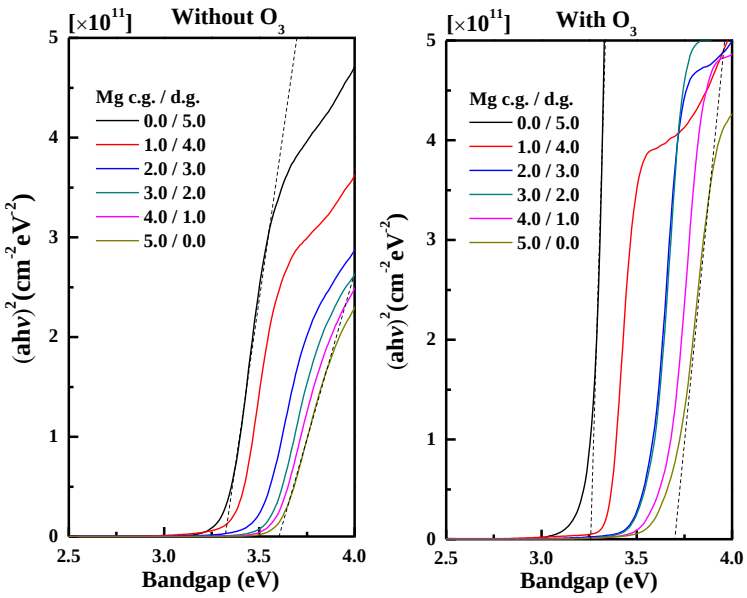

Fig. 3.12 Absorption spectrum of ZnMgO in comparison between without O_3 and with O_3

ing to new absorption peaks or shifts in the existing ones.

3.4.3 Summary

From the comparison of the experiment without & with O_3, we found that ozone can influence the incorporation of Mg into the ZnO lattice during growth. However, from the growth rate, top surface, and band gap data, there was no obvious improvement between without O_3 and with O_3 supporting.

3.5 Conclusions

In this chapter, ZnMgO films were deposited by mist-CVD and investigated in three different directions:

1) Investigation of the influence of the different supply ratios of H_2O / {[Zn] + [Mg], with an increase in the supply ratio of H_2O / {[Zn] + [Mg]} from 0 to 903. The crystallinity of (002) had degenerate and the peak center shifted by 0.28 deg. H_2O / {[Zn] + [Mg]} around 200, the growth rate reached the highest value and afterwards the roughness decreased. From the results of this experiment we can see that 3 % of

H_2O has good balance in the growth rate, roughness, and the intensity ratio of $I_{(002)}/I_{(103)}$. Therefore, the condition of 3 % H_2O has used for HJDs deposition used.

2) Investigation of the influence of different Mg content. With increasing incorporation of the Mg content (Mg c.g./d.g. increasing from 0.0 / 5.0 to 2.0 / 3.0), by alloying the Mg atom (x = 0.00 ~ 0.23) E_g = 3.3 eV ~ 3.7 eV, carrier concentration from N_e= 7.44×10^{19} (x = 0.0) to N_e= 3.9 × 10^{19} cm^{-3} (x = 0.08), and the resistivity increases from 0.66 Ω·cm (x = 0.00) to 1.58 × 10^8 Ω·cm (x = 0.23). The ZnMgO films tended to be the polycrystal structure, and the morphology varied to be the combination of the five-fold coordinated hexagonal structure of MgO and the wurtzite structure of ZnO.

3) Investigation of the influence of O_3, compared to without O_3 and with O_3. There was no obvious improvement.

Therefore, from the single layer experiment of mist-CVD ZnMgO, the condition for HJDs was selected: Chamber A of H_2O supporting: 3%, c.g. / d.g. = 2.0 / 3.0, Chamber B of Zn precursor: 50 mM, c.g. / d.g. = 2.5 / 2.5, Chamber C of Mg precursor: 20 mM, c.g. / d.g. = 0.0 / 5.0 ~ 2.0 / 3.0.

3.6 References

[1] Bernard Gil, Phys. Rev. B 64, 201310(R) (2001).

[2] S. C. Jain, M. Willander, J. Narayan, et al., Journal of Applied Physics 87, 965 (2000).

[3] G. Yadav, S. Dewan, M. Tomar, Optical Materials 126, 112149 (2022).

[4] S. Nakamura, G. Fasol, The Blue Laser Diode (Springer, Berlin, 1997).

[5] K. Tominaga, N. Umezu, I. Mori, T. Ushiro, T. Moriga, I. Nakabayashi, Thin Solid Films 334, 35-39 (1998).

[6] J. D. Albrecht, P. P. Ruden, S. Limpijumnong, et al., Journal of Applied Physics 86, 6864 (1999).

[7] D. Ehrentraut, H. Sato, Y. Kagamitani, H. Sato, A. Yoshikawa, T. Fukuda, Prog. Cryst. Growth Charact. Mater. 52, 280 (2006).

[8] E. Ohshima, H. Ogino, I. Niikura, K. Maeda, M. Sato, M. Ito, and T. Fukuda, J. Cryst. Growth 260, 166 (2004).

[9] K. Torii, T. Deguchi, T. Sota, K. Suzuki, S. Chichibu, S. Nakamura, Phys. Rev. B 60, 4723 (1999).

[10] F. P. Koffyberg, Phys. Rev. B 13, 4470 (1976).

[11] A. Ohtomo, M. Kawasaki, T. Koida, K. Masubuchi, H. Koinuma, Y. Sakurai, Y. Yoshida, T. Yasuda, Y. Segawa, Appl. Phys. Lett. 72, 2466 (1998).

[12] Ohkubo, Y. Matsumoto, A. Ohtomo, T. Ohnishi, A. Tsukazaki, M. Lippmaa, H. Koinuma, M. Kawasaki, Appl. Surf. Sci. 159-160, 514-519 (2000).

[13] Y. Chen, D. M. Bagnall, H. Ko, K. Park, K. Hiraga, Z. Zhu, T. Yao, J. appl. Phys. 84, 3912 (1998).

[14] S. Hayamizu, H. Tabata, H. Tanaka, T. Kawai, J. Appl. Phys. 80, 787 (1996).

[15] R. D. Vispute, V. Tayansky, S. Choopun, R. P. Sharma, T. Venkatesan, M. He, X. Tang, J. B. Halpern, M. G. Spencer, Y. X. Li, L.G. Salamanca-Riba, A. A. Illiadis, K. A. Jones, Appl. Phys. Lett. 73, 348 (1998).

[16] Yun Hi Lee, Man Ho Song, Byeong Kwon Ju, et al., J. Vac. Sci. Technol. B 15(2),

(1997).

[17] T. Minami, H. Nanto, S. Takata, Appl. Phys. Lett. 41 958 (1985).

[18] T. Minami, H. Nanto, S. Takata, Jpn. J. Appl. Phys. 124, 43-47 (1985).

[19] Hu, R. Gordon, J. Appl. Phys. 71 880 (1992).

[20] Kobayashi, T. Matsubara, S. Matsushima, S. Shirrakata, S. Isomura, G. Okata, Thin Solid Films, 266, 106 (1995).

[21] G. L. Mar, P. Y. Timbrell, R. N. Lamb, Chem. Mater. 7, 1890-1896 (1995).

[22] T. Tsuchiya, T. Emoto, T. Sei, J. Non-Crystal. Solids. 178, 327-332, (1994).

[23] Spanhel, Lubomir, Anderson, Marc A. J. Am. Chem. Soc. 113, 2826-2833 (1991).

[24] J. Zhai, L. Zhang, X. Yao, Ceramics International 26,883-885, (2000).

[25] Y. Natsume, H. Sakata, Thin Solid Films 372, 30-36 (2000).

[26] Y.S. Choi, C.G. Lee, S.M. Cho, Thin Solid Films 289, 153-158 (1996).

[27] J.L. van Heerden U, R. Swanepoel, Thin Solid Films 299, 72–77 (1997).

[28] S. A. Studenikin, N. Golego, M. Cocivera, J. Appl. Phys. 83, 2104 (1998).

[29] Miki-Yoshida, F. Paraguay-Delgado, W. Estrada-Lopez, E. Andrade, Thin Solid Films 376, 99-109 (2000).

[30] Y. Kamada, T. Kawaharamura, H. Nishinaka, S. Fujita, Jpn. J. Appl. Phys. 45 L857 (2006).

[31] H. Nishinaka, Y. Kamada, N. Kameyama, S. Fujita, Phys. Status Solidi (B) 247, 6, 1460-1463 (2010).

[32] C. Biswasa, Z. Ma, X. Zhu, T. Kawaharamura, K. L. Wang, Solar Energy Materials Solar Cells 157, 1048-1056 (2016).

[33] T. Kawaharamura, T. Hirao, Jpn. J. Appl. Phys. 51, 036503 (2012).

[34] T. Kawaharamura, G. T. Dang, M. Furata, Jpn. J. Appl. Phys. 51, 040207 (2012).

[35] Giang T. Dang, M. W. Allen, M. Furuta, T. Kawaharamura, Jpn. J. Appl. Phys. 58, 090606 (2019).

[36] Li Liu, T. Kawaharamura, G.T. Dang, H. Kobayashi, H. Orita, Jpn. J. Appl. Phys. 58 025502 (2017).

[37] P. Rutthongjan, L. Liu, M. Nishi, M. Sakamoto, S. Sato, G. T. Dang, T. Kawaharamura, Jpn. J. Appl. Phys. 58, 035503 (2019).

[38] T. Kawaharamura, Jpn. J. Appl. Phys. 53, 05FF08 (2014).

[39] T. Kawaharamura, H. Nishinaka, K. Kametani, Y. Masuda, M. Tanigaki, and S. Fujita, Zairyo 55, 153 (2006).

[40] T. Kawaharamura, H. Nishinaka, and S. Fujita, Zairyo 57, 481 (2008).

[41] S. Limpijumnong, W. Lambrecht., Phys. Rev. B 63, 104103 (2001).

[42] J. F. Sarver, Fred L. Katnack, F. A. Hummel, J. Electrochem. Soc. 106, 960 (1959).

[43] W.I. Park, G.C. Yi, H.M. Jang, Appl. Phys. Lett. 79, 2022 (2001).

[44] R.D. Shannon, Acta Cryst. A32, 751 (1976).

[45] Oliver R. Wulf, the Discussion of Ozone. 156, 54 (1932).

[46] N. Barsan, U. Weimar, J. Electroceram. 7 (2001) 143.

[47] Suchea, M., Christoulakis, S., Moschovis, K., Katsarakis, N., & Kiriakidis, G., Thin solid films, 515(2), 551-554 (2006).

Chapter 4

Fabrication and Characterization of Ag_xO Thin Film by Mist-CVD

Silver is widely used as an electrode because of its good conductivity and stability. Silver belongs to the transition metal group. Thus, silver oxides present the multivalent mixture oxidation states. In this chapter, serial trial experiments of grown Ag_xO films by mist-CVD were carried out. Investigations of the properties of mist-CVD Ag_xO are mainly focused on influence of supporting Ozone and H_2O.

4.1 Introduction

There are various deposition methods for Ag or Ag_xO thin films. Most of them are vacuum-based systems due in part to dense and high-quality films [1, 2]. They are widely used in the practical manufacturing process. For example, the sputtering technique is a well-developed method for large-size flat panel displays. In the next chapter, we discuss our experimental results via the RFM-sputtering system. The advantage of sputtering techniques is that, depending on the materials, the different compounds can be grown by adequate selection of the targets. Furthermore, other techniques, such as pulsed laser deposition (PLD) 3,4) and plasma- or UV-enhanced ALD 5, 6) are also used to obtain high-quality Ag_xO layers. The purpose of this study is to carry out a trial of the mist-CVD growth process to prove the potential of using such an atmospheric deposition method for the growth of the Ag and Ag_xO thin films.

4.2 Effects of Ozone and H_2O Influence on the Mist-CVD Ag_xO Thin Films

4.2.1 Experimental Methods

The mist-CVD Ag and Ag_xO films were deposited on quartz substrates via two chambers of the mist-CVD system. Ag precursor is supplied by carrier gas/dilution gas (c.g. / d.g.) = 2.0 / 3.0, and associated with the oxidant source of H_2O and O_3. Each quartz substrate was ultrasonically precleaned for 2 min, respectively, in acetone, isopropyl alcohol, and deionized (D.I.) water followed by drying in an N_2 gas gun. Details of the deposition conditions are concluded in Table 4-1.

Table 4-1 Effects of H_2O and O_3 on mist-CVD Ag_xO thin films experiment conditions

	Chamber A	Chamber B	Assistant gas
Source concentration	Ag(ac) + MeOH +AMS 20mM + 95mL + 5mL	H_2O	O_3 10 g/m^3
c.g. / d.g.	2.0 / 3.0	0.0 / 5.0 (C1)	1.5
		0.5 / 4.5 (C2)	
Growth time & Temperature	10 min or 20 min & 350 ℃		
Ultrasonic transducer	2.4 MHz, 24 V·0.625 A		

4.2.2 Results and Discussions

Fig 4.1 shows (a) the crystal structure of the GIXD spectra and (b) the appearance of Ag_xO grown by the mist-CVD system with Hall measurement results. C1 represents the standard condition that did not use H_2O or O_3 as oxidant, and C2 represents the condition of using the assistance of O_3 gas. According to the GIXD spectra, at the same position as the sputtering Ag_xO appeared the diffraction peaks, which are Ag related diffraction peaks: (111), (200), (220) and (311), and the peak of Ag_2O (111). However, by the appearance observation of Fig. 4.2 (b) during the standard condition C1, the appearance shows brownish from the basement of the substrate and silvery

color from the top surface. This indicates that during growth processing, at high temperature (T = 350℃), the Ag_xO on the top side was partially reduced and some decomposition to silver metal on the top surface. This can be proved by the comparison between the top surface (on the right side of Fig. 4.1 (b)) and the back side surface (on the right side of Fig. 4.1 (b)), there are obvious differences in the color appearances.

From the results of the hall effect as shown in Fig. 4.1 (b), the resistivity of C1 sample is 9.1×10^{-1} Ω·cm, mobility (μ) = 2.5 $cm^2/V{\cdot}s$, carrier concentration (N) = -4.1×10^{23} cm^{-3}. Furthermore, since the sample was grown under the condition of C2 the oxidant was O_2 plus O_3, so the produced films would be completely oxidized due to the stronger oxidizing potential of O_3. As we can see from the appearance, the color shows only a brownish-red color, and the resistivity was increased to 2.3×10^8 Ω·cm. This means that the Ag Mist droplets were thoroughly oxidized and resulted in semiconductors or insulators. Reference to previous studies has shown that exposure to ozone largely facilitates the oxidation of Ag through the reactions as below:

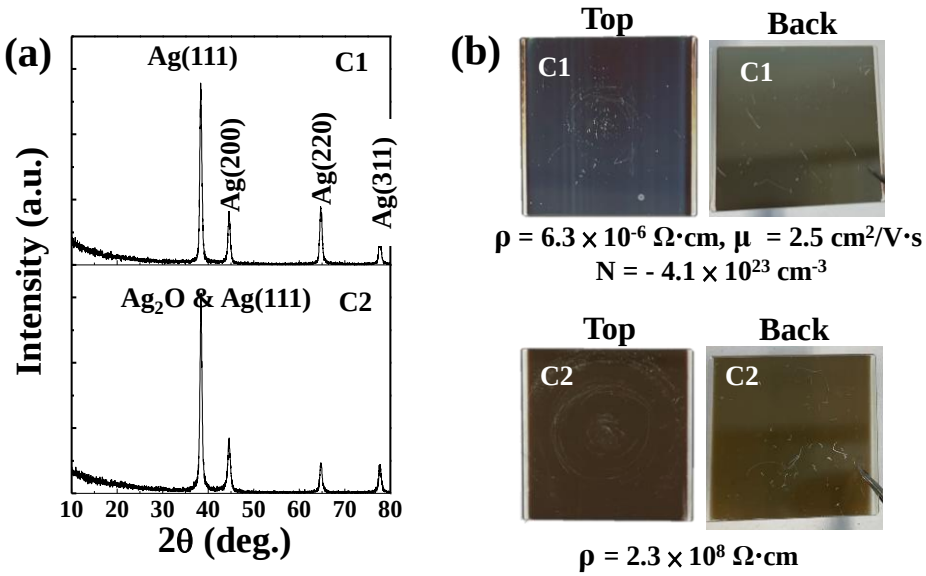

Fig. 4.1. (a) GIXD spectra and (b) appearance of mist-CVD Ag_xO

$$2Ag(s) + O_3(g) \rightarrow Ag_2O(s) + O_2(g) \quad (1)$$

$$Ag_2O(s) + O_3(g) \rightarrow Ag^{I}Ag^{II}O(s) + O_2(g) \quad (2)$$

Otherwise, oxidation of Ag would not readily take place under ambient conditions at room temperature.

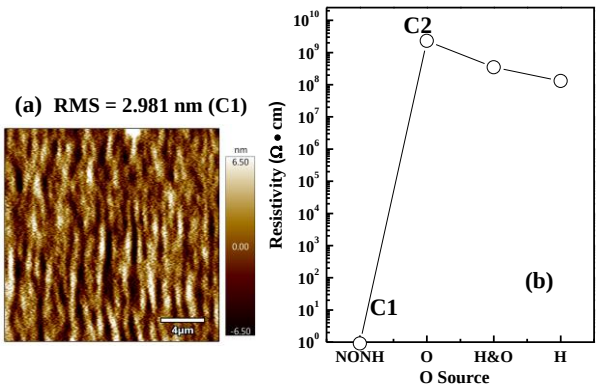

Fig. 4.2. (a) AFM image and (b) Resistivity of mist-CVD Ag_xO

Fig 4.2 shows (a) the AFM image of the sample under the condition of C1, which is without H_2O and O_3, the RMS value is around 3 nm. This suggests that using mist-CVD grown Ag_xO can yield high-quality thin films. Fig. 4.3 (b) is the resistivity of all samples. When the sample was grown without O_3 and H_2O, the resistivity was 9.1×10^{-1} Ω·cm, and when the sample was grown with O_3, the resistivity increased to 2.3×10^{8} Ω·cm, but when the sample was grown both H_2O and O_3, the resistivity decreased slightly.

Comparison of Ag_xO surface images before and after introducing O_3 is shown in

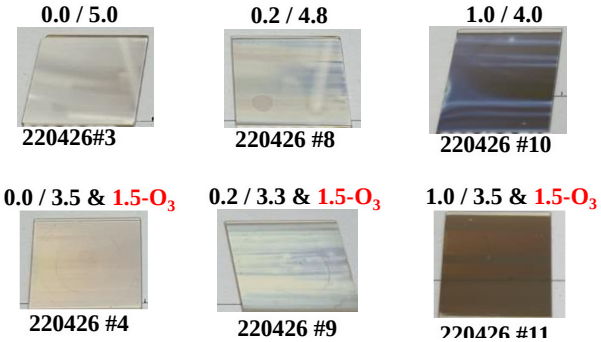

Fig. 4.3. Ag_xO surface images comparison before and after introducing O_3

Fig. 4.3. After introducing O_3, the film becomes more uniform and transparent.

Table 4-2 Ag_xO resistivity

Oxidant	H_2O (0.0/5.0)	H_2O (1.0/4.0)
Resistivity	5	5.4×10^{9}
Oxidant	H_2O (0.0/5.0) + O_3	H_2O (1.0/4.0) + O_3
Resistivity	4×10^{9}	2.3×10^{10}

The resistivity of Ag_xO before and after introducing O_3 is summarized in Table 4-4. When there was no oxidant (H_2O c.g. / d.g. = 0.0 / 5.0), the sample had metal behavior with the resistivity around 5 Ω·cm.

Changes before and after introducing O_3 were investigated using GIXD measurement and transmittance as evaluation methods. GIXD spectra are shown in Figure 4.4. There is no obvious change before and after introducing O_3, and the peak derived only from Ag, that is, Ag (111), Ag (200), Ag (220), and Ag (311) appeared, and no peak derived from AgO_x was detected. However, the intensities of the Ag-related peaks decreased after introducing O_3 as H_2O c.g. / d.g. = 1.0 / 4.0.

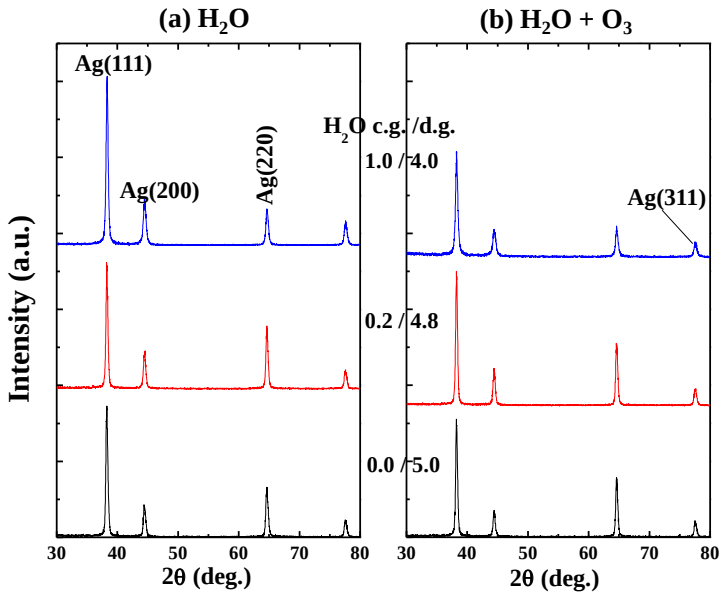

Fig. 4.4. GIXD spectrum (a) H_2O oxidant (b) H_2O + O_3 oxidant

In addition, it can be seen that the transmittance in Fig. 4.5 shows a significant change before and after introducing O_3 referring to the long wavelength range. The reason for this is thought that the reactive O_3 radicals enhanced the interaction between the precursors and led to more Ag incorporated with active oxygen particles resulting in the mixture of Ag and Ag_xO. However, from the GIXD spectra, there were indeed no Ag_xO peaks detected during the GIXD measurement. These inconsistent results may come from the different areas measured in the samples.

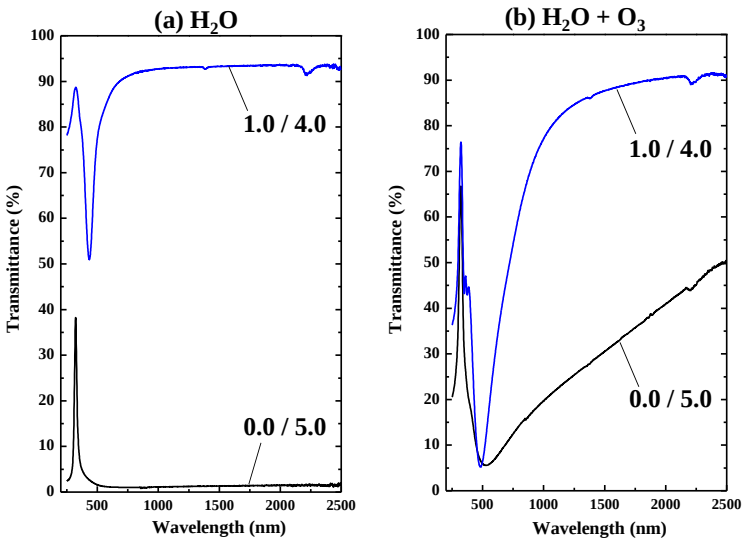

Fig. 4.5. UV-vis transmittance of Ag_xO (a) H_2O (b) $H_2O + O_3$

4.3 Conclusions

We found that Ag deposition should be acted with caution during the process phase such as the influence of oxidation. And H_2O and O_3 can be used for Ag_xO deposition to control the extent of oxidization. Two chambers are necessary for Ag_xO deposition. The preparation of Ag and Ag_xO thin films via mist-CVD system, temperature at 400 ℃ and 350 ℃ reaction is performed.

4.4 References

[1] Park, J. S., Maeng, W. J., Kim, H. S., Park, J. S.:Review of recent developments in amorphous oxide semiconductor thin film transistor devices. Thin Solid Films 520(6), 1679-1693 (2012).

[2] Fortunato, E., Barquinha, P., Matins, R., Oxide semiconductor thin film transistors: a review of recent advances. Adv. Mater. (Deerfield Beach, FL) 24(22), 2945-2986 (2012).

[3] Suresh, A., Wellenius, P., Dhawan, A., Muth, J.: Room temperature pulsed laser deposited indium gallium zinc oxide channel based transparent thin film transis-

tors. Appl. Phys. Lett. 90(12), 123512 (2007).

[4] Gupa, M., Chowdhury, F.R., Barlage, D., Tsui, Y.Y.: Optimization of pulsed deposited ZnO thin film growth parameters for thin film transistors (TFT) application. Appl. Phys. A 110(4), 793-798(2013).

[5] Lee, B. H., Cho, S., Hwang, J. K., Kim, S. H., Sung, M. M.: UV-enhanced atomic layer deposition of ZrO_2 thin films at room temperature. Thin Solid Films 518(22), 6432-6436 (2010).

[6] Lim, S.J., Kim, J.-M., Kim, D., Lee, C., Park, J.-S., Kim, H.: The effects of UV exposure on plasma-enhanced atomic layer deposition ZnO thin film transistor. Electro. chem. Solid-State Lett. 13(5), H151 (2010).

Chapter 5

The Effects of Oxygen Flow Ratio on the Properties of Ag_xO Thin Films Grown by Radio Frequency Magnetron-Sputtering

RFM-sputtering Ag_xO was applied on the ZnMgO/Ag_xO HJDs fabrication. The properties of Ag_xO thin films are crucial for the performance of ZnMgO/Ag_xO HJDs. In this chapter, we mainly investigated the influence of the oxygen flow ratio on the properties of Ag_xO thin films grown by radio frequency magnetron-sputtering.

5.1 Introduction

Oxide-based thin film properties are highly beneficial in a variety of technological applications, including transparent conductive films, gas sensors, LEDs, transparent electronic devices, and solar cells, among others. Thus, to obtain the adjustable properties of semiconductor materials, precise control of extent of oxidation of the thin film during the synthesis process is important for the electronic industry [1, 2, 3].

According to previous investigations, silver oxide (Ag_xO) is a transparent material at wavelengths ranging from the infrared region to the visible region with an optical band gap in the range of 1.2 ~ 3.1 eV. While, silver (Ag) is a good reflective coating for applications in the opt-electrical field [4]. Ag_xO is preferable for use in battery electrodes as it performs better in voltage regulation and enhances storage life [5, 6]. The work function can reach roughly 5.3 eV with O_2 plasma treatment or UV-ozone treatment of Ag anodes [7, 8]. Especially, Ag_2O films in general are reported to show p-type semiconducting properties [9, 10, 11]. However, previous studies [7, 13] have revealed the instability of Ag_xO resulting from heating in the transition of composition, crystal-

linity, refractive index, and other properties. Furthermore, silver oxides (AgO, Ag_2O) desorb oxygen at low temperatures (~200 °C)[13]. As a consequence, a low-temperature film fabrication process is required to form Ag_xO thin films.

Sophisticated growth methods for Ag or Ag_xO thin film deposition are well developed, including chemical bath deposition (CBD) [10], dry chemical route at room temperature [11], electron beam (EB) evaporation [12, 13], microwave sputtering [14], and DC magnetron sputtering [15~17]. Furthermore, partially oxidized Ag_xO films grown by reactive sputtering were applied for the fabrication of Ag_xO/ZnO Schottky diodes (SBDs) [18], Ag_xO/α-Ga_2O_3 metal semiconductor field effect transistor (MESFET) [19], Ag_xO/IGZO SBDs [20], and Ag_xO/ZnMgO heterojunction diodes (HJDs) [21]. The applications of Ag_xO thin films have been proven to improve the barrier height. Indeed, reactive oxygen might have the capacity to provide O-rich ambient healing of the interface defects or states, as a result of the Ag ion/plasma would combining with reactive oxygen (oxygen plasma, oxygen radicals) during the sputtering deposition process. Therefore, the purpose of this work is to investigate the effect of different oxygen flow ratios of R[O_2] % = [O_2 / (O_2 + Ar)] % on the properties of the Ag_xO film properties grown by the radio frequency magnetron sputtering (RFM-SPT) deposition method.

5.2 Experimental Methods

Ag and Ag_xO films were deposited at room temperature (25 °C) on quartz substrates that were placed vertically above the Ag target at an appropriate distance by introducing the excited gas mixture of Ar without/with O_2 via a radio frequency magnetron sputtering (RFM-SPT) deposition system. Before film deposition, the reaction chamber was evacuated to a base pressure below 1×10^{-4} Pa. During film deposition, the working pressure was maintained at 0.3 Pa. The total flow rate ([O_2 + Ar]) was set at 10 sccm, and the oxygen flow ratio (R[O_2] % = [O_2 / (O_2 + Ar)] %) was changed from 0 % to 30 %, while the power supply was fixed at 40 W. Each quartz

substrate was ultrasonically precleaned for 2 min in acetone, isopropyl alcohol, and deionized (D.I.) water, respectively, and was then dried using an N_2 gas gun. Before the growth rate was checked, the pretest sample preparation was operated to maintain the chamber ambient and also to remove the top oxidized layer of the Ag target, after which the thin film with the target thickness was prepared accordingly. The details of the deposition conditions are summarized in Table 5-1.

Table 5-1 RFM-SPT deposition conditions for Ag_xO films

Target	R[O_2] (%)	Pressure (Pa)	Power (W)	Thickness (nm)	Growth time (min)
Ag	0 ~ 30	~ 0.3	40	50	≅ 5
				150	≅ 20

The crystal structure was analyzed by grazing incident X-ray diffraction (GIXD) spectra using CuKα radiation (Rigaku Corp., Smart Lab, X-ray wavelength λ = 1.5418 Å, incident angle 0.35°). The surface morphology was characterized by scanning electron microscopy (SEM) (Hitachi SU8020). The optical transmittance of the Ag and Ag_xO films was measured in the range from 200 nm to 2500 nm using a UV-visible spectrometer (Hitachi UV-vis U-4100). Afterward, the band gaps were calculated and confirmed by the Tauc plot. The Tauc plot was built on the data extracted from the transformation of transmittance spectra into absorption spectra. Resistance was measured by the resistive measurement system (MITSUBISHI Chemical Corp., Hiresta-Up MCP-HT450). The work function of 150 nm thick Ag and Ag_xO films on the quartz substrate was determined by photoelectron yield spectroscopy (PYS) (BUNKOUKEIKI Corp., BIP-KV202GD/UVT) in vacuum at room temperature. X-ray photoelectron spectroscopy (XPS) (Ulvac-Phi ESCA 5500 A) was used to investigate the chemical states of the Ag and Ag_xO films, and a monochromic Al Kα (1486.6 eV) X-ray source was operated at 96 W and 12 kV at room temperature below 3.0×10^{-8} Pa. The binding energies in the XPS spectra were calibrated by the peak position of the C 1s spectra appearing at 284.8 eV for adventitious carbon surface contamination [22–24].

5.3 Results and Discussions

Under vacuum ambient, Ag_xO films were deposited on quartz in various oxygen flow ratios (R[O_2] %). Photos showing the appearance of Ag_xO of the thickness of (a) 150 nm and (b) 50 nm, which had long exposure to the atmosphere and was placed on top of the illuminated screen, are shown in Fig. 5.1. At the same light illumination, the Ag_xO samples present different transparency colors, for an increase of R[O_2] %. The color-changing tendency is the same for 150 nm and 50 nm films. More remarkable changes could be seen in (a) 150 nm; As the Ag_xO film with R[O_2] % = 0 % presented silvery metallic color and 10 % showed dark brown color that blocked light to pass through, but after increasing R[O_2] % from 16 % to 30 %, all Ag_xO films showed lighter brown-gray colors with the exception of R[O_2] % = 17 % which presented yellow color. It can be seen that the appearance changes significantly in relation to the oxygen flow ratio (the change in the x value), and the trend of the color change follows in 4 categories of the oxygen flow ratio: 0%, 10%, below 17%, and above 17%.

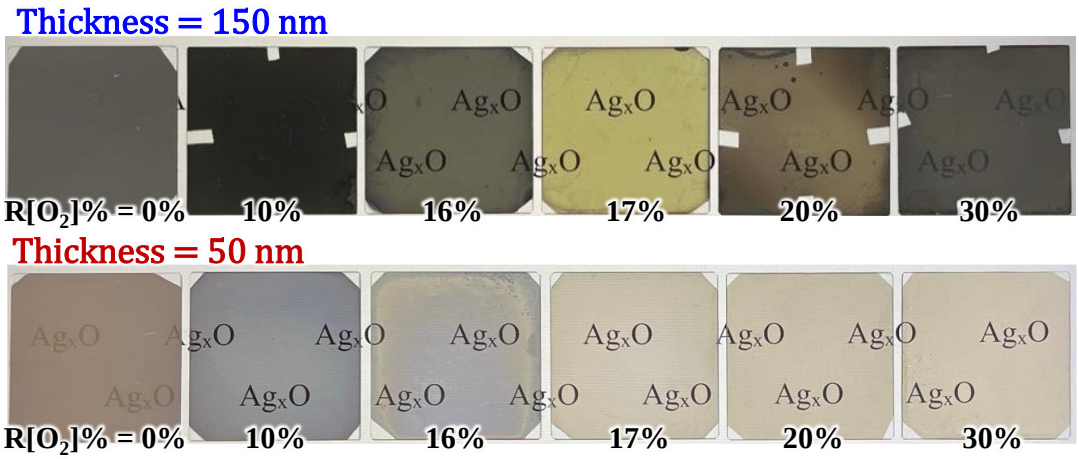

Fig. 5.1 Ag_xO samples appearance photos comparison with various R[O_2] % (a) thickness is 150 nm (b) thickness is 50 nm.

The influences of R[O_2] % on crystal structure were investigated using GIXD spectra with thicknesses of (a) 150 nm and (b) 50 nm, as shown in Fig. 5.2. Focusing on samples of R[O_2] % = 0 %, Ag-related diffraction peaks are detected as: (111), (200), (220), and (311), respectively, in samples with thicknesses of 150 nm and 50 nm. The relative intensity of the Ag (111) diffraction peak is significantly higher than

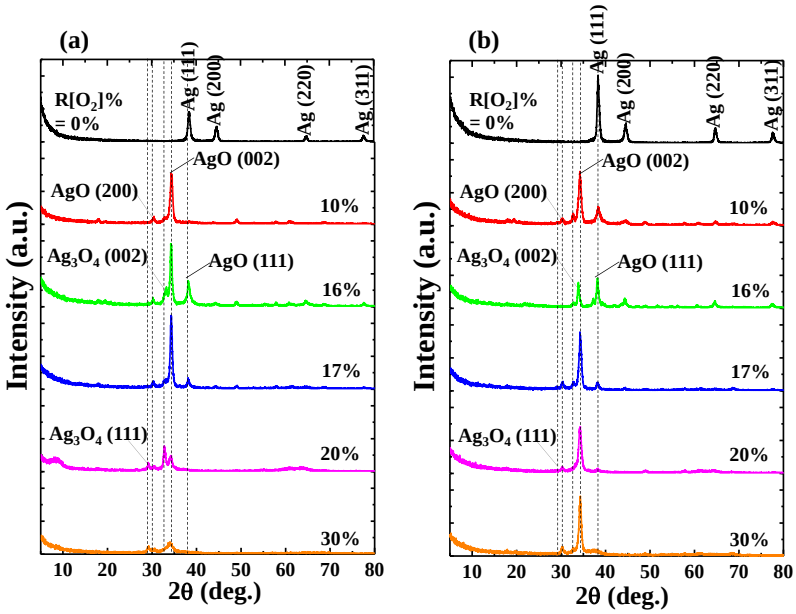

Fig. 5.2. Influence of R[O_2] % on GIXD of Ag_xO films
(a) 150 nm (b) 50 nm

others. After oxygen was introduced into the depositions, all of the diffraction peaks of Ag were diminished. Ag cations started to bond with oxygen ions, forming transparent Ag_xO films. For low oxygen flow ratios of R[O_2] % = 10 % to 17 %, the dominant diffraction peak at 2θ = 34.52° was confirmed as the representation of the AgO (002) peak [25, 26], and its intensity is properly proportional to the increase in R[O_2] %. However, when R[O_2] % exceeded 20 %, the intensities of AgO (002) were clearly reduced. On the other hand, the other two related AgO peaks of (200) and (111) were detected at 2θ = 30.2° and 38.3° from these measured samples. AgO (200) had a relatively weak signal with constant intensity, and AgO (111) only appeared as R[O_2] % = 16 % and 17 % with decreased intensity. No Ag_2O peaks were detected in these depositions [27, 28, 29]. At the same time, another small shoulder shaped diffraction peak adja-

cent to the AgO (002) diffraction peak without regular tendency of intensities of increase of R[O_2] % was determined as the Ag_3O_4 (002) diffraction peak [30, 31]. After the R[O_2] % increased to 20 % and 30 %, another related to the Ag_3O_4 diffraction peak (111) was presented at 2θ = 29° with a weak constant intensity. Other studies [32 ~ 34] have reported that the dissociation of Ag_3O_4 ($2Ag_3O_{4(s)} \rightarrow 6AgO_{(s)} + O_{2(g)}$) readily happen even at room temperature, as the crystal grains of Ag_3O_4 randomly distributed between the $Ag^{(II)}O$ and $Ag_2{}^{(III)}O_3$. Therefore, at high R[O_2] %, the Ag_xO grains are considered as a mixture of two or more individual oxides of $Ag^{(II)}O$ and $Ag_2{}^{(III)}O_3$ [26, 35, 36, 37].

Furthermore, comparing samples with different thicknesses prepared at the same R[O_2] %, it was found that confirmed diffraction peaks appeared in the same 2θ position with slightly different intensities, but the Ag_3O_4 (111) peak is not mainly presented in the 50 nm sample, and the AgO (002) peak appeared as the dominant peak at any oxygen flow ratios.

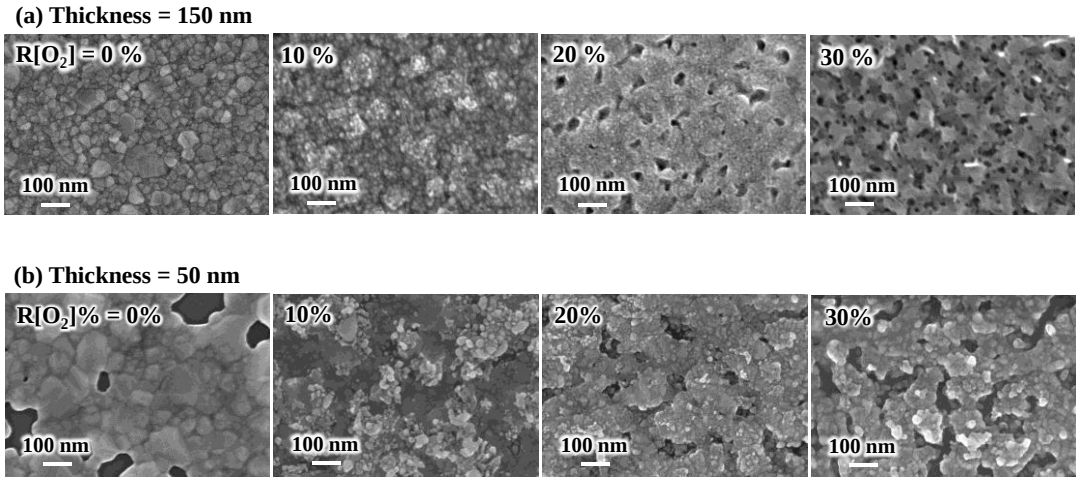

Fig. 5.3 Influence of R[O_2] % on the surface morphology of Ag_xO films
(a) 150 nm (b) 50 nm

The surface morphology images of Ag_xO (a) 150 nm and (b) 50 nm are shown in Fig. 5.3. Without oxygen, the Ag films of both the 150 nm and 50 nm thickness samples showed good smooth top surfaces. After introducing oxygen, the grain shape presented a spherical grain morphology and the grain size clearly became smaller, and

the white color particles were characterized by a spherical grain morphology on top of the surface. In addition, we can see that Ag_xO films become much looser and more polyporous with an increase of R[O_2] % from 20 % to 30 %, indicating that the surface relocation of silver atoms had increased and the 3-dimensional crystal growth formed at high oxygen flow ratios.

The variations in transmittance with the wavelength of different R[O_2] % of 150 nm Ag_xO films are shown in Fig. 5.4 (a). It can be seen that the transmittances between the R[O_2] % of 10 % and 16 % clearly increased in the longer wavelengths. The absorption edges were narrowly blue-shifted between R[O_2] % of 10 % ~ 17 %, but after R[O_2] % increased to 20 % and 30 % the transmittances were decent and the absorption edges were red-shifted in a certain range. The relation between the optical absorption coefficient α of a direct band gap (E_G) semiconductor near the band edge and the photon energy hv is given by the following equation [38, 39]:

$$\alpha hv = A(hv - E_G)^{1/2},$$

where A is a constant value. The film transmittance (T) around the absorption edge is approximated as $\exp(-\alpha t)$, where t is the film thickness. By then plotting $(\alpha hv)^2$ versus photon energy hv, the band gap E_G can be confirmed by linear extrapolations of the absorption region. Furthermore, referring to the data from the GIXD results, we

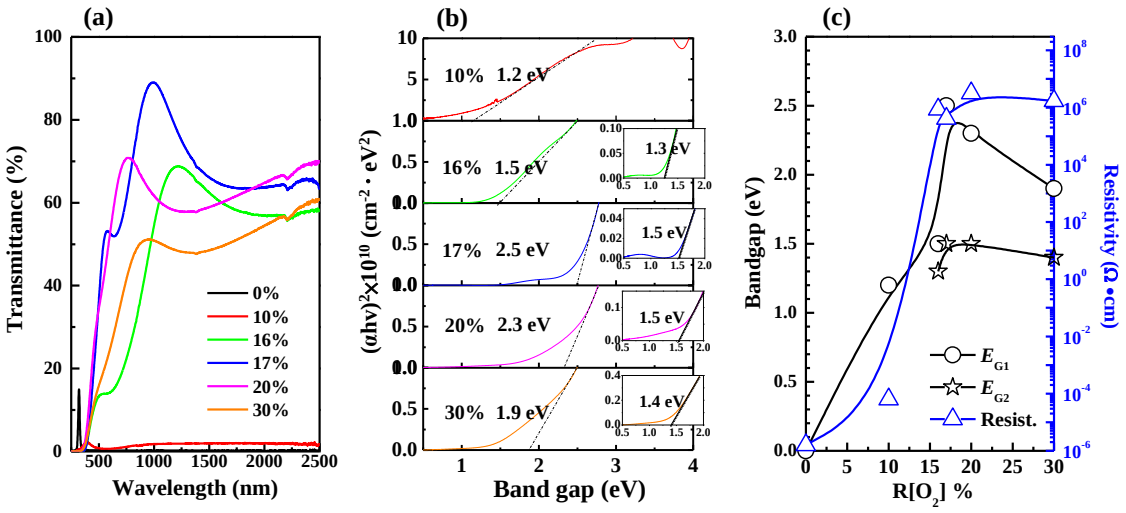

Fig. 5.4. Variations in (a) transmittance (b) band gaps were extracted from the linear extrapolations of thickness 150 nm samples

found that 150 nm samples had mixture crystals present under certain conditions. Fig. 5.4 (b) shows the band gap evaluation of 150 nm thickness Ag_xO samples. The optical band gaps (E_{G1}) increased from 1.2 to 2.5 eV as the R[O_2] % increased from 10 % to 17 %. After the R[O_2] % increased to 20 % and 30 %, the band gap decreased. Meanwhile, the observation from Fig. 5.4 (b) of the absorption edges curve along with different trends indicates that the Ag_xO grains were a mixture of two individual oxides. When magnifying into the smaller range of the absorption region, as shown in the inset of Fig. 5.4 (b), the other band gaps (E_{G2}) value could be confirmed. And in Fig. 5.4 (c), the resistivity (ρ) was also evaluated, which had a similar changing tendency to that of the band gaps confirmed variations with increasing oxygen flow ratios, that is, as R[O_2] % = 10 % ~ 16 %, ρ increased from 6.3 $\times 10^{-5}$ $\Omega \cdot$ cm to 8.6 $\times 10^{5}$ $\Omega \cdot$ cm, and as R[O_2] % = 17 % ~ 30 %, ρ slightly decreased but almost stabilized as 10^{6} $\Omega \cdot$ cm. Although the thickness of the films affected the optical evaluation, we decided to evaluate thinner samples with a thickness of 50 nm again.

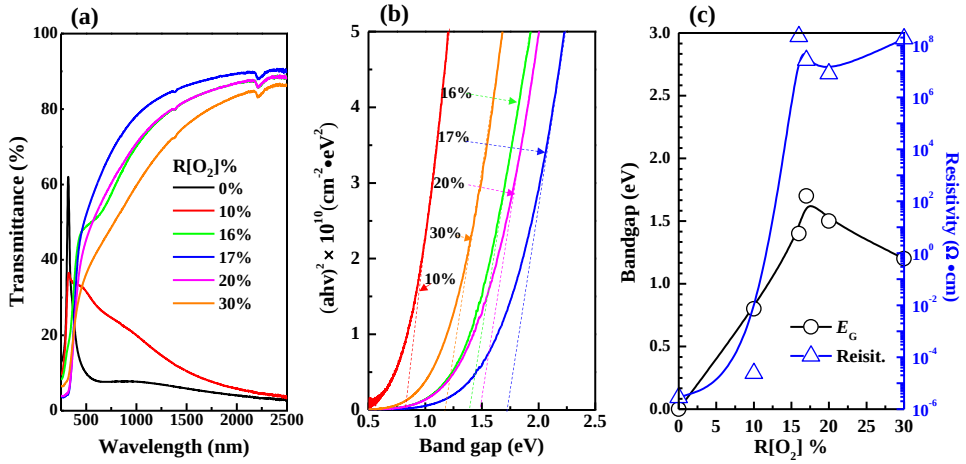

Fig. 5.5. Variations in (a) transmittance (b) band gaps were extracted from the linear extrapolations of thickness 50 nm samples

Fig. 5.5 shows the optical properties of 50 nm Ag_xO films, which were shown to be more transparent from the observation of Fig. 5.1. Therefore, they had higher transmittance with a comparison of 150 nm samples at the same R[O_2] % as shown in Fig. 5.5 (a). The band gaps of 50 nm samples could be precisely confirmed, because its crystal structure tends to be dominated only by the AgO (002) peak and widened from

0.8 to 1.7 eV with the increase in R[O_2] % from 10 % to 17 %. Meanwhile, from Fig. 5.4 (c) and Fig. 5.5 (c), it is observed that the resistivity (ρ) reached the summit value as R[O_2] % = 20 % of 150 nm Ag_xO films: $\rho = 3.2 \times 10^6\ \Omega \cdot \mathrm{cm}$, and as R[$O_2$] % = 16 % of 50 nm Ag_xO films: $\rho = 2.2 \times 10^8\ \Omega \cdot \mathrm{cm}$. The resistivity of 50 nm samples is 2 magnitudes higher than that of 150 nm samples. The band gap reached the summit value as R[O_2] % = 17 % of 150 nm Ag_xO films: $E_G = 2.5$ eV and 1.5 eV, and as R[O_2] % = 17 % of 50 nm Ag_xO films: $E_G = 1.7$ eV. These results could be interpreted as that after R[O_2] % exceeded 17 % provided O ions sufficiency ambient with the result of the higher chemical formation of Ag cations.

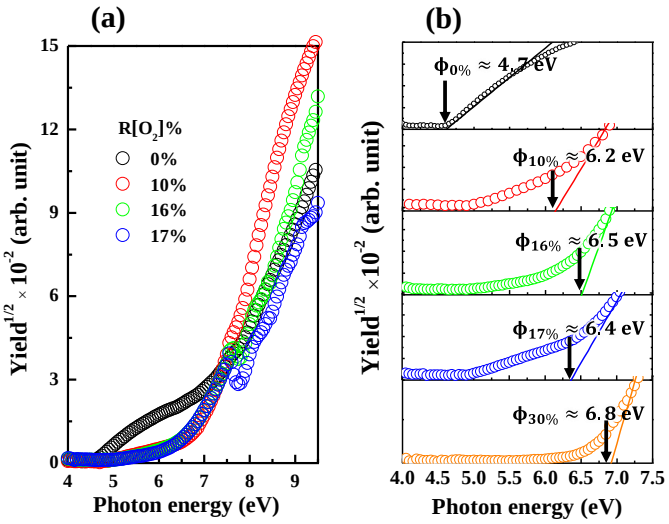

Fig. 5.6 PYS spectra of Ag_xO films with various R[O_2] % (a) full range (b) magnification of small range

Afterwards, all measurements and analyzes were based on the 150 nm thickness Ag_xO sample. Variations in the PYS spectra of the Ag_xO films depending on the R[O_2] % are presented in Figure 5.6 with (a) the full scan range and (b) a small magnification range to determine the work function of Ag and the ionization energy of Ag_xO. The monochromatized photon from D_2 (30 W) lamp is used as the excitation light. The density of yield photoelectrons (Y) of Ag_xO samples is detected by irradiated D_2 light with incremental photon energy (hv) scan from 4 eV to 9.5 eV, which is thought to be proportional to the square root in the surface area of hv over the thresh-

old ionization energy (I_{th}) which is equal to the energy difference $E_0 - E_{\mathrm{F}}$ for Ag, or $E_0 - E_{\mathrm{v}}$ for Ag_xO, where E_0 is vacuum level, E_{F} is fermi level, E_{v} is valence band energy. I_{th} was evaluated by the following equation $Y \propto (h\nu - I_{\mathrm{th}})^{1/2}$ [40, 41] with plotting the $h\nu$ versus $Y^{1/2}$ spectra then by linear extrapolations of $Y^{1/2}$.

In a certain range of increasing R[O_2] %, the ionization energy of Ag_xO tended to be high energy shifting of the spectra approaching R[O_2] % = 10 % obtained approximately 6.2 eV, and by increasing R[O_2] % to 16 %, it shifted to 6.5 eV. However, when R[O_2] % is 17 %, the yield of photoelectrons did not increase monotonically with increasing $h\nu$ and the ionization energy appears to shift in the opposite direction reaching to 6.4 eV. This may be attributed to the highest resistivity of the 17 % Ag_xO sample with mere electrons so that the 0.1 second waiting time yielded a lower density of photoelectron. And the R[O_2] % = 16 % sample might have similar abnormal data. And after R[O_2] % increased to 30 %, its ionization energy continued to shift high energy at 6.8 eV, but there was no abnormal behavior of the photoelectron yield as R[O_2] % = 30 %.

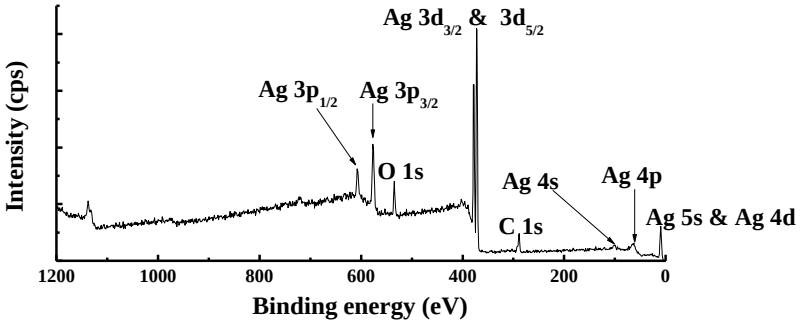

Fig. 5.7. XPS survey spectrum obtained from the R[O_2] % = 17 % Ag_xO sample.

The XPS survey spectrum obtained from R[O_2] % = 17 % of the Ag_xO film is shown in Fig. 5.7. The major elements and the minor elements represent peaks in this survey spectrum including the Ag 2p, Ag $3d_{3/2}$, Ag $3d_{5/2}$, Ag 4s, and Ag 4p peaks, the O 1s peak and the C 1s peak, and the Ag 5s & Ag 4d peak. The specific information of the C 1s, Ag $3d_{5/2}$ and O 1s spectra about the peak assignments and chemical species correspond to different Ag-O compounds with the comparison of the increment of

R[O_2] % from 0 % to 30 % obtained by examining the high-resolution XPS spectra shown in Fig. 5.8 (a), (b) and (c), respectively.

The binding energies are calibrated to the C 1s peak at 284.8 eV using charging correction and XPS analyzer techniques. Subsequently, the Ag $3d_{5/2}$, O 1s, and C 1s spectra were fitted with Gaussian curves. Referring to several previous published XPS studies for Ag_xO [42~47], the binding energies of C 1s, Ag $3d_{5/2}$ and O 1s photoelectrons associated with different silver compounds and their chemical shift values of various R[O_2] % are given in Table 5-2 and Table 5-3.

Table 5-2 Binding energies and chemical species of C 1s spectra

Peak assignment	C 1s
C-metal	282.2
C	284.8
Carbonate	288.4

Table 5-3 Binding energies and chemical shifts for different Ag_xO compounds

Peak assignment	Ag $3d_{5/2}$	O 1s
Ag_3O_4	366.2	528.5
Ag_3O_4	367.5	530.2
AgO	367.7	530.5
Ag	368.4	530.5
AgOH	369.3	532

The C 1s spectra of Ag_xO films with various R[O_2] % are shown in Fig. 5.8 (a). There are two distinct peaks shown in these spectra of the assignments at 284.8 eV due to adsorbed hydrocarbons and at 288.4 ± 0.02 eV attributed to surface carbonate [48, 49, 50]. With increments of the R[O_2] % from 0 % to 30 %, the peak positions were shifted by 1 eV towards the high energy direction from 287.4 eV to 288.4 eV, in the peaks of the surface carbonate, their intensities also increased with increasing R[O_2] %. From the GIXD data, we determined that with increases of R[O_2] %, the dominant compositions of Ag_xO were presumably changed from Ag^{2+} to the mixture of randomly distributed Ag^{2+} and Ag^{3+}. This may be caused by the surface Ag^{3+}-adhered carbonate having a higher binding energy than the surface Ag^{2+}-adhered carbonate. However, for the increase until R[O_2] % = 30 %, the extraordinary peak ap-

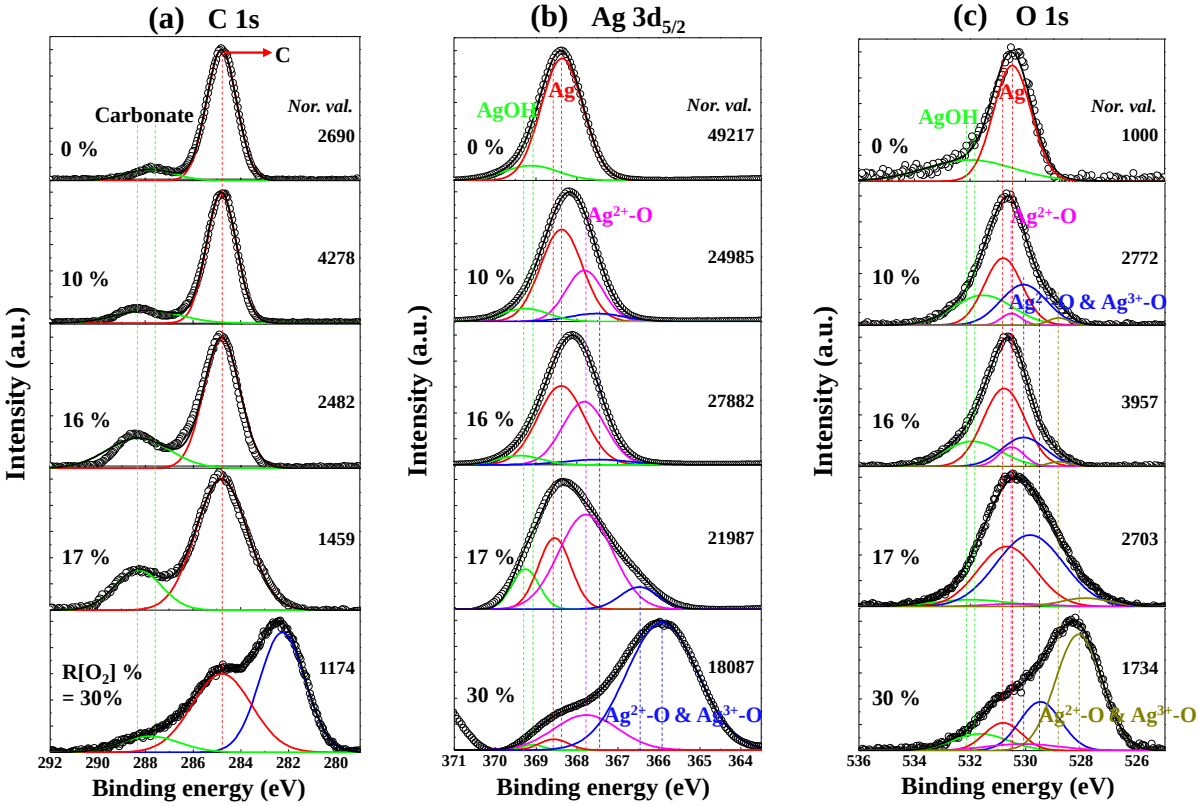

Fig. 5.8. Measured HXPS data for (a) C 1s (b) Ag 3d5/2 (c) O 1s spectra.

pears as the third peak at 282.2 eV with significant intensity, which can be expected to be C-Ag bonds from previous studies [51, 52].

The Ag $3d_{5/2}$ and O 1s spectra of Ag_xO with various R[O_2] % are shown in Fig. 5.8 (b) and (c). While R[O_2] % = 0 %, the binding energies of the Ag thin film can be observed at 368.4 eV of the Ag peak in Ag $3d_{5/2}$ and at 530.5 ± 0.02 eV of the Ag_xO-related peak in the O 1s spectra. It is postulated that the Ag_xO-related peak obtained from the Ag metal sample may be caused by the influence of the oxidized layer on the surface during atmospheric exposure. As evidence, the intensity of the O 1s peaks of the metallic Ag thin film is less than that of the corresponding peaks in Ag $3d_{5/2}$. And there are small peaks present on the higher binding energy side of both Ag $3d_{5/2}$ and O 1s spectra, corresponding to 368.9 eV and 532 eV, respectively. This may indicate the presence of hydroxy groups of AgOH, which are likely formed by H_2O absorption during exposure to air. However, AgOH is not stable above 228 K [46], so it may be

impossible for AgOH to exist in this case but here we only focus on the surface area. Meanwhile, as R[O_2] % increased to 10 % and 16 %, in the Ag $3d_{5/2}$ spectra of Ag peaks intensities were reduced and proportional increases of Ag_xO compound peaks appeared in comparison to R[O_2] % = 0 %. The binding energies of Ag $3d_{5/2}$ and O 1s were shifted to the lower binding energies within the increase in the oxidation state of Ag. Furthermore, we found that by intentionally increasing the R[O_2] % from 16 % to 17 %, even increasing the R[O_2] % by just one percent, the splitting peaks of the Ag_xO compound shifted further to the lower binding energies. From the observation of the Ag $3d_{5/2}$ spectrum of R[O_2] % = 17 % deposition, AgO dominates the fitting fragments of the Ag oxidation state. Whereas in the increase of R[O_2] % = 30 %, the assignment of the peaks occurred further transitions toward lower binding energies at 366.2 eV of Ag $3d_{5/2}$ spectrum and 528.5 eV of O 1s spectrum, and incorporation of more higher oxidation states formed as the mixture of AgO and Ag_2O_3. This suggests that at the higher oxygen flow ratio, the oxidation states of Ag are increased with the incorporation of more electrons into the chemical bond [53] to form the dominant oxidation state of Ag_3O_4, which is the mixture of two or more individual oxides of $Ag^{(II)}O$ and $Ag_2^{(III)}O_3$.

The high resolution in the -1~10 eV scan of the valence band (VB) spectra obtained by XPS measurement of Ag_xO films with various R[O_2] % is shown in Fig. 5.9 (a). The R[O_2] % = 0 % VB spectrum presents two peaks at the binding energy of 7.2 eV and 5.5 eV, which may be the result of the Ag 5s and 4d orbital atoms exerting repel forces on each other. This is consistent with the metal-metal interactions for the electric dipole transitions from 5s to 4d orbitals [54, 55]. Increasing the oxygen flow ratio of R[O_2] % from 10 % to 17 % and 30 %, only one peak can be observed with the binding energy changing from 5.8 eV to 4 eV. In the case of R[O_2] % = 17 % and 30 %, the peak wing on the lower binding energy side was lifted to a higher intensity compared to R[O_2] % = 10 % and 16 %. This may indicate that with increasing R[O_2] %, the atomic interaction preference for metal (Ag) and metal (Ag) transition to metal

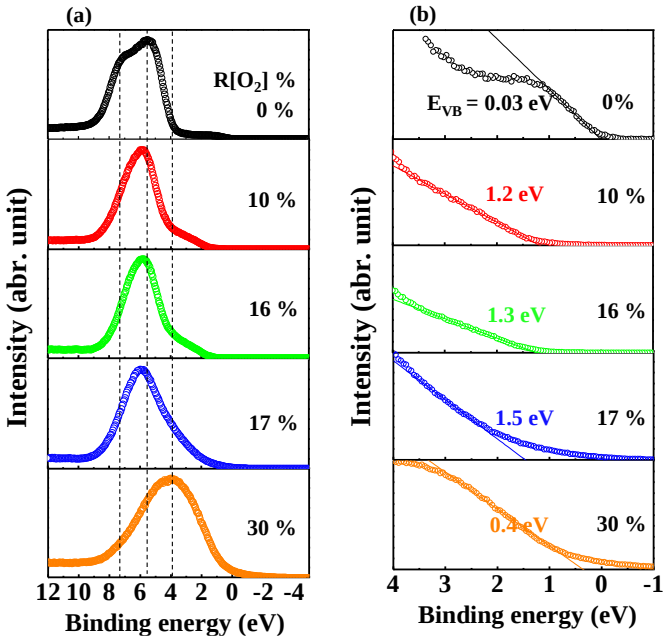

Fig. 5.9. Measured XPS data for (a) the peaks of the valence band region and (b) Magnifying the valence band region

(Ag) and nonmetal (O) [8] is interpreted as the attractive forces between the charge of the Ag 4d orbital and the charge of the O 2p orbital bonding to form a hybrid orbital around the valence band [12, 53]. The feature of the lower binding energy shift would be to the extent of hybridization of Ag 5s and/or 4p orbital with O 2p orbital [56, 57, 58]. Meanwhile, Fig. 5.9 (b) of magnifying the valence-band region provides good evidence for the interaction of the metal (Ag) and nonmetal (O) bonding system. As R[O_2] % = 0 %, the density of states at the Fermi level can be properly observed. This is in agreement with the metallic behavior characterized as pure Ag. After supplying oxygen R[O_2] %, we can observe that the oxygen-induced band is forming. In addition to that, these results closely match the ionization energy or work function data from PYS measurements, which shows that high oxygen flow ratios tend to incorporate more oxygen into the deposited film, especially the top surface range. Up to now, we can summarize all the information together to define the main species of Ag_xO films; that is, the Ag_xO samples grown under R[O_2] % = 17 % and 30 % are the mixture of $Ag^{(II)}O$ and $Ag_2^{(III)}O_3$ randomly distributed as Ag_3O_4, while those grown under

R[O_2] % = 10 % and 16 % are mainly $Ag^{(II)}O$.

Lastly, combining all the causation and correlation, we established a pilot energy level diagram of Ag_xO films with various R[O_2] % to illustrate the mechanism between the material character and R[O_2] % as shown in Fig. 5.10. Band gaps were evaluated from 50 nm Ag_xO. For R[O_2] % = 0 %, the metallic Ag film was deposited with a conductivity of 10^6 S · cm^{-1}, a work function of 4.7 eV, and the valence band and the conduction band overlapped at 0 eV (measured data showed -0.03 eV and we thought this is due to air exposure) with respect to the Fermi level. For R[O_2] % = 10 %, the semiconductor and/or insulator of AgO was deposited with the resistivity of 6.3 × 10^{-5} Ω · cm, the work function (ϕ) of 6.2 eV, and the band gap (E_G) of 0.8 eV (estimated value), in which the bottom of the conduction band is located at -0.4 eV and the top of the valence band is located at -1.2 eV with respect to the Fermi level. However, from the transmittance results, the characteristics of R[O_2] % = 10 % in the transparent region are different from those of other samples, and the reflection, not the

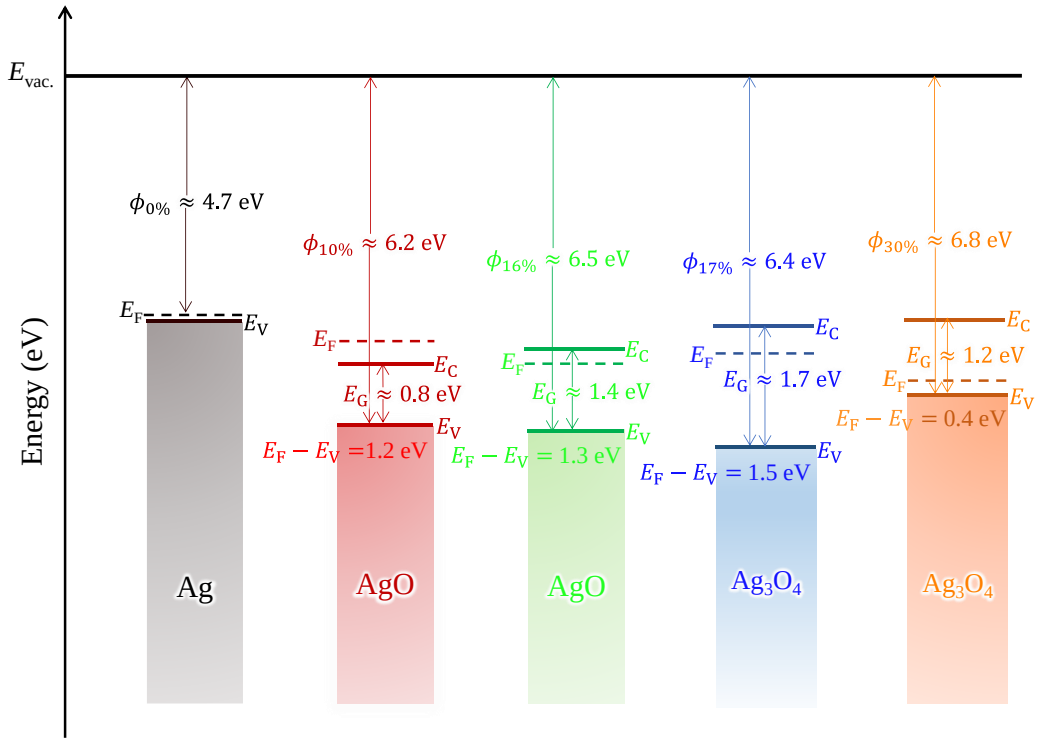

Fig. 5.10. Schematic energy level diagram of Ag_xO with various R[O_2] %.

absorption, is dominant. In this case, it may not be possible to calculate the absorption edge well from the equation of Tauc. For R[O_2] % = 16 %, the semiconductor and/or insulator of AgO was deposited with a resistivity of $8.6 \times 10^5\ \Omega \cdot \mathrm{cm}$, a work function ($\phi$) of 6.5 eV, and a band gap (E_G) of 1.4 eV. The bottom of the conduction band is located at 0.1 eV and the top of the valence band is located at -1.3 eV with respect to the Fermi level. For R[O_2] % = 17 % & 30 %, the deposition sample is a semiconductor and/or insulator of a mixture of $Ag^{(II)}O$ and $Ag_2^{(III)}O_3$ randomly distributed as Ag_3O_4 with a resistivity of $4.1 \times 10^5\ \Omega\cdot$cm (R[$O_2$] = 17 %) and $1.7 \times 10^6\ \Omega\cdot$cm (R[$O_2$] = 30 %) , the work function (ϕ) of 6.4 eV (R[O_2] = 17 %) and 6.8 eV (R[O_2] = 30 %) and the band gap (E_G) of 1.7 eV (R[O_2] = 17 %) and 1.2 eV (R[O_2] = 30 %). The bottom of the conduction band is located at 0.2 eV (R[O_2] = 17 %) and 0.8 eV (R[O_2] = 30 %) and the top of the valence band is located at -1.5 eV (R[O_2] = 17 %) and -0.4 eV (R[O_2] = 30 %) with respect to the Fermi level. However, the valence band energy level and the work function data of 16 % and 17 % may be unreliable because the high resistance leading to the photoelectron cannot be obtained clearly.

5.4 Conclusions

The properties of Ag_xO thin films with various R[O_2] % have been investigated and analyzed using different types of measurements. GIXD spectra and SEM images were used for the crystal structure characterization, and UV-vis spectra and the resistance meter were used for the band gap and resistivity investigations. From GIXD data, it was found that Ag_xO films tended to be a mixture of $Ag^{(II)}O$ and $Ag_2^{(III)}O_3$. To precisely confirm the band gaps of Ag_xO, two different thicknesses of 150 nm and 50 nm were deposited. The PYS spectra were used for work function confirmation. XPS was used to characterize the chemical states of Ag_xO. With an increase in R[O_2] % from 0 % to 30 %, Ag_xO has a variational orientation for AgO (111) to Ag_3O_4 (002) grains, and the band gaps have extended to 1.7 eV but narrowed to 1.2 eV. The chemical states of Ag_xO have been confirmed to be dominated by AgO (R[O_2] % = 10 %

and 16 %) and Ag_3O_4 (R[O_2] % = 17 % and 30 %). To conclude, after processing all the results together, the energy level band has been given but the details of the physical phenomena need furthermore confirmation.

5.5 References

[1] H. Yanagi, S. Inoue, K. Ueda, H. Kawazoe, H. Hosono and N. Hamada: J. Appl. Phys. 88, 4159 (2000). https://doi.org/10.1063/1.1308103

[2] F. X. Bock, T. M. Christensenb, S. B. Riversc, L. D. Doucettea, R. J. Lad. Thin Solid Films 468, 57-64 (2004). https://doi.org/10.1063/5.0000210

[3] S. B. Rivers, G. Bernhardt, M.W. Wright, D.J. Frankel, M.M. Steeves and R.J. Lad: Thin Solid Films 515, 8684 (2007). https://doi.org/10.1016/j.tsf.2007.03.139

[4] W. M. Haynes, David R. Lide, Thomas J. Bruno, CRC Handbook of CheMistry and Physics, Internet Version 2005. http://www.hbcpnetbase.com CRC Press, Boca Raton, FL, 2005.

[5] David Linden, Thomas B. Reddy, 3d ed. 1995, Handbook of Batteries (New York: McGraw-Hill).

[6] David F. Smith, George R. Graybill, Robert K. Grubbs, James A. Gucinski, Journal of Power Sources 65, 47-52, (1997). https://doi.org/10.1016/S0378-7753(97)02467-1.

[7] E. Fortin and F. L. Weichman, Phys. Status Solidi 5, 515-519 (1964). https://doi.org/10.1002/pssb.19640050308

[8] Jong Bok Kim, Chang Su Kim, Youn Sang Kim, et al., Appl. Phys. Lett. 95, 183301 (2009). https://doi.org/10.1063/1.3257361

[9] T. Minami, K. Shimokawa, and T. Miyata, J. Vac. Sci. Technol. A 16,1218 (1998). https://doi.org/10.1116/1.581262

[10] A. J. Varkey, A.F. Fort, Sol. Energy Mater. Sol. Cells 29 (1993) 253. https://doi.org/10.1016/0927-0248(93)90040-A

[11] Jie Wei, Yan Lei, Huimin Jia, Jia Meichen, Hongwei Hou and Zhi Zheng, et al., DaltonTrans., 2014,43, 11333. https://doi.org/10.1039/C4DT00827H

[12] J. Asbalter and A. Subrahmanyam, J. Vac. Sci. Technol. A 18, 1672 (2000). https://doi.org/10.1116/1.582405

[13] T. Ishida, H. Kobayashi, and Y. Nakato, Journal of Applied Physics 73, 4344

(1993). https://doi.org/10.1063/1.352818

[14] A. I. Boronin, S.V. Koscheev, K.T. Murzakhmetov, V. I. Avdeev, G. M. Zhidomirov, Appl. Surf. Sci. 165 (2000) 9. https://doi.org/10.1016/S0169-4332(00)00146-X

[15] X. Y. Gao, S. Y. Wang, J. Li, Y. X. Zheng, R. J. Zhang, P. Zhou, Y. M. Yang and L.Y. Chen: Thin Solid Films 455-456, 438 (2004).

[16] L. A. A. Pettersson, P. G. Snyder, Thin Solid Films 270 (1995) 69. https://doi.org/10.1016/0040-6090(96)80069-1

[17] Subrahmanyam, A., Barik, U.K. Indium doped silver oxide thin films prepared by reactive electron beam evaporation technique: electrical properties. J Mater Sci 42, 6041–6045 (2007).

[18] Barik, Ullash Kumar, et al. "Electrical and optical properties of reactive DC magnetron sputtered silver oxide thin films: role of oxygen." Thin Solid Films 429.1-2 (2003): 129-134. https://doi.org/10.1016/S0040-6090(03)00064-6

[19] M. Allen, S. Durbin. Appl. Phys. Lett. 92, 122110 (2008). https://doi.org/10.1063/1.2894568

[20] G. T. Dang, T. Kawaharamura, et al., Appl. Phys. Lett. 107, 143504 (2015). https://doi.org/10.1063/1.4931960

[21] Y. Magari, M. Furuta, et al., Appl. Surf. Sci. 512, 144519 (2020). https://doi.org/10.1016/j.apsusc.2019.144519

[22] X. Liu, G. T. Dang, L. Liu, T. Kawaharamura, Applied Surface Science 596 (2022) 153465. https://doi.org/10.1016/j.apsusc.2022.153465

[23] M. A. BARTEAU and R. J. MADIX, Journal of Electron Spectroscopy and Related Phenomena, 31, 101-108 (1983). https://doi.org/10.1016/0368-2048(83)80013-9

[24] Waterhouse, G. I. N., G. A. Bowmaker, and J. B. Metson. "Oxidation of a polycrystalline silver foil by reaction with ozone." Applied Surface Science 183.3-4 (2001): 191-204. https://doi.org/10.1016/S0169-4332(01)00561-X

[25] Hoflund G. B., Hazos Z. F., Salaita G. N., Physical Review B-Condensed Matter and Materials Physics, 62, 11126-11133 (2000). https://doi.org/10.1016/S0169-4332(01)00561-X

[26] F. Bock, T. Christensen, S. Rivers, et al., Thin Solid Films 468, 57–64 (2004). https://doi.org/10.1016/j.tsf.2004.04.009

[27] J. F. Pierson, T, C. Rousselot, Surface & Coatings Technology, 200, 276–279 (2005). https://doi.org/10.1016/j.surfcoat.2005.02.005

[28] Tseng, C. C., et al. "Effects of deposition and annealing temperatures on the electrical and optical properties of Ag_2O and Cu_2O–Ag_2O thin films." Journal of Vacuum Science & Technology A: Vacuum, Surfaces, and Films 28.4 (2010): 791-794. https://doi.org/10.1116/1.3425638

[29] Schmidt, A. A., J. Offermann, and R. Anton. "The role of neutral oxygen radicals in the oxidation of Ag films." Thin Solid Films 281 (1996): 105-107. https://doi.org/10.1016/0040-6090(96)08586-0

[30] Fortin, E., and F. L. Weichman. "photoconductivity in Ag2O." physica status solidi (b) 5.3 (1964): 515-519. https://doi.org/10.1002/pssb.19640050308

[31] Suzuki, Ryosuke O., Takamichi Ogawa, and Katsutoshi Ono. "Use of ozone to prepare silver oxides." Journal of the American Ceramic Society 82.8 (1999): 2033-2038. https://doi.org/10.1111/j.1151-2916.1999.tb02036.x

[32] Usategui, Magdalena, "Higher Oxidation States of Silver." (1961). LSU Historical Dissertations and Theses. 658. https://doi.org/10.31390/gradschool_disstheses.658

[33] S. Burkhard, and M. Jansen, Journal of Solid State Chemistry 67, 278-284 (1987).

[34] Fischer, Peter, and Martin Jansen. "Cyclovoltammetrische-und Röntgenbeugung-suntersuchungen zur anodischen abscheidung Höherer silberoxide." Solid State Ionics 43 (1990): 61-67. https://doi.org/10.1016/0167-2738(90)90471-3

[35] Mansour, A. N. "Evidence for an Ag_4O_3 phase of silver oxide." Journal of Physical Chemistry 94.2 (1990): 1006-1010.

[36] McMillan, Juan A. "Magnetic properties and crystalline structure of AgO." Journal of Inorganic and Nuclear Chemistry 13.1-2 (1960): 28-31. https://doi.org/10.1016/0022-1902(60)80231-X

[37] Graff, William S., and Hans H. Stadelmaier. "Higher oxides of silver." Journal of The Electrochemical Society 105.8 (1958): 446. https://doi.org/10.1149/1.2428887

[38] Hamberg, Ivar, and Claes G. Granqvist. "Evaporated Sn-doped In_2O_3 films: Basic optical properties and applications to energy-efficient windows." Journal of Applied physics 60.11 (1986): R123-R160. https://doi.org/10.1063/1.337534

[39] Urbach, Franz. "The long-wavelength edge of photographic sensitivity and of the electronic absorption of solids." Physical Review 92.5 (1953): 1324. https://doi.org/10.1103/PhysRev.92.1324

[40] Wei-Xue Li, Catherine Stampfl, and Matthias Scheffler. "Insights into the function of silver as an oxidation catalyst by ab initio atomistic thermodynamics." Physical Review B 68.16 (2003): 165412. https://doi.org/10.1103/PhysRevB.68.165412

[41] Ishii, Hisao. "Photoelectron yield spectroscopy." Compendium of Surface and Interface Analysis (2018): 457-463. https://doi.org/10.1007/978-981-10-6156-1_75

[42] Yasuo Nakayam, Hisao Ishii et al., Applied Physics Letters 93, 173305 (2008);

[43] Weaver, Jason F., and Gar B. Hoflund. "Surface characterization study of the thermal decomposition of Ag_2O." Chemistry of materials 6.10 (1994): 1693-1699.

[44] Gaarenstroom, S. W., and N. J. T. J. Winograd. "Initial and final state effects in the ESCA spectra of cadmium and silver oxides." The Journal of chemical physics 67.8 (1977): 3500-3506. https://doi.org/10.1063/1.435347

[45] Rehren, C., et al. "Surface and subsurface products of the interaction of O_2 with Ag under catalytic conditions." Catalysis letters 11 (1991): 253-265. https://doi.org/10.1007/BF00764316

[46] Schön, Gunnar, et al. "ESCA studies of Ag, Ag_2O and AgO." Acta Chem. Scand 27.7 (1973): 2623.

[47] Hammond, J. S., S. W. Gaarenstroom, and Nicholas Winograd. "X-ray photoelectron spectroscopic studies of cadmium-and silver-oxygen surfaces." Analytical CheMistry 47.13 (1975): 2193-2199.

[48] A. Savitzky, M. J. E. Golay, Anal. Chem. 36, 1627 (1964).

[49] Bukhtiyarov, V. I., et al. "The state of oxygen on the surface of polycrystalline silver." Reaction Kinetics and Catalysis Letters 39 (1989): 21-26.

[50] Charles T. Campbell, and Mark T. Paffett. Surface science 143.2-3 (1984): 517-535.

[51] G. Zhang, P. Yan, P. Wang, Y. Chen, J. Zhang, The preparation and mechanical properties of Al-containing a-C: H thin films, J. Phys. D Appl. Phys. 40 (2007) 6748–6752.

[52] K. Baba, R. Hatada, Deposition and characterization of Ti- and W-containing diamond-like carbon films by plasma source ion implantation, Surf. Coat. Technol. 169–170 (2003) 287–290.

[53] Behrens, P. "Bonding in silver-oxygen compounds from Ag L_3 XANES spectroscopy." Solid state communications 81.3 (1992): 235-239. https://doi.org/10.1016/0038-1098(92)90506-5

[54] Bigelow, Richard W. "An XPS study of air corona discharge-induced corrosion products at Cu, Ag and Au ground planes." Applied Surface Science 32.1-2 (1988): 122-140. https://doi.org/10.1016/0169-4332(88)90077-3

[55] Jansen Martin. "Homoatomic d10–d10 interactions: their effects on structure and chemical and physical properties." Angewandte Chemie International Edition in English 26.11 (1987): 1098-1110. https://doi.org/10.1002/anie.198710981

[56] P. Behrens, Z. anorg. allg. chem., 625, 1116, (1999).

[57] M. Romand, M. Roubin, J. P. Deloume, J. Electron. Spectr. Relat. Phenom. 13 (1978) 229. https://doi.org/10.1016/0368-2048(78)85029-4

[58] L. H. Tjeng, M. B. J. Meinders, J. van Elp, J. Ghijsen, G. A. Savatsky, and R. L. Johnson, Phys. Rev. B 41, 3190 (1990). https://doi.org/10.1103/PhysRevB.41.3190

Chapter 6

Fabrication of $Zn_{1-x}Mg_xO/Ag_yO$ Heterojunction Diodes by Mist-CVD at Atmospheric Pressure

This chapter discusses the electrical characteristics of junctions formed between ZnMgO and Ag_yO. The performance of ZnMgO/Ag_yO HJDs is optimized by adjusting the synthesis condition in two directions: 1) influence of pre-treatment such as O_3 treatment, H_2O treatment, ICP treatment, pre-annealing in air (PAA), and pre-annealing in N_2 (PAN); 2) influence of the Mg component of the ZnMgO layer and R[O_2] % of Ag_yO films, and R[O_2] % = [O_2 / (O_2 + Ar)] %, where the total flow rate of oxygen and argon [O_2 + Ar] = 10 sccm. In addition, band diagrams near the heterostructure interface formed by two different materials are discussed.

6.1 Introduction

Semiconductor heterojunctions have been extensively proposed and investigated as the building blocks of many novel solid-state devices for more than a quarter of a century [1]. Differences in the band gaps, electron affinities, and refraction indexes of the composed materials combined together as such a type of heterostructure of the multilayers can independently confine photons or electrons in different regions of a crystal [2].

Among the materials that are used in such junctions, oxide-based thin films are of increasing interest. In particular zinc oxide (ZnO) [3] and indium tin oxide (ITO) [4] are two well-studied oxide-based materials for ultraviolet photodetectors [5], light-emitting diodes (LEDs) [6, 7], laser diodes (LDs) [8], and field-effect transistors (FET) [9, 10]. One of the significant advantages is that the exciton binding energy of ZnO (60 meV) [11] is more than two times higher than that of GaN (24 meV) [12]. For this reason, ZnO-based heterostructures may be preferable to GaN-based material systems for applications in the ultraviolet-visible range [13]. For example, several researchers

have reported methods to fabricate homojunctions of ZnO-based devices [14-17].

However, there are some crucial issues related to the realization of these ZnO-based devices, such as the requirement to grow high-quality p-n junctions of ZnO thin films being limited due to the difficulties in the production of p-type materials [17, 18]. To extend the applications of ZnO-based devices, the utilization of doping or alloying with MgO to control the band gap energy of ZnO films may be a substitute proposal to deal with this conundrum [19]. The ionic radius of Mg^{2+} (0.57 Å) and Zn^{2+} (0.60 Å) are comparable [20]. The $Zn_xMg_{1-x}O$ alloy films are expected to be a suitable potential barrier material [21, 22]. A tunable band gap can be obtained from the mixture of ZnO (band gap = 3.3 eV) and MgO (band gap = 7.8 eV) by varying the atomic composition of Mg. Furthermore, the fabrication of Schottky contacts on Ag_yO/ZnO and Ag_yO /IGZO had been accomplished by M. W. Allen et al and Y. Magari et al [23, 24]. According to the above statement, oxide-based thin films have been successfully deposited by vacuum-based processing techniques. The vacuum-based deposition technology demanded the anti-pressure ability of the system chambers, but because of its robustness, high reactive and toxic source materials were allowed. This may have an influence on our environment because of their high energy consumption and environmental pollution. In contrast, non-vacuum growth methods such as spray pyrolysis, aerosol assisted CVD process, mist-CVD process, etc., have been developed, and the vacuum condition is required to simplify the thin film deposition procedures without overburdening the environment. For example, various kinds of thin films and devices fabrication have been reported by using the mist-CVD method.

6.2 Experimental Methods

The fabrication of heterojunction diodes (HJDs) was performed using photolithography and lift-off processes. The photoresist was spin-coated on ZnMgO thin films (~300 nm thick) with different Mg compositions grown on top of ITO films [33] (~200 nm thick. Subsequently, to form a mesa structure on such ZnMgO/ITO wafer, the covered photoresist was removed from one corner by acetone, and then the exposed ZnMgO layer was etched with 1 % HCl solution for 1 min. Circular diodes of different diameters (100 μm ~1000 μm) were patterned by UV lithography and developed using tetramethylammonium hydroxide (TMAH) for 20 s followed by a final rinse in deionized (D.I.) water and drying in an N_2 gas gun. The Ag_yO film (~100 nm

thick) was then deposited on top of ZnMgO/ITO by radio-frequency magnetron sputtering (RFM-SPT). A capping layer of Au was then deposited onto the silver oxide thin film by the electron beam evaporation process. The Ag_yO/Au bilayer anodes were patterned by the lift-off process. A schematic of the resulting heterostructures grown (a) and cross-section TEM micrograph (b) are shown in Fig. 6.1.

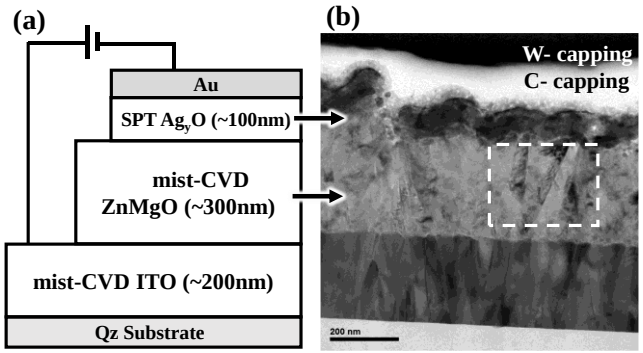

Fig. 6.1.(a) Schematic diagram (b) Cross-section TEM micrograph of ZnMgO/Ag_yO HJDs.

Table 6-1 Mist-CVD deposition conditions for ITO & ZnMgO films

		Chamber A	Chamber B	Chamber C
ITO	Sour. Conc.	MeOH + $InCl_3$ + $SnCl_2$ 45 mM : 5 mM	H_2O + HNO_3 + HCl 98.7 : 0.8 : 0.5	----
	c.g. / d.g. (l / min)	2.0 / 3.0	0.2 / 4.8	----
ZnMgO	Sour. Conc.	MeOH + $Zn(acac)_2$ 50 mM	MeOH + $Mg(acac)_2$ 20 mM	MeOH + H_2O 97 : 3
	c.g. / d.g. (l / min)	2.5 / 2.5	0.5 / 4.5 ~ 2.0 / 3.0	2.0 / 3.0
Growth time& Temp.		ITO (180 s & 400℃), ZnMgO (600 s & 400℃)		
Ultrasonic transducer		2.4 MHz, 24 V, 0.625 A		

Table 6-2 RFM-SPT deposition conditions for Ag_yO films

Target	R[O_2] (%)	Pressure (Pa)	Power (W)	Thickness (nm)	Growth T. & Temp.
Ag	0 ~ 30	~0.3	40	~100	17 min & RT

The details of the experiment conditions of each layer are summarized in Table 6-1 and Table 6-2. The film thickness of the ZnMgO and the ITO were obtained from a spectroscopic ellipsometer (J.A. Woollm, W-VASE). The specific properties of every single have been presented in previous chapters. The cross-section micrograph of the completed device was applied by transmission electron microscopy (TEM) measurement. The current density-voltage (J-V) characteristics of the ZnMgO/Ag_yO HJDs

were characterized by a Keysight B1506A power device analyzer at room temperature (RT) in the dark.

6.3 Results and Discussions

6.3.1 With Pre-treatment J-V Characteristics of ZnMgO/Ag$_y$O HJDs

As shown in Fig. 6.2 is the J-V characteristics in random areas of ZnMgO/Ag$_y$O HJDs in comparison with different pre-treatment (pre-Tr). For sample #6, the ZnMgO film was grown without O_3 assistance, and Ag$_y$O was deposited at R[O_2] % = 16 %. Pre-treatment with H_2O or pre-treatment with O_3 was carried out at 400 ℃ for 3 mins before Ag$_y$O deposition. Compared to the absence of pre-treatment, pre-treatment

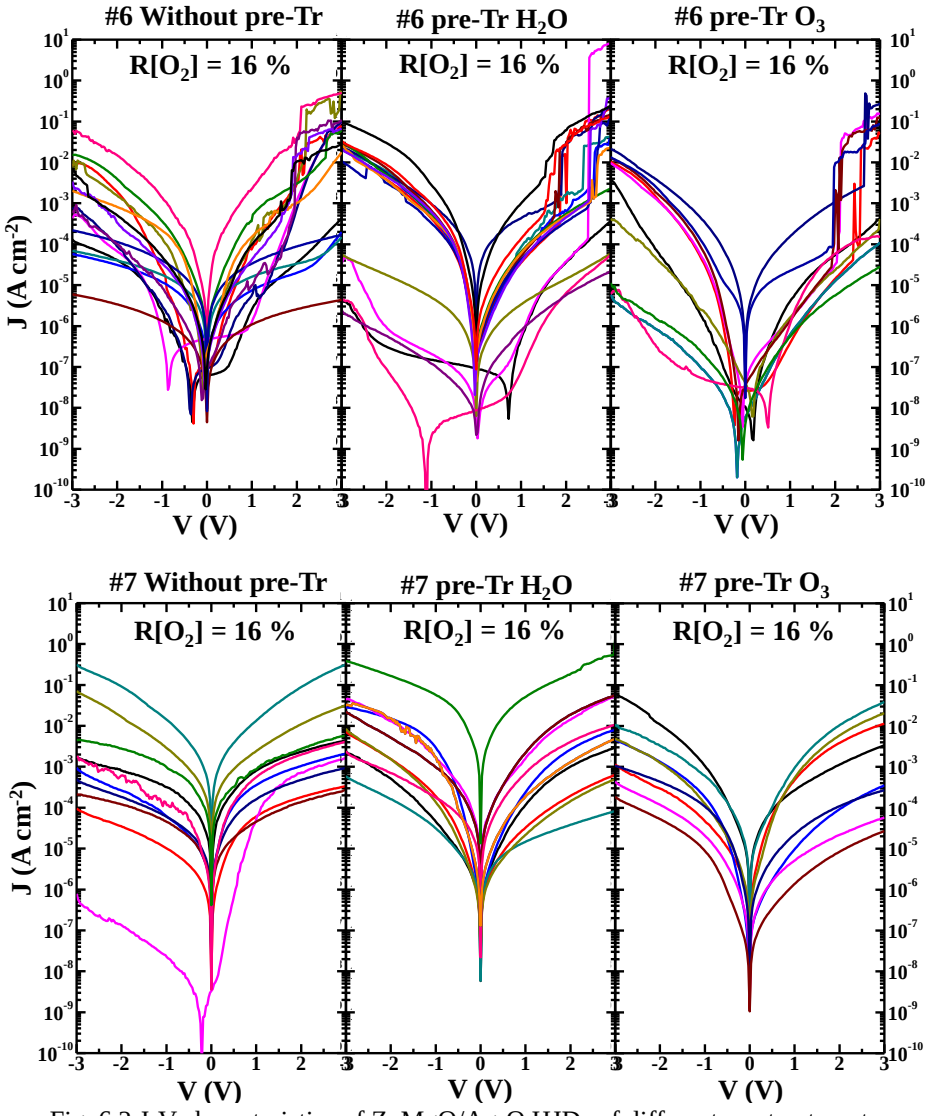

Fig. 6.2 J-V characteristics of ZnMgO/Ag$_y$O HJDs of different pre-treatment

with H_2O had a better effect on suppressing reverse current, since the rectifying ratio was around 10^5 magnitudes for the applied voltage at $+3/-2$ V, shown in the purple color, and others did not show obvious rectifying behavior. This improvement might come from pre-treatment with H_2O and O_3 compensating the oxygen vacancies. Another phenomenon is that after pre-treatment jumping current constantly appeared for applying + 2.5 V forward bias.

For sample #7, the ZnMgO film was grown with O_3 assistance, and Ag_yO was also deposited at R[O_2] % = 16 %. There was no rectifying behavior after pre-treatment with H_2O and O_3. However, for the sample without pre-treatment, a rectifying behavior of 10^5 magnitudes was present for the applied voltage at $+3/-2$ V, shown in purple color. This suggests that during ZnMgO depositions, the introduction of O_3 could reduce the dangling bonds of Zn and Mg. At the same time, although the current for sample #7 was more stable and no jumping current was shown in compared to sample #6, the same phenomenon of the saturation current shifting may be due to insufficient barrier height.

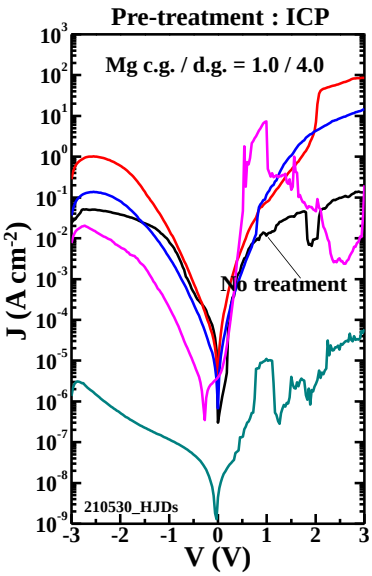

Fig. 6.3 J-V characteristics of ZnMgO/Ag_yO HJDs of ICP pre-treatment

Fig. 6.3 shows the J-V characteristic measuring in random areas of ZnMgO/Ag_yO HJDs with ICP pre-treatment in 2 mins. Compared to the no treatment sample, which is shown in black color, there were three areas that showed slightly rectifying behavior for the forward current being increased but the reverse current almost kept the same as before pre-treatment, and the green color showed even worse result. This may be caused by high power-induced plasma damaging the sample surface.

To summarize briefly, pre-treatment with O_3, H_2O, ICP did not get the expected results referring to the rectify ratios of that before and after pre-treatment.

Fig. 6.4 shows the J-V characteristic of ZnMgO/Ag_yO HJDs with pre-annealing in N_2 (PAN) and pre-annealing in air (PAA) at 400 ℃ 1-hour of which it was grown with (a) Mg c.g. / d.g. = 1.0 / 4.0 and (b) Mg c.g. / d.g. = 2.0 / 3.0. From Fig. 6.4 (a), we can see that there is an apparent improvement corresponding to before and after annealing compared to without annealing, as shown in black color. Meanwhile, comparing with Fig. 6.3 (b), in the sample grown with Mg c.g. / d.g. increasing to 2.0 / 3.0., the reverse current was further suppressed. This may come from the higher band gap energy level for more Mg atom incorporation. These results suggest that pre-annealing treatment supplies oxygen or N atom decreased oxygen vacancies.

6.3.2 Without Pre-treatment J-V Characteristics of ZnMgO/Ag_yO HJDs

As shown in Section 6.2, Fig. 6.1 shows (a) schematic diagram and (b) cross-section TEM micrograph of ZnMgO/Ag_yO HJDs. These structures demonstrate the possibility of growth multi-layers with the thickness needed by using Mist-CVD system. Before formal preparation of the devices, the growth rate was checked. Then, depending on the growth rate, the deposition time of the thickness of each layer needed was determined. This process was properly proved by TEM micrograph. The clear

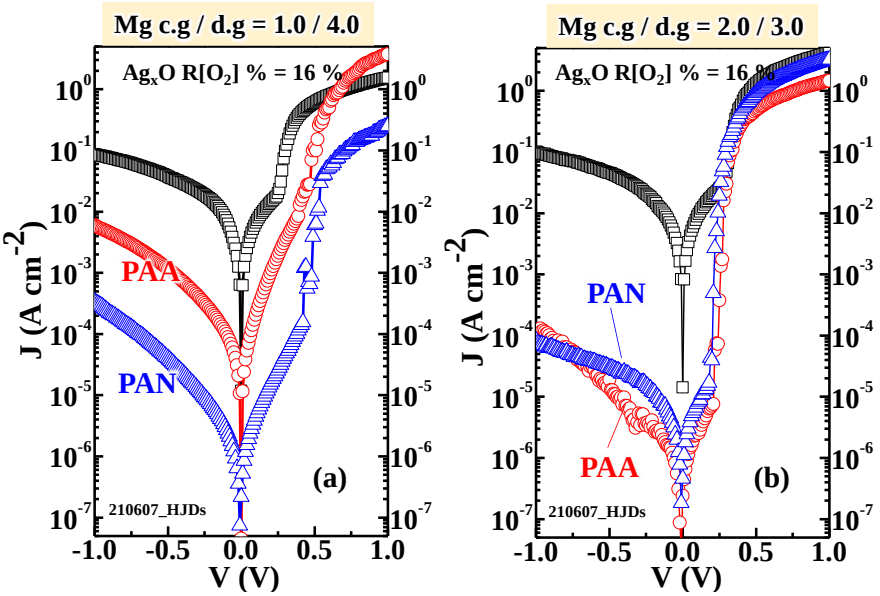

Fig. 6.4 J-V characteristic of ZnMgO/Ag_yO HJDs with pre-annealing in N_2 (PAN) and pre-annealing in air (PAA) at 400 ℃ 1 hour
(a) Mg c.g. / d.g. = 1.0 / 4.0 (b) Mg c.g. / d.g. = 2.0 / 3.0.

observation that each film had been stacked in the deposition order can be seen by the black arrows shown in Fig. 6.1 (b), corresponding to the Au/Ag_yO layer and the ZnMgO layer, respectively. The rim of Ag_yO shows the bubble shape of the topside that was inter-formed nearby the C-capping layer. The reason is that the TEM measurement was performed a long time after the device deposition, and the device was preserved in the atmosphere, thereby, oxygen and humidity re-oxidized and/or changed Ag_yO to hydroxide. Furthermore, it should be noted that there was an additional oxide interfacial layer between the Ag_yO and ZnMgO, which means that there is a gap between Ag_yO and ZnMgO, and it ended up forming as an interfacial oxidation layer. The square region marked the oblique area, which exists in the ZnMgO layer. As can be seen, the partial inclinations originally resulted from the ITO layer, and such areas bounded by the partially tilted crystals ended up as an abrupt edge of grain boundaries. In general, the properties of devices may follow in crystal orientation, so the tilted crystal grain is responsible for the abrupt jumping current behavior as suggested from the analysis of I-V characteristics of the HJDs. However, their properties have been reported to become more uniform, as crystals with various orientations are assembled in such a disordered manner in a certain amount [34].

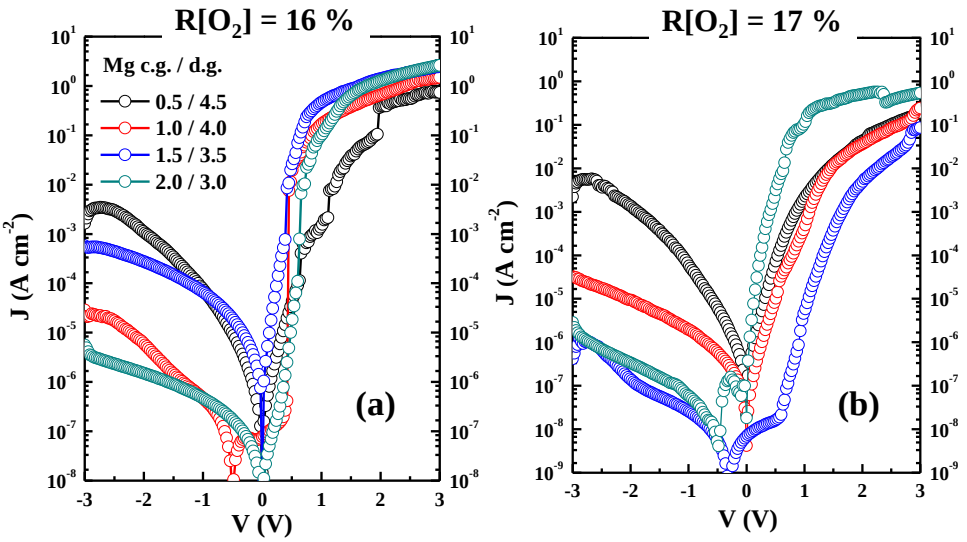

Fig. 6.5 J-V characteristics of ZnMgO/Ag_yO HJDs of Mg content dependence

The J-V characteristics of the ZnMgO/Ag_yO HJDs of R[O_2] = 16% & 17% in comparison of the dependence of the Mg content at room temperature, are shown in Fig. 6.5. From Fig. 6.5 (a) R[O_2] = 16 % with an increase in the Mg c.g. / d.g. of the ZnMgO/Ag_yO HJDs had a rectifying behavior [35], and when the Mg c.g. / d.g. in-

creased to 2.0 / 3.0, it exhibited the highest rectifying behavior, which is $J_{on/off} = 1.47 \times 10^7$ for the applied voltage at $+3/-0.5$ V. The heterojunctions showed rectifying behavior might have two possibilities. One of them has sufficient barrier height between ZnMgO and Ag_yO, which will protect the carriers from freely moving and with the electrostatic field's assistance to flow in one direction. Another theory is that Ag_yO may act as a p-type material. In addition to the separate experiments in the single layer of n-ZnMgO, when the Mg c.g. / d.g. increased to 2.0 / 3.0, the Mg content x = 0.23, the film exhibited high resistance compared to the Mg content x = 0.08, which is the $\rho = 1.58 \times 10^8 \Omega \cdot cm$. The higher resistivity ascribing to the higher Mg combination of the ZnMgO active layer was plausible for such wider band gaps achievements and thus would be capable of blocking current flow freely, and as a consequence, the reverse current density was deduced by almost 3 order magnitude at -3 V. However, the increment of the Mg content also led to crystallinity degradation, and this might give rise to the unevenly jumping performance of the J-V characteristics. And such abrupt jumping behaviors might be interpreted as the surface between ZnMgO and Ag_yO existed an interfacial layer that had a large number of surface states (dangling bonds or defects) [36], this understanding is supported by the TEM micrograph observation. Structural fluctuations or the resulting disorders, all could be the reasons for the abrupt jumping current behavior [37].

When R[O_2] % increased to 17 % the dependence of Mg content of the J-V characteristics is shown in Fig. 6.5 section (b). The forward current density of HJDs decreased by an order of magnitude at $+3$ V compared to as grown junctions with R[O_2] = 16 % at the same Mg component. Presumably, this improvement might be explained that the increase in R[O_2] % provided extra oxygen in the reaction chamber. Therefore, O-rich ambiance could possibly repair or decline the dangling bonds in the films, as suggested from the analysis of the chemical bonding states of Ag_yO films by hard X-ray photon electron spectroscopy (HXPS) measurement reported earlier in ref. 24. When Mg content x = 0.19, the n-p junction shows an abruptly diffusion limited current at approximately 0.8 V and after that, the current increased exponentially. And, in x = 0.23, the junction encompassed a broad shoulder on the forward voltage side, but near the interfacial region, some unusual jumping current at reverse voltage -0.5 V can be seen. This might be caused by the abrupt edges at the grain boundaries. Such results of pre-annealing or post-annealing treatment are effective approaches to en-

hance the performance of the device according to reports from other studies. These parts of improvement of the properties of thin films and oxide HJDs will be discussed in further reports.

Table 6-3 ZnMgO/Ag$_y$O HJDs electrical properties

Mg content	R[O_2]%	$J_{on/off}$ @ 3V/-0.5V	$J_{F/R}$ @ ± 3 V	φ_b	n
x = 0.08	16%	7.28×10^4	4.47×10^2	0.78	3.68
x = 0.17	16%	2.21×10^8	5.19×10^4	-----	----
x = 0.19	16%	1.25×10^5	4.26×10^3	0.75	1.89
x = 0.23	16%	1.47×10^7	4.63×10^5	0.92	1.84
x = 0.08	17%	8.51×10^2	1.37×10^1	0.59	4.27
x = 0.17	17%	3.98×10^5	7.49×10^3	0.81	4.33
x= 0.19	17%	1.45×10^7	2.11×10^5	1.01	3.32
x = 0.23	17%	1.01×10^8	1.86×10^5	0.68	3.45

The barrier heights of ZnMgO/Ag$_y$O HJDs were determined from thermionic emission theory [38, 39] by fitting the forward J-V characteristics. The theoretical relation between current density and voltage is expressed as:

$$J = A^* T^2 \exp\left(-\frac{q\varphi_b}{k_B T}\right)\left[\exp\left(\frac{qV}{nkT} - 1\right)\right],$$

where $A^*$is the effective Richardson constant that was obtained from the effective electron mass in ZnMgO m^* = 0.27 m_0 so that $A^*$of ZnMgO [40, 41] is estimated as 32 A cm^{-2} K^{-2}, V is the applied voltage, n is the ideality factor, k is the Boltzmann constant and T is the absolute temperature.

Only the good performance J-V characteristics were discussed here. The barrier height φ_b = 0.75 eV was extracted with the ideality factor n = 1.89 for the HJDs which was Mg x = 0.19 of the ZnMgO layers and R[O_2] = 16 % of the Ag$_y$O films. Apparently, the fermi level was pinned at the E_c ~ 0.75 eV defect level. And as Mg x = 0.23, barrier height φ_b was increased to 0.92 eV. This could be explained by the magnitude of the electron affinity of the compounds, i.e., $\chi_{MgO} < \chi_{ZnO}$ [42, 43] resulted in the higher conduction band offsets. And when R[O_2] % increased to 17 % and x = 0.19, the extracted barrier height is 0.98 eV, which varied 0.23 eV compared to R[O_2] = 16 % at the same Mg content. This variation should come from the Ag$_y$O layer. According to the measurement results of the PYS and Hall effect, when R[O_2] % increased from 15% to 20% (included R[O_2] = 16 % & R[O_2] = 17%), the work function of Ag$_y$O increased from 4.7 eV to 5.2 eV. It suggests that this change might be

caused by the increased combination number of the higher electronegativity of O ions [44]. The electric properties of the dependence of the Mg content and the dependence of R[O_2] % in the ZnMgO/Ag$_y$O HJDs were summarized (Table 6-3).

In addition by tabulating the information from the electric properties of the junctions and GIXD data of ZnMgO, it suggests that Mg c.g. / d.g. = 1.5 / 3.5 and R[O_2] = 17 % might be more suitable for device preparation. And this condition will be used for future pre-annealing experiments.

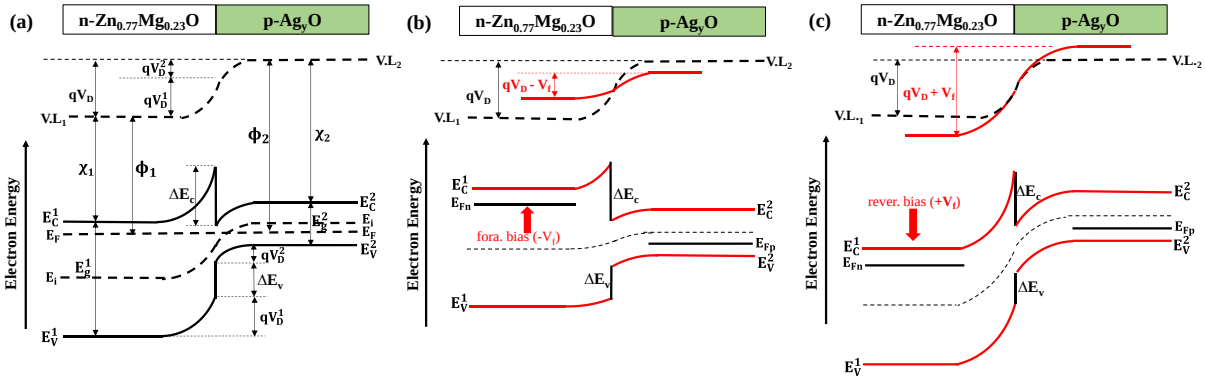

Fig. 6.6 Schematic energy diagram of the interface between ZnMgO/Ag$_y$O HJDs

For illustration of the design concept and the work principle of the devices, the energy band diagram around the active area of the interface for the n-p heterojunction of ZnMgO/Ag$_y$O is shown in Fig. 6.6. The features of the band alignment are determined based on the Anderson electron affinity rule [37]. The vacuum level is always parallel to the conduction and valence bands and continuous, and the wide band gap ZnMgO overlaps the narrow band gap Ag$_y$O at equilibrium (a). When n-ZnMgO applied forward bias as shown in Fig. 6.6 (b), due to the electrostatic field the E_{Fn} of ZnMgO shifted upward, the E_{Fp} of p-Ag$_y$O moved to the lower energy level, assuming that the quasi-fermi level of an electron was E_{Fn}, the quasi-fermi level of a hole was E_{Fp}. In Fig. 6.6 (c) as reverse bias case, there is no current flow across the junction due to the barrier potential effect. However, the difference in dielectric constants in the two films results in a discontinuous electrostatic field at the interface [37], and the two forces of the electric field are unequal, hence the band structure becomes position dependent [45]. Furthermore, such differences in the energy of the edges of the conduction band in ZnMgO/Ag$_y$O are represented by ΔE_c and in the edges of the valence band by ΔE_v, where χ is the electron affinity, ϕ is work function, E_g is band gap, and subscripts 1 and 2 correspond to ZnMgO and Ag$_y$O, respectively. The band gap of

ZnMgO by alloying Mg x = 0.23 is $E_g^1 = 3.7\text{eV}$, the electron affinity of ZnMgO to be taken as $\chi_1 = 3.67$ eV [44, 45]. The electron affinity of Ag_yO (R[O_2] = 17 %) is assumed to be $\phi_2 = \chi_2 = 4.8$ eV, which was obtained from the PYS spectrum. This is because the electrostatic field exerted on the band edges and interface charges around the interface area might cause the Ag_yO conduction band edge to be bent downward to the Fermi band, thus, the work function of Ag_yO would be considered same as electron affinity in this discussion. The band gap of Ag_yO (R[O_2] = 17 %) is $E_g^2 = 2.18$ eV. As a result, the discontinuities were determined as $\Delta E_c = \chi_2 - \chi_1 = 1.13$ eV, $\Delta E_v = E_g^1 - E_g^2 - \Delta E_c = 0.39$ eV.

The conduction band discontinuity is quite larger than the valence band discontinuity. Also, this reveals that there is a discrepancy in the Schottky barrier heights and heterointerface band offsets. Or, such discrepancy may originally come from the abrupt edge of grain boundaries. Consequently, these grain boundaries seem to give inferior effects on the barrier potential and may result in different magnitude electrostatic forces on electrons and holes. Thus, the barrier height and band offsets are deeply dependent on the position of the interface, and this result well agrees with H. Kroemer [45]. Now we just obtained these results, but from the analysis perspective the current problem will be further identified in the future, and the results will be used as an index for forming higher performance devices.

6.4 Conclusions

We proposed a growth trial of ZnMgO/Ag_yO heterojunction by mist-CVD system and sputtering deposition techniques. Mist-CVD can be applied for device preparation. The junctions between the ZnMgO and Ag_yO had rectifying behavior and presented an abrupt interface, and there are discrepancies in the Schottky barriers and interface band offsets. Pre-treatments with N_2 (pre-N_2) & pre-treatments with Air (pre-Air) for annealing at 400 ℃ 1h could improve the surface of $Zn_{1-x}Mg_xO$. Partial oxidized Ag_yO could improve the surface of $Zn_{1-x}Mg_xO$, at the Mg content of x = 0.17, the HJDs of R[O_2] = 17% performed better than the HJDs of R[O_2] = 16%. $Zn_{1-x}Mg_xO$ has the potential as a wide band gap to be used for electric devices (I-V characteristics). In the future, we will continue to optimize the structure and fabrication process of ZnMgO to further improve the performance of heterojunctions.

6.5 References

[1] Giorgio Margaritondo, *Electronic Structure of Semiconductor Heterojunctions* (1988).

[2] L. J. Brillson, G. K. Sujan, Semiconductor Heterojunctions, An Essential Guide to Electronic Material Surfaces and Interfaces, (2016).

[3] H. E. Brown, Zinc oxide: *Properties and applications, International Lead Zinc Research Organization* (1976).

[4] H. L. Hartnagel et al., Semi. Trans. *Thin Films Institute of Physics, Bristol* (1995).

[5] S. Liang, H. Sheng, Y. Liu, Z. Huo, Y. Lu, H. Shen, J. Crystal. Growth. 225, 110 (2001).

[6] A. Tsukazaki, A. Ohtomo, T. Onuma, M. Ohtani, T. Makino, M. Sumiya, K. Ohtani, et al., Nature Mater. 4, 42-46 (2005).

[7] D. K Hwang, S. H. Kang, J. H. Lim, et al., Appl. Phys. Lett. 86, 222101 (2005).

[8] S. J. Pearton, F. Ren, Inter. Mater. Revi., 59, 2 (2014).

[9] K. Keem, D.Y. Jeong, S. Kim, M.S. Lee, I.S. Yeo, U.I. Chung, J.T. Moon, Nano Lett. 6, 1454 (2006).

[10] J. Y. Kwon, D. J. Lee, K. B. Kim, Electron. Mater. Lett., Vol. 7, 1 (2011).

[11] D. G. Thomas, J. Phys. Chem. Solids 15, 86-96 (1960).

[12] K. Torii, T. Deguchi, T. Sota, K. Suzuki, S. Chichibu, S. Nakamura, Phys. Rev. B 60, 4723 (1999).

[13] D. C. Look, Mater. Sci. Eng. B 80, 383-387 (2001).

[14] X. L. Guo, J.H. Choi, H. Tabata, T. Kawai, Jpn. J. Appl. Phys. 40, L177 (2001).

[15] A. Tsukazaki, M. Kubota, A. Ohtomo, T. Onuma, K. Ohtani, H. Ohno, S.F. Chichibu, M. Kawasaki, Jpn. J. Appl. Phys. 44, L643 (2005).

[16] Y. Ryu, T. S. Lee, J. A. Lubguban, H. W. White, B. J. Kim, Y. S. Park, C. J. Youn, Appl. Phys. Lett. 88, 241108 (2006).

[17] Ü. Özgür, Y. I. Alivov, et al., J. Appl. Phys. 98, 041301 (2005).

[18] H. Yang, Y. Li, D.P. Norton, S.J. Pearton, S. Jung, et al., Appl. Phys. Lett. 86, 172103 (2005).

[19] A. Osinsky, J.W. Dong, M.Z. Kauser, B. Hertog, A.M. Dabiran, et al., Appl. Phys. Lett. 85, 4272 (2004).

[20] R. D. Shannon, Acta Cryst. A32, 751 (1976).

[21] J. G. Yoon, S. W. Cho, E. Lee, J. S. Chung, Appl. Phys. Lett. 95, 222102 (2009).

[22] R. C. Boutwell, M. Wei, W. V. Schoenfeld, Appl. Phys. Lett. 103, 031114 (2013).

[23] M. W. Allen, S. M. Durbin, J. B. Metson, Appl. Phys. Lett. 91, 053512 (2007).

[24] Y. Magari, M. Furuta, et al., Appl. Surf. Sci. 512, 144519 (2020).

[25] T. Kawaharamura, T. Hirao, Jpn. J. Appl. Phys. 51, 036503 (2012).

[26] T. Kawaharamura, G. T. Dang, M. Furata, Jpn. J. Appl. Phys. 51, 040207 (2012).

[27] T. Kawaharamura, T. Uchida, M. Sanada, D. Wang, M. Furuta et al., Phys. Status Solidi C 10, No. 11, 1565–1568 (2013).

[28] T. Kawaharamura, T. Uchida, M. Sanada, M. Furuta, AIP Adv. 3, 032135 (2013).

[29] G. T. Dang, T. Kawaharamura et al., Applied Physics Express 9, 041101 (2016).

[30] L. Liu, T. Kawaharamura, G. T. Dang, E. K. C. Pradeep, S. Sato, T. Uchida, S. Fujita, T. Hiramatsu, H. Kobayashi, H. Orita, Jpn. J. Appl. Phys. 58, 025502 (2019).

[31] P. Rutthongjan, L. Liu, M. Nishi, M. Sakamoto, S. Sato, G. T Dang, T. Kawaharamura, Jpn. J. Appl. Phys. 58, 035503 (2019).

[32] G. T. Dang, S. Sato, Y. Tagashira, T. Yasuoka, L. Liu, T. Kawaharamura, APL Mater. 8, 101101 (2020).

[33] T. Kawaharamura, Jpn. J. Appl. Phys. 53, 05FF08 (2014).

[34] W. I. Park, G. C. Yi, H. M. Jang, Appl. Phys. Lett. 79, 2022 (2001).

[35] T. S. Kuan, T. F. Kuech, W. I. Wang, E. L. Wilkie, "Long range order in $Al_xGa_{1-x}As$." Phys. Rev. Lett. 54, 201-204 (1985).

[36] H. K. Henisch, Rectifying Semiconductor Contacts (Clarendon, Oxford, 1957).

[37] W. Shockley, "On the Surface States Associated with a Periodic Potential," Phys. Rev. 56, 317 (1939).

[38] R. L. Anderson, Solid-State Electronics 5, 341-351 (1962).

[39] E. H. Rhoderick, R. H. Williams, *Metal–Semiconductor Contacts vol 129 (Oxford: Clarendon* 1988*).*

[40] S. M. Sze, K. K. Ng, *Physics of Semiconductor Devices 3rd edn (Wiley: Inter-science* 2007*).*

[41] K. Sarpatwari, O. O. Awadelkarim, M. W. Allen, et al., Appl. Phys. Lett. 94, 242110 (2009).

[42] K. Sarpatwari, S. E. Mohney, O. O. Awadelkarim, J. Appl. Phys. 109, 014510 (2011).

[43] P. V. Sushko, J. L. Gavartin, A. L. Shluger, J. Phys. Chem. B 06, 2269-2276

(2002).

[44] B. J. Coppa, C. C. Fulton, S.M. Kiesel, R.F. Davis, et al., J. Appl. Phys. 97, 103517 (2005).

[45] R. P. Iczkowski, J. L. Margrave, Journal of the American Chemical Society 83(17), 3547-3551 (1961).

Chapter 7

Conclusions

This thesis summarizes the research conducted on the $Zn_{1-x}Mg_xO$ thin film and $Zn_{1-x}Mg_xO/Ag_yO$ heterojunction diodes by the mist-CVD method, which is a non-vacuum, low-cost, and environment-friendly technique. The contents focus mainly on 1) the deposition and evaluation of the properties of $Zn_{1-x}Mg_xO$ films by mist-CVD (Chapter 3); 2) the growth and evaluation of the properties of Ag_xO films by mist-CVD (Chapter 4); 3) the deposition and evaluation of properties of Ag_xO films by RFM-Sputtering (Chapter 5); 4) the fabrication and analysis performance of the $Zn_{1-x}Mg_xO/Ag_yO$ heterojunction diodes, and optimization of the $Zn_{1-x}Mg_xO/Ag_yO$ heterojunction diodes (Chapter 6). This chapter summarizes the contents described in this thesis.

Chapter 3. Fabrication and Characterization of $Zn_{1-x}Mg_xO$ Thin Film Grown by Mist-CVD

The Group II-O-based compound system of ZnO and MgO alloy thin films had been successfully grown by 3rd generation mist-CVD system with tri-chambers. In comparison with the 2rd generation mist-CVD system, the 3rd generation mist-CVD system with plural solution chambers has the advantage of being able to easily manipulate the amount of supplied solution by setting different carrier gas / dilution gas (c.g. / d.g.) and able to easily manipulate the component ratios in the thin film. For example, we can easily deposit the multilayers and devices for its separated solution chambers, etc. Various measurements had been used for characterizing the deposited ZnMgO films. After Mg was introduced, the properties of ZnMgO have changed a lot.

When ZnMgO thin films were growth by the 3rd generation mist-CVD, the following results were revealed. 1) The $H_2O/\{[Zn]+[Mg]\}$ supply ratio has strongly influence on the growth rate, the roughness had the same tendency as the film thickness, the crystal orientations changed and (002) peak was suppressed. 2) As the flow rate of

the Mg c.g. / d.g. increased, the morphology and crystallinity were extensively impacted by the Mg content, the band gaps broadened from 3.3 to 3.7 eV, and the resistivity increased to 1.58×10^8 Ω·cm. 3) In comparison without O_3 and with O_3, we found that ozone can influence Mg incorporation into the ZnO lattice during growth, but also create defects and there was no obvious improvement.

Chapter 4. Fabrication and Characterization of Ag_xO Thin Film Grown by Mist-CVD

Silver is a transition metal so it has novel properties than general metals its oxides contain several valent states. But at low temperatures (> 120 ℃), silver oxide easily decomposes into metallic silver and oxygen. Therefore, low-temperature film fabrication process is required to grow Ag_xO thin films. Sputtering is a well-developed fabrication system for the preparation of Ag_xO film. However, the trial deposition experiments of Ag and Ag_xO films by mist-CVD have been carried out. For Ag deposition, protecting precursor from H_2O and O_3, should be acted with caution during the process phase. H_2O and O_3 can be used as oxidant for Ag_xO deposition and change the flow rate of H_2O and O_3 can control the extent of oxidization. In addition, two chambers can be used for Ag_xO deposition. The deposition temperature at 350 ℃ and 400 ℃ is required for the preparation of Ag and Ag_xO thin films via Mist-CVD system.

Chapter 5. The Effects of R[O_2] % on the Properties of Ag_xO Thin Films Grown by RFM-Sputtering

The properties of Ag_xO thin films with various R[O_2] % by RFM-Sputtering have been investigated and analyzed using different types of measurements. GIXD spectra and SEM images have been used for the crystal structure characterization, and UV-vis spectra and resistance meter have been used for the band gap and resistivity investigations. From GIXD data, it was found that Ag_xO films tended to be a mixture of $Ag^{(II)}O$ and $Ag_2^{(III)}O_3$. To precisely confirm the band gaps of Ag_xO, two different thicknesses of 150 nm and 50 nm were deposited. The PYS spectra were used for work function confirmation. XPS was used to characterize the chemical states of Ag_xO. With an increase in R[O_2] % from 0 % to 30 %, the Ag_xO has a variational orientation for the AgO (111) to Ag_3O_4 (002) grains, and the band gaps have extended to 1.7 eV but narrowed to 1.2 eV with R[O_2] % = 30 %. The chemical states of Ag_xO have been confirmed to be dominated by AgO (R[O_2] % = 10 % and 16 %) and Ag_3O_4 (R[O_2] % = 17 % and 30 %). To conclude, after processing all the results together, the energy lev-

el band has been given but the details of the physical phenomena need furthermore confirmation.

Chapter 6. Fabrication of $Zn_{1-x}Mg_xO/Ag_yO$ Heterojunction Diodes by Mist-CVD at Atmospheric Pressure

In chapter 6, from the single layer experiments obtained recipe, the growth trial of $ZnMgO/Ag_yO$ heterojunction diodes (HJDs) by Mist-CVD system and sputtering deposition techniques has been conducted. Two directions for optimizing the HJDs performance were used. One is investigating the influence of pre-treatment, such as O_3 treatment, H_2O treatment, ICP treatment, pre-annealing in air (PAA), and pre-annealing in N_2 (PAN). And the other is investigating the influence of the Mg component of the ZnMgO layer and R[O_2] % of AgyO films. Treatment of O_3, H_2O, and ICP did not obtain the expected results for improving rectify ratio. However, through pre-annealing in N_2 and in air, the performance of $ZnMgO/Ag_yO$ HJDs has improved depending on the current density on/off rectifying ratio. Without treatment, the junctions between the ZnMgO and Ag_yO also had rectifying behavior, the TEM cross-section image of HJDs presented an abrupt interface, and there were discrepancies in the Schottky barriers and interface band offsets. In the future, to control the top surface roughness, the surface states of ZnMgO and Ag_yO will be investigated, and to deposit a further wider band gap, ZnMgO will be growth with increasing the incorporation of Mg. Then these results will be applied to fabricate $ZnMgO/Ag_yO$ heterojunction diodes, it may be possible to obtain a more higher barrier height of $ZnMgO/Ag_yO$ HJDs.

Appendix

Apx. 1. Back side electrode ITO film properties

InSnO (ITO) thin film prepared on quartz by mist-CVD. Its top surface roughness and band gap information are shown in Figure-Apx. 1. Its electric properties are summarized in Table-Apx.1.

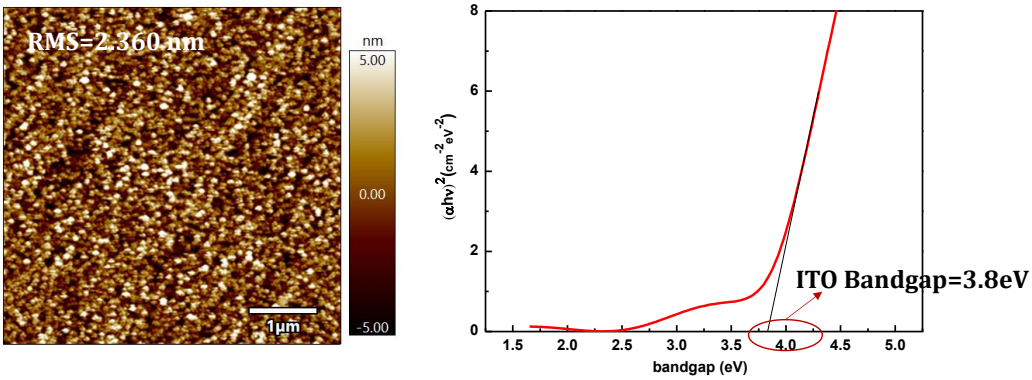

Figure-Apx. 1 AFM image and Tauc plot of ITO films

Table-Apx. 1 ITO electric property

Sample No.	Mobility ($cm^2/V \cdot S$)	Carrier density (cm^{-3})
210420FCM030ITO-11	8.37	-1.2×10^{21}
210420FCM030ITO-25	8.9	-1.7×10^{21}

Apx. 2 ZnMgO AFM images

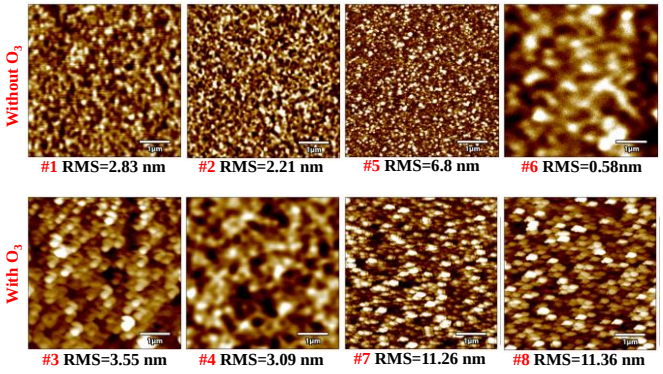

Figure-Apx. 2 AFM images of ZnMgO in comparison after introducing O_3

Apx. 3. Chlorine precursors for ZnMgO thin film deposition

Table-Apx. 2 experiment condition of ZnMgO

	Chamber A	Chamber B	Assistant gas
Source concentration	$ZnCl_2$ +H_2O 50 mM	$MgCl_2$+ H_2O 20 mM	O_3 0, 2, 5, 10, 20, 40, 50 g/m^3
c.g. / d.g. (l/min)	2.0 / 3.	0.0 / 5.0 ~ 5.0 / 0.0	1.5
Growth time & Temperature	5 min & 400 ℃		
Ultrasonic transducer	2.4 MHz, 24 V,·0.625 A		

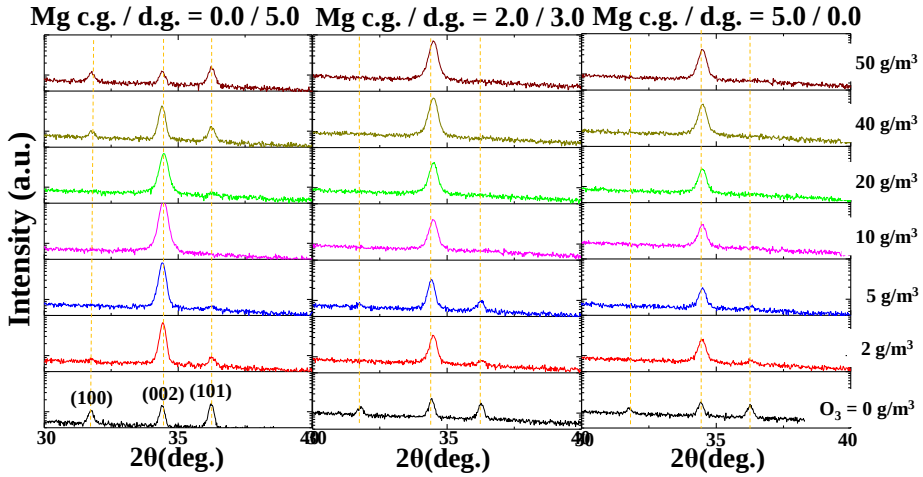

Figure-Apx. 3 GIXD spectra of chlorine precursor ZnMgO thin film

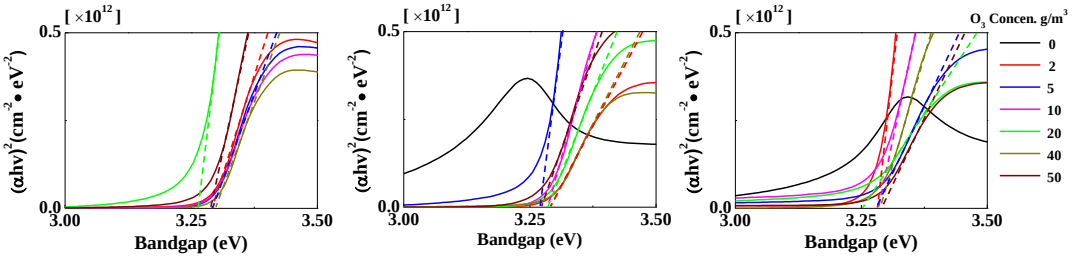

Figure-Apx. 4 Absorption spectra of ZnMgO deposited by chlorine precursors with different O_3 concentrations

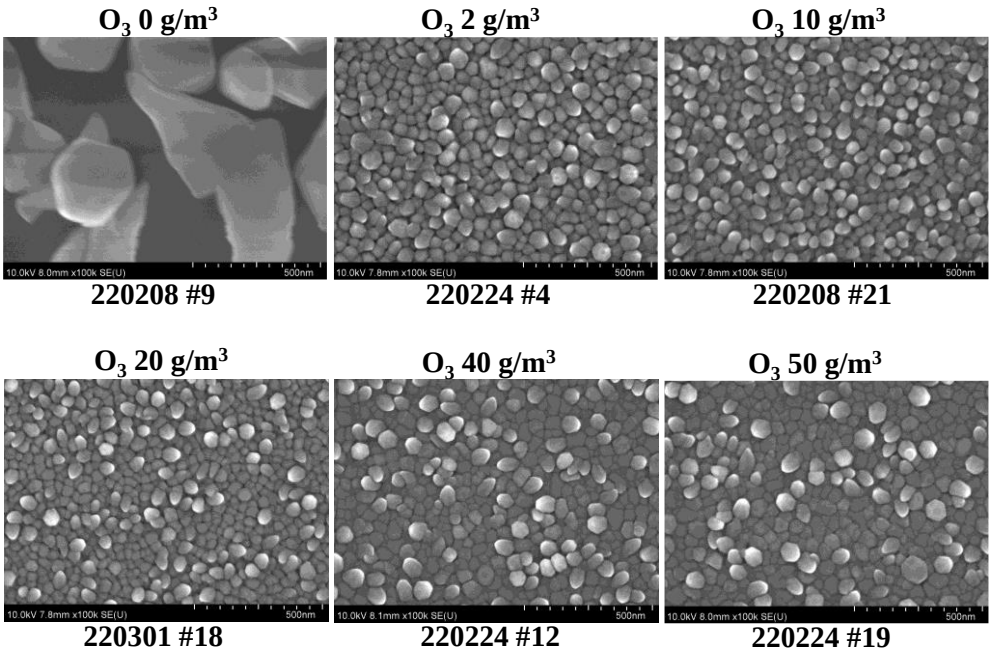

Figure-Apx. 5 SEM images of chlorine precursor ZnMgO thin film

Apx. 4. RFM-sputtering Ag_xO electric properties and PYS spectra

Figure-Apx. 6 shows (a) PYS spectra and (b) Hall effect measurement of Ag_xO films deposited at various R[O_2] %. When R[O_2] = 0 %, the thin film deposition was Ag with work function Φ_m = 4.5 eV, and resistivity $\rho = 1.6 \times 10^{-6}\Omega \cdot \mathrm{cm}$, $N_H = 1.09 \times 10^{22}\mathrm{cm}^{-3}$, $\mu_H = 85.3\ \mathrm{cm}^2/\mathrm{V} \cdot \mathrm{s}$. When R[$O_2$] % increased from 10 % to 15 %, ρ was approximately increased by an order of 11 magnitudes and for R[O_2] = 15 %, ρ reached the peak value by $4.64 \times 10^6\Omega \cdot \mathrm{cm}$. When R[$O_2$] % exceeded 15 %, ρ gradually declined. And as R[O_2] % between 10 % and 13 %, both of N_H and μ_H decreased to $9.62 \times 10^{20}\mathrm{cm}^{-3}$, $14.7\ \mathrm{cm}^2/\mathrm{V} \cdot \mathrm{s}$, respectively. After R[$O_2$] = 13 % the Hall measurement could no longer be obtained. At R[O_2] = 30 %, Φ_m increased to 5.6 eV, this was confirmed by measurement of PYS.

Therefore, the Hall effect data indicates that after R[O_2] = 13 %, the Ag_yO films were transformed from metallic films to semiconductive films. The dramatic increase in resistivity was caused by the large number of oxygen ion combinations. This was confirmed by the UV-vis measurement, in which the band gap of Ag_yO was increased from 1.87 eV to 2.2 eV. We intend to investigate this phenomenon further in future

research. Thorough consideration of the properties of Ag_yO for the fabrication of HJDs, we selected R[O_2] = 16 % & 17 %, which is between 15 % and 20 %, because during this phase the films were grown in an ambient rich in O_2. It is also good for passivating the surface dangling bonds of ZnMgO. The type of ZnMgO and Ag_xO semiconductors were estimated as n-type and p-type, respectively, which refers to the obtained Hall effect data and this assumption will be employed in the band diagram discussion of Chapter 6.

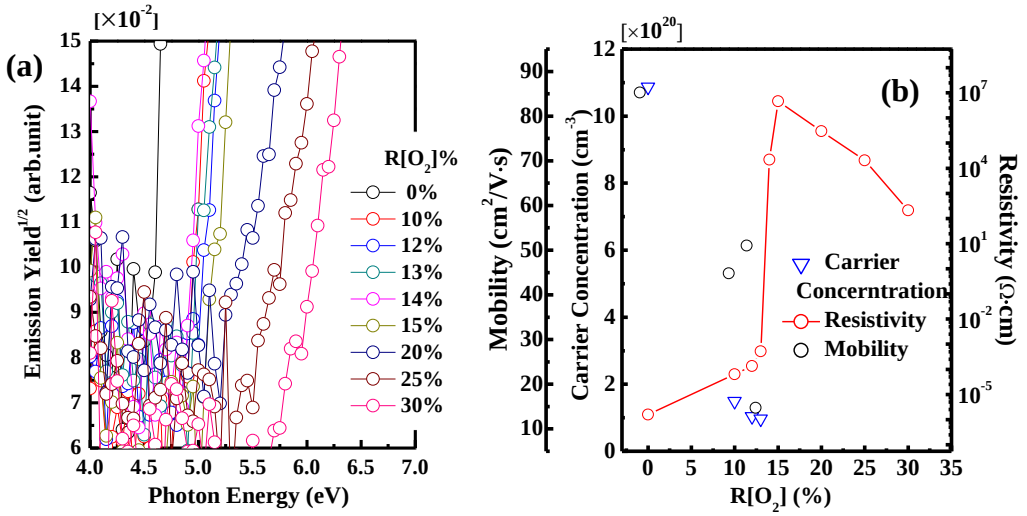

Figure-Apx. 6 PYS spectra (b) Hall effect measurement of the AgyO films with different R[O_2] %

Apx. 5 Temperature Dependence of Grown Ag_xO Thin Films via Mist-CVD

Apx. 5.1 Experimental Methods

The mist-CVD Ag and Ag_xO films conditions are summarized in Table 4-1. The solute is Ag(ac), solvent is methanol (MeOH) and ammonia dissolved in methanol solution (AMS: 2 mol/L), the concentration ratio between MeOH and AMS is 95 : 5. Samples were deposited on quartz substrates. Each quartz substrate was ultrasonically precleaned for 2 min, respectively, in acetone, isopropyl alcohol, and deionized (D.I.) water followed by drying in a N_2 gas gun. The deposition temperature was changed from 450 ℃ to 250 ℃ in 50 ℃ intervals. After finish the deposition, cooling process was adopted to protect the Ag surface from the high temperature caused oxidation in the air, which is keep the sample inside the reaction chamber and introduce N_2 0.0 / 2.0 l/min to cooling down the inside temperature of the reaction chamber below 100 ℃.

Table-Apx. 3 Mist-CVD deposition conditions for Ag_xO films with different temperature

Solute	Ag(ac)
Solvent	MeOH : AMS = 95 : 5
Solution concentration	0.02 mol/L
Growth temperature	450 ℃, 400 ℃, 350 ℃, 300 ℃, 250 ℃
Growth time	300 s
c.g. / d.g. flow rate	N_2, 2.0 / 3.0 l/min
Cooling process	N_2, 0.0 / 2.0 l/min below 100 ℃
Ultrasonic transducer	2.4 MHz, 24 V, 0.625 A

Apx. 5.2 Results and Discussion

Figure-Apx. 7 shows the appearance photos of Ag_xO, which is grown by mist-CVD in the atmosphere. With increasing the temperature at the same conditions, Ag_xO samples present different transparency colors. As the temperature = 250 ℃, the reaction did not occur. Increasing the temperature to 300 ℃, the reaction started and the film presented light yellow color. While the temperature increased to 350 ℃ and 400 ℃, the films were almost the same color of brown. And when the temperature reached the highest 450 ℃, the film was also light yellow similar to 300 ℃.

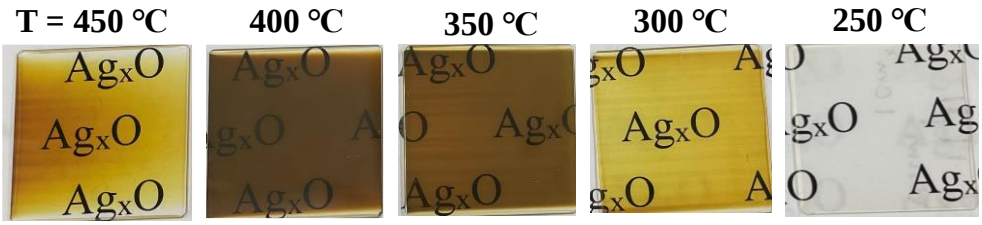

Figure-Apx. 7. Appearance images of Mist-CVD Ag_xO

Resistance was measured using the impedance analyzer, as shown in Table-Apx. 4. For the highest temperature of 450 ℃, its resistivity has the highest value of around 12 digits and has good transparency. And after the temperature was decreased, its resistivity also decreased.

Table-Apx. 4 Resistivity of Mist-CVD Ag_xO dependence on temperature

	450 ℃	400 ℃	350 ℃	300 ℃	250 ℃
Resistivity	3.28×10^{12}	5.64×10^{10}	4.5×10^{10}	×	×
Growth	○	○	○	×	×

Apx. 5.3 Summary

From the appearance photos, the growth temperature for the Ag thin film might be at 350 ℃. Although the growth conditions were definitely the recipe for fabricating silver metal thin film, a transparent thin film was created, which is a different from the properties of metal films. I will leave it to my juniors to solve this mystery.

Apx. 6. Thermal ionic emission of barrier height calculations

Figure-Apx.7 is the example data from one of the J-V characteristics of ZnMgO/Ag_yO HJDs (Mg c.g. / d.g. = 1.0 / 4.0 of ZnMgO, R[O_2] = 17% of Ag_xO) Through thermionic emission current equation (1):

$$J = A^{*}T^{2}\exp\left(-\frac{q\varphi_b}{k_BT}\right)[\exp\left(\frac{qV}{nkT}-1\right)],$$

where $A^{*}$is the effective Richardson constant that was obtained from the effective electron mass in ZnMgO m^{*} = 0.27 m_0 so that $A^{*}$of ZnMgO is estimated as 32 A cm^{-2} K^{-2}, V is the applied voltage, n is the ideality factor, k is the Boltzmann constant and T is the absolute temperature. Then using an approximate formula and converting it into logarithms we can get this equation (2):

$$\phi_{Bn} = \frac{kT}{q}\ln(\frac{A^{*}T^{2}}{J_0}) .$$

Using Equation (2) to calculate the barrier height, we can then input the original data

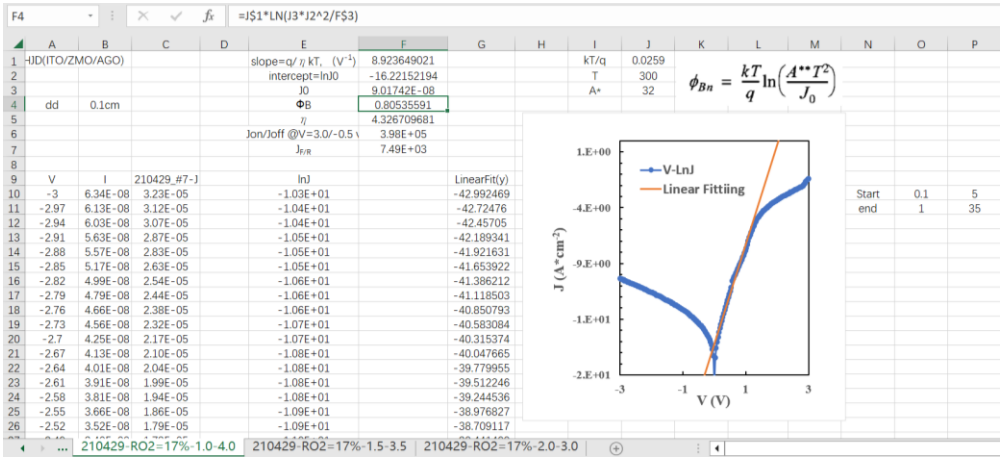

Figure-Apx. 8 Barrier height calculation approach

of the J-V characteristics into Excel as shown in Figure-Apx. 7. To obtain slope and intercept values, these values are put into this transformed equation (2). Finally, we can confirm the barrier height of ZnMgO/Ag_yO HJDs.

List of Publications

Published Papers

1) "Fabrication of $Zn_{1-x}Mg_xO/Ag_yO$ heterojunction diodes by Mist-CVD at atmospheric pressure", **Xiaojiao Liu**, Giang T. Dang, Li Liu, Toshiyuki Kawaharamura, Applied Surface Science 596 (2022) 153465 (6 pages) (10.1016/j.apsusc.2022.153465) (P.O.:2022.04.28, Accepted:2022.04.19, Received:2021.12.31).
2) "The Effects of Oxygen Flow Ratio on the Properties of Ag_xO Thin Films Grown by Radio Frequency Magnetron-Sputtering ", **Xiaojiao Liu**, Giang T. Dang, Tatsuya Yasuoka, Li Liu, Toshiyuki Kawaharamura, (Accepted: 2023.09).
3) "Boron Doped a-SiO_x:H Prepared by H_2 Diluted SiH_4 + CO_2 Plasma", **Xiaojiao Liu**, Junchuan Yin, Jiawei Zhang, Ming Li, Peizhi Yang, Zhihua Hu, et al., Int. J. Electrochem. Sci., 11 (2016) 10827 - 10836, doi: 10.20964/2016.12.94.
4) "Optical and electrical properties of p-type a-SiO_x:H thin films prepared by using PECVD method", **Xiaojiao Liu**, Guanghui Shi, Chuanjun Yin, Hang Li, Hua Liao, Zhihua Hu, Journal of Yunnan Normal University (Natural Sciences Edition): Vol.36, 2016, 5-8.
5) "Effect of CO_2/SiH_4 gas flow ratio on the structure and optical properties of Si-O_x:H thin films", **Xiaojiao Liu**, Guanghui Shi, Ye Tu, Jieqing Liu, Shurong Wang, Zhihua Hu, Acta Energiae Solaris Sinica: Vol.38, 2017.
6) "Optical and Electrical Properties of Boron Doping a-SiO_x:H Thin Films Prepared by Using RF-PEVD Method", **Xiaojiao Liu**, Guanghui Shi, Chuanjun Yin, Hongxia Liu, Ye Tu, Zhihua Hu, Acta Energiae Solaris Sinica: Vol.40, 2017.

International and domestic conferences

1) "Challenge of Using Mist-CVD for Preparation of $Zn_{1-x}Mg_xO/Ag_yO$ Schottky Diodes", **Xiaojiao Liu**, Giang T. Dang, Tatsuya Yasuoka, Yoshiro Kawanishi, Li Liu, Toshiyuki Kawaharamura, Solid State Devices and Materials (SSDM 2021), all-virtual conference (Sep. 06-09, 2021), 10: Thin Film Electronics: Oxide / Non-single Crystalline / Novel Process.
2) The 70th JSAP Spring Meeting (JSAP 2023 Mar. 14-18): "The Effects of R[O_2] % on the Optical Properties Sputtering", **Xiaojiao Liu**, Giang T. Dang, Tatsuya Yasuoka, Li Liu, Toshiyuki Kawaharamura (Oral presentation).
3) Material Strength and Applied Mechanics (MSAM 2023 Jul. 04-07): " The Effect of O_3 and [H_2O] / {[Zn]+[Mg]} Supply Ratio on the Properties of $Zn_{1-x}Mg_xO$ Thin Films Grown by mist-CVD", **Xiaojiao Liu**, Giang T. Dang, Tatsuya Yasuoka, Li Liu, Toshiyuki Kawaharamura (oral presentation).